The Argo

Final Design Report

Team Dauntless

Team Members: Andrew Cichon, Ted Lataif, Himmat Mann, Jason Moon,

Avantika Murali, Emily Tokarski

AE443

University of Illinois Urbana-Champaign

Department of Aerospace Engineering

April 30, 2020

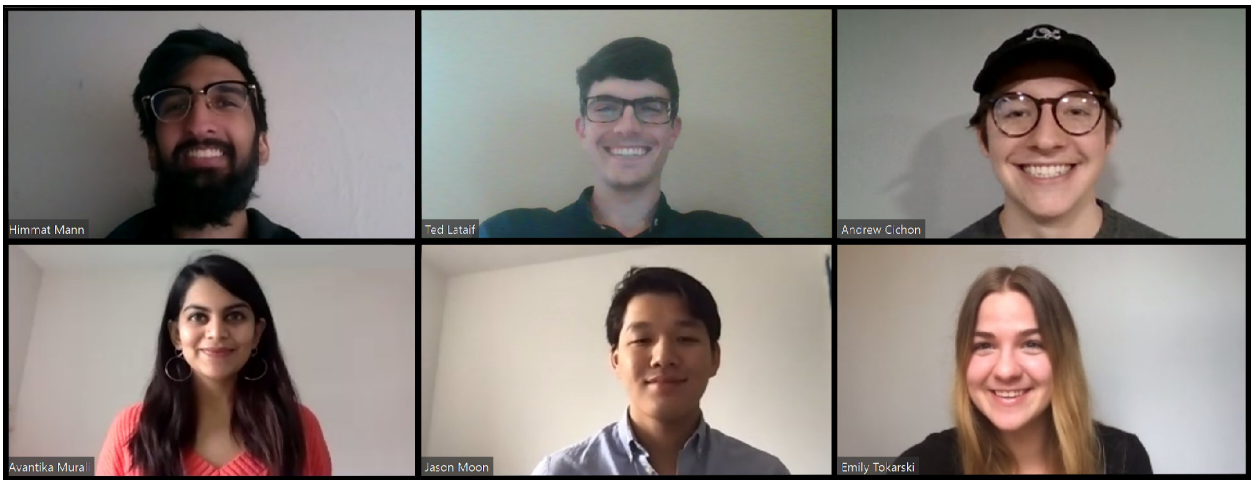

Team Dauntless

Group Member Contributions

Name	Signature	Member Contribution	AIAA Number
Andrew Cichon	Andrew Cichon	Concept of Operations, Propulsion, Performance, Certification	979638
Ted Lataif	L. C. Lataif AIAA	Team Lead, Configuration	1108747
Himmat Mann	Himmat Mann	Mass Properties, Acoustics	1108791
Jason Moon	Jason M.	Structures, Loads and Dynamics, Landing Gear	1108715
Avantika Murali	Avantika Murali	Aerodynamics, Stability and Control, Interior Design	981643
Emily Tokarski		Systems, Cost, Avionics	1108811

Head Advisor

Name	Signature
Jason Merret	Jason M Merret

Contents

Nomenclature

a_t = Horizontal tail lift curve slope
a_w = Wing-body lift curve slope
α = Angle of attack
b = Span
c = Chord
C_f = Skin friction coefficient
C_L = Lift coefficient
C_D = Drag coefficient
C_{D_0} = Zero lift drag coefficient
$C_{l\beta}$ = Rolling moment derivative with respect to sideslip angle
C_{lp} = Rolling damping derivative
$Cl_{\delta a}$ = Aileron control power
$CL_{\delta e}$ = Elevator control power
$Cl_{\delta r}$ = Rolling moment sensitivity to rudder deflection
$C_{L_{max}}$ = Maximum lift coefficient
C_M = Moment coefficient
$C_{M\alpha}$ = Pitching moment derivative with respect to angle of attack
$CM_{\delta e}$ = Pitching moment sensitivity to elevator deflection
C_{Mq} = Pitch damping derivative
$C_{n\beta}$ = Yawing moment derivative with respect to sideslip angle
$Cn_{\delta r}$ = Rudder control power
C_{nr} = Yawing moment derivative with respect to roll angle
c_r = Root chord
c_t = Tip chord
δ_a = Aileron deflection
δ_e = Elevator deflection
δP = Cabin pressure differential
δ_r = Rudder deflection
e = Oswald efficiency factor
ϵ_α = Downwash angle derivative
g = Acceleration due to gravity
h_{AC} = Aerodynamic center as % wing MAC
h_{CG} = Center of gravity as % wing MAC
h_{NP} = Neutral point as % wing MAC
i_t = Tail incidence angle
i_w = Wing incidence angle
K_A = Aerodynamic term in ground-roll distance computation
kt = Knots
K_T = Thrust term in ground-roll distance computation
l_t = Tail arm
L/D = Lift-to-drag ratio
M = Mach Number
M_{dd} = Drag divergence Mach Number
ρ = Density
σ = Stress
TSFC = Thrust specific fuel consumption
S_{ref} = Reference wing area
S_t = Horizontal tail area
S_{TR} = Transition distance
S_v = Vertical tail area
T_2 = Spiral mode doubling time
τ_a = Aileron effectiveness
τ_e = Elevator effectiveness
τ_r = Rudder effectiveness
τ_R = Roll time
$\frac{t}{c}$ = Thickness to chord ratio
T/W = Thrust to weight ratio
λ = Taper ratio
V_1 = Decision speed
V_2 = Takeoff safety speed
V_A = Design maneuvering speed
V_B = Design speed for maximum gust intensity
V_C = Design cruise speed
V_D = Design diving speed
V_H = Horizontal tail volume coefficient
V_{LOF} = Lift-off speed
V_{TO} = Takeoff speed
V_{TR} = Transition speed
V_V = Vertical tail volume coefficient
$\Lambda_{c/4}$ = Quarter-chord sweep angle
ω_n = Natural frequency
ζ = Damping ratio

Acronyms

A/C = Air Conditioning
AC = Alternating Current
ADIRS = Air Data Inertial Reference Unit
ADS-B = Automatic Dependent Surveillance Broadcast
AIAA = American Institute of Aeronautics and Astronautics
AIMS = Airplane Information Management System
ADA = American with Disabilities Act
APU = Auxiliary Power Unit
AR = Aspect Ratio
ATC = Air Traffic Control
BFL = Balanced Field Length
CAD = Computer Aided Design

CER = Cost-Estimating Relationship
CFD = Computational Fluid Dynamics
CFR = Code of Federal Regulations
CG = Center of Gravity
DAPCA IV = Development and Procurement Costs of Aircraft Version 4
DC = Direct Current
DCN = Data Concentration Network
DISA = Delta International Standard Atmosphere
DOT = Department of Transport
EAS = Equivalent Airspeed
ECU = Engine Control Unit
ECS = Environmental control Systems
E&E = Electronic & Equipment
EGPWS = Enhanced Ground Proximity Warning System
EPNL = Effective Perceived Noise Level
ETACS = Electronic Time and Alarm Control System
ETOPS = Extended Twin Operations
EW = Empty Weight
FAA = Federal Aviation Administration
FADEC = Full Authority Digital Electronic Control
FH = Flight Hour
FMU = Fuel Management Unit
HBPR = High Bypass Ratio
HF = High Frequency
HLS = High Lift System
HUD = Heads-up Display
IDG = Integrated Drive Generator
IFE = In-flight Entertainment
IFR = Instrument Flight Rules
IPPS = Integrated Power Plant System
ISA = International Standard Atmosphere
JFK = John F. Kennedy International Airport
KCAS = Knots Calibrated Airspeed
KEAS = Knots Equivalent Airspeed
KIAS = Knots Indicated Airspeed
KTAS = Knots True Airspeed
LEMAC = Leading Edge Mean Aerodynamic Chord
LFL = Landing Field Length
LHR = London Heathrow Airport
MAC = Mean Aerodynamic Chord
MCT = Maximum Continuous Thrust
MGMT = Management
MLW = Maximum Landing Weight
MMR = Multi-Mode Receiver
MRW = Maximum Ramp Weight
MTOW = Maximum Takeoff Weight
NACA = National Advisory Committee for Aeronautics
NASA = National Aeronautics and Space Administration
OEI = One Engine Inoperative
OEM = Original Equipment Manufacturer
PIP = Performance Improvement Package
PRSOV = Pressure Reducing Shut-Off Valve
RAT = Ram Air Turbine
RDT&E = Research Development Test and Evaluation
RFP = Request For Proposals
ROC = Rate of Climb
SATCOM = Satellite Communications
SC = Supercritical
SOV = Shut-off Valve
TCAS = Traffic Collision Avoidance System
TOFL = Takeoff Field Length
TSFC = Thrust Specific Fuel Consumption
USD = US Dollars
VFR = Visual Flight Rules
VHF = Very High Frequency
WXR = Weather Radar

List of Figures

List of Tables

Executive Summary

As air travel becomes increasingly common around the world, many airports and airlines are struggling to overcome congestion. One solution is to use high-capacity aircraft on shorter routes that typically see mid-size aircraft. This led to an RFP from AIAA requesting a 400 seat aircraft with a range of 3,500 nmi [1]. The aircraft was required to have 50 business class and 350 economy class seats. The aircraft was to be optimized based on a reference mission of 700 nmi.

The aircraft, named the *Argo*, will be a single deck, twin-aisle aircraft with two under-wing turbofan engines. In order to save weight and optimize the aircraft for short distances, the wing has an area of 4,000 ft^2 and an aspect ratio of 7.3. The estimated MTOW is 500,000 lb. Similarly sized aircraft include the Boeing 777, Airbus A350 and Boeing 747, but these aircraft are all designed for ranges greater than 7,000 nmi. Therefore, the proposed design incorporates aspects of high-capacity aircraft along with common features of short-range aircraft. Since weight plays a much greater factor in short-range flights than drag does, the aircraft was designed to minimize MTOW and fuel weight as much as possible. The aircraft was designed with future derivatives in mind in order to create a family of aircraft. Future models could be lengthened or shortened, converted to a cargo configuration, or feature additional fuel tanks for extended range. In this way, the program revenue could be greatly increased with minimal additional development cost. With a projected production run of 1,000 aircraft, the unit list price of the *Argo* will be $186 million. This price gives it a significant competitive advantage over other similar aircraft.

The team is confident that all requirements outlined in the RFP have been met [1]. Based on estimates for thrust and weight, the 9,000 ft take-off field length requirement have been met. When operating with a full payload, the required fuel to meet the range requirement is 151,000 lb of fuel. All aspects of the *Argo* will comply with existing FAA regulations. With a competitive cost and compatibility with existing infrastructure, Team Dauntless is confident that the *Argo* will have the first-mover advantage that will make it a successful program in the emerging market of high-capacity, short-range aircraft.

I. Introduction

Air travel has become increasingly popular as the average cost of both domestic and international tickets have decreased. Large airports such as John F. Kennedy International (JFK) and London Heathrow (LHR) are experiencing large delays and congestion as the number of people moving through each airport continues to increase. In order to meet the needs of both airlines and travellers, this project aims to design a high-capacity short-range aircraft. The *Argo* meets a maximum range of 3,500 nmi while being optimized for a 700 nmi flight. The priority in design was decreasing the weight as much as possible to reduce fuel costs. On a short flight, weight plays a much more significant factor than drag in determining required fuel. A smaller wing will cost less to manufacture in addition to weighing less, making the aircraft more efficient on short haul flights. Further, a smaller wing allows the *Argo* to comply with FAA Class D regulations and therefore allows it to service more airports [2]. Being a high-capacity aircraft, the *Argo* can seat up to 400 passengers in a two-class configuration with 50 business class seats and 350 economy class seats. The aircraft is planned for an entry into service of 2029, and will be designed to reduce costs for all parties involved. This includes optimizing cost of production as well as operation. As the demand for air travel continues to increase, the *Argo* will emerge as the top choice for a low cost and efficient aircraft that moves both people and goods across the globe.

II. Concept of Operations

A. Requirements

The RFP published by AIAA outlines mandatory and tradable requirements [1]. Mandatory requirements closely relate to the performance of the aircraft, as well as basic configuration. These requirements are compiled in Table 1.

Table 1 RFP Design Requirements [1]

Category	Requirement	Section
Instruments	Capable of VFR and IFR with autopilot	XI.H
Certification	Meets certification rules of FAA 14 CFR Part 25	All
Powerplant	In service by 2029	V
Crew	2 pilots and 8 flight attendants	IV
Passenger Capacity	400 passenger capacity; 50 business class and 350 economy class	IV
Baggage	5 ft^3 of baggage per passenger	IV
Payload	200 lb passenger/pilot/attendant weight and 30 lb baggage per passenger	IV & X
Range	3,500 nmi design range	VII.K
Fuel Reserves	Flight to alternate airport 200 nmi from destination airport, 30 minute loiter at alternate airport, and 5% contingency fuel	VII.K
Takeoff Length	9,000 ft over 35 ft obstacle at ISA + 15°C	VII.K

B. Mission Profile

A typical mission profile can be determined with the outlined requirements. This is shown in Figure 1. After an initial sizing analysis and configuration were established, details about the mission profile were calculated to minimize the MTOW of the aircraft. This included varying designated cruise altitude, cruise speed, aspect ratio, and other geometric parameters of the aircraft. The details of each mission segment are presented in Table 2.

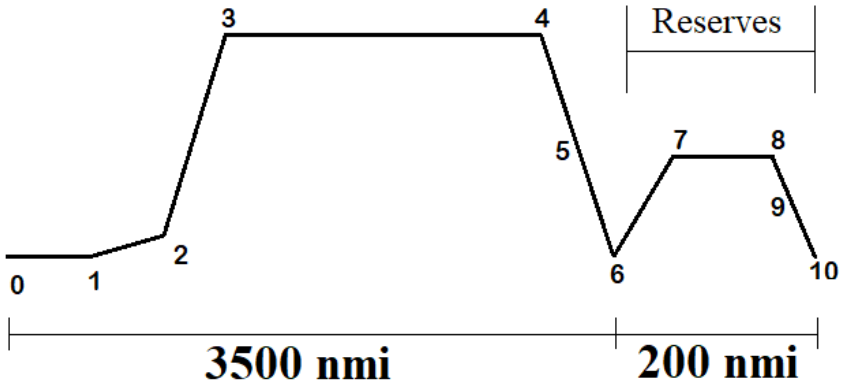

Figure 1 Typical Mission Profile

Table 2 Mission Profile Segments

Number	Description	Specific Details
0-1	Start, warm-up, & taxi	-
1-2	Takeoff	-
2-3	Climb	2,000 ft/min
3-4	Cruise	36,000 ft at M = 0.82 for 3,500 nmi
4-5	Descent	-
5	Loiter	5 minutes at 5,000 ft
5-6	Landing	-
6-7	Climb	2,000 ft/min
7-8	Divert	200 nmi to alternate airport
8-9	Descent	-
9	Loiter	5 minutes at 5,000 ft
9-10	Landing	-

The rate of climb, cruise altitude, and cruise speed were all chosen to minimize the MTOW of the aircraft. Although rate of climb had little effect on the size of the aircraft, its value was chosen to be 2,000 ft/min as this is typical of most aircraft this size. The cruise altitude was chosen to ensure the power requirement for steady level flight would not be too high. The cruise speed was chosen as Mach 0.82 in order to maximize aerodynamic efficiency.

C. Derivative Aircraft

One the possibilities for the *Argo* program is the potential for a family of derivative aircraft. Many commercial airliners currently on the market are developed as a family, for instance, the Airbus 320 family, which share a common design, but have a wide range of passenger capacity and design ranges. The *Argo* program could include a handful of derivatives, including an extended range version, a smaller, 250-300 passenger capacity version, or the capability to be outfitted as a corporate jet or freighter variant. The benefits of an aircraft family include lower production costs, increased revenue for the manufacturer, and common pilot rating for the airlines. Further, as the *Argo* earns a good reputation in the industry, airlines will be incentivized to invest in additional variants of the *Argo*. An extended range derivative is further discussed in Section XII.C.

III. Sizing Analysis

A. Similarity Analysis

In order to start the sizing analysis process, similar aircraft were considered due to similar passenger capacity and range requirements. Of the aircraft considered, the Boeing 777-300ER and the Boeing 747-8i were chosen as seeds because of their similar passenger capacities. Since single and double deck configurations were considered for the *Argo*, two seed analyses were conducted. A seed analysis involves gathering data from a similar aircraft and calculating the major characteristics of a new aircraft based on the difference in size. The data extracted from the similarity analysis can be seen in Table 3. All data in Table 3 was gathered from Jane's All the World's Aircraft [3].

Table 3 Data from Similarity Analysis

Parameter [units]	Boeing 777-300ER	Boeing 747-8i
Empty Weight [lb]	260,000	470,000
AR	8.70	8.45
Wing Weight [lb]	109,072	231,881
Fuselage Length [in]	2,509	1,746
Double Decker Length [in]	-	1,176
Horizontal Tail Area [ft^2]	1,090	1,470
Vertical Tail Area [ft^2]	573	830
Takeoff Thrust [lb]	98,000	133,000
T/W IPPS [lb/lb]	5.59	5.37

B. Initial Sizing

The initial size of the *Argo* was determined using a sizing method based on a seed aircraft. First, the performance of a seed aircraft was established as a baseline. In order to determine initial dimensions for the *Argo*, different parameters were changed to see how they influenced performance. Estimations for thrust required, fuel weight, and total weight

difference between the seed and the *Argo* were iterated until the range and takeoff distance matched the requirements from the RFP [1]. Limits typically shown on a constraint diagram were built into this method. Consequently, only solutions which were within the limits outlined in 14 CFR Part 25 were shown [4].

Most complex calculations in this method came from Raymer [5] or Roskam [6]. Other equations were provided by the head advisor for the project based on industry knowledge [7]. The inputs chosen were based on typical values for similar aircraft or predicted technological advances. The spreadsheet was used to create a series of contour plots. A trade study was conducted using these values to establish wing area and aspect ratio. The contour plots in Figures 2 and 3 show how fuel and takeoff weight vary with wing area and aspect ratio. The wing area of 4,000 ft^2 and aspect ratio of 7.3 were chosen to minimize takeoff weight and fuel weight.

The completed spreadsheet was used to find the values of different major aircraft components and performance figures. These values were used as a starting point for a part-by-part buildup of the aircraft and do not necessarily reflect the final design of the *Argo*.

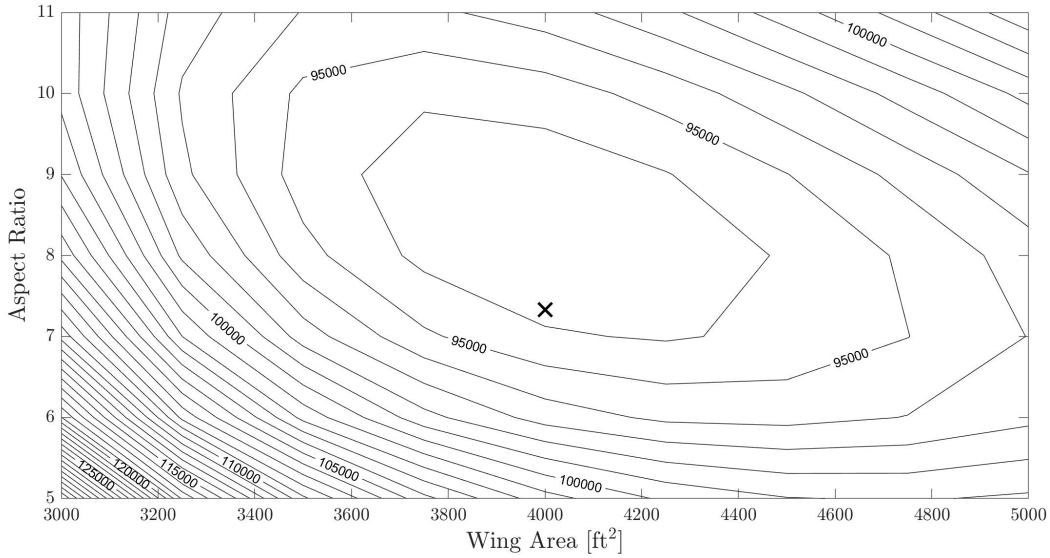

Figure 2 Estimated Fuel Weight with Boeing 777 as Seed

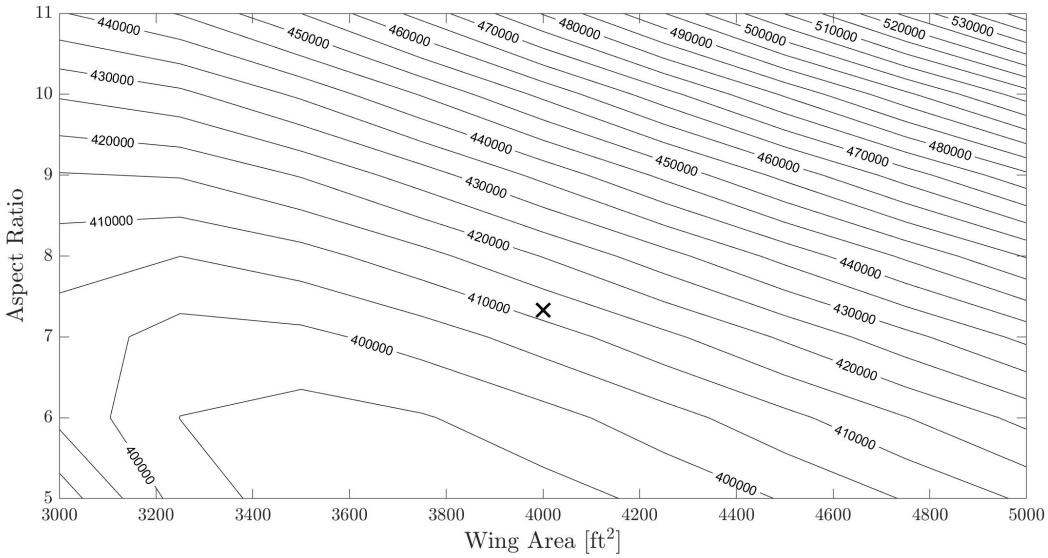

Figure 3 Estimated MTOW with Boeing 777 as Seed

Table 4 Allocated and Derived Requirements from Sizing Analysis

Parameter [Units]	Value	Justification	Allocated or Derived
T/W IPPS [lb/lb]	5.8	Typical industry value	Allocated
$C_{L_{max}}$	2.2	Expected value from airfoil and HLS	Allocated
Payload Weight [lb]	94,300	AIAA Requirement	Allocated
Max. Payload Weight [lb]	111,800	Study of DOT Load Factors [8]	Allocated
TSFC [lb/lb/hr]	0.545	GE90-115B Published TSFC	Allocated
Fuselage Weight [lb/in]	64.89	Scaled from known G650 weight [9]	Allocated
Cruise Mach	0.82	Typical transonic cruise speed	Allocated
Rate of Climb [ft/min]	300	Typical airliner value	Allocated
L/D	14.03	Reasonable value for low AR, twin-aisle airliner	Derived
MTOW [lb]	440,000	Calculated from payload and weight difference	Derived
MLW [lb]	385,000	Typical fraction of MTOW	Derived

C. Trade Study for Maximum Payload Weight

A trade study was conducted to determine the maximum payload weight for the *Argo*. This was done to accommodate at the average amount of freight carried between JFK and London Heathrow, the two airports mentioned in the RFP [1]. This revenue payload was then incorporated into the maximum payload weight. For this trade study, data from the Department of Transportation was used which shows data on the number of departures and total freight per month gathered over a two year span from May 2017 to April 2019 as seen in Table 5.

Table 5 Freight Data on Flights between JFK International and London Heathrow [8]

Month	No. of Departures	Freight [lb]	Avg Freight/Flight [lb]	Month	No. of Departures	Freight [lb]	Avg Freight/Flight [lb]
May-17	585	7,206,820	12,319	May-18	614	7,245,347	11,800
Jun-17	576	8,586,369	14,906	Jun-18	597	7,709,505	12,913
Jul-17	604	8,077,249	13,372	Jul-18	618	7,307,010	11,823
Aug-17	606	7,881,258	13,005	Aug-18	617	7,750,420	12,561
Sep-17	580	8,455,893	14,579	Sep-18	596	8,403,059	14,099
Oct-17	609	8,043,281	13,207	Oct-18	601	7,620,288	12,679
Nov-17	558	8,954,816	16,048	Nov-18	549	7,562,706	13,775
Dec-17	576	7,916,740	13,744	Dec-18	597	8,266,835	13,847
Jan-18	536	7,674,626	14,318	Jan-19	556	7,635,017	13,732
Feb-18	495	7,980,466	16,122	Feb-19	526	7,366,987	14,005
Mar-18	554	8,343,035	15,059	Mar-19	593	8,875,605	14,967
Apr-18	596	7,592,601	12,739	Apr-19	592	6,770,201	11,436

Table 6 Maximum Payload Weight Build Up

Weight	Per Person [lb]	Total [lb]
Passenger/Pilot/Flight Attendant	200	82,000
Baggage	30	12,300
Freight	-	17,500
Maximum Payload	-	111,800

The results of the trade study showed that over the two year period from May 2017 to April 2019, the overall average freight taken onboard a flight between JFK and London Heathrow was 13,638 lb while the highest average was seen in November 2017 at 16,048 lb. The *Argo* was given a revenue payload capacity of 17,500 lb. The weight of the passengers, pilots, and flight attendants total 82,000 lb, assuming 200 lb per person. Baggage adds another 12,300 lb assuming 30 lb of baggage per person as per the RFP [1]. The total maximum payload weight build up can be seen in Table 6.

IV. Configuration

A. Design Morphology

A major decision in determining the configuration of this aircraft was whether to design a single-deck or double-deck aircraft. A single-deck aircraft would feature the business class section at the front of the aircraft, like most modern airliners. The other option was to place the business class section, along with an appropriate number of lavatories and galleys, on a deck above the economy section, similar to the Boeing 747. The estimated weight of each configuration was determined and a contour plot was created to show the estimated weight difference between the two options. A positive value on the contour plot implies that the double-deck option is heavier. Figure 4 shows that a

twin-deck aircraft will be at least 120,000 lb heavier than a single deck due to structural complexity and additional fuel requirements. For these reasons, the decision was made to design a single deck aircraft.

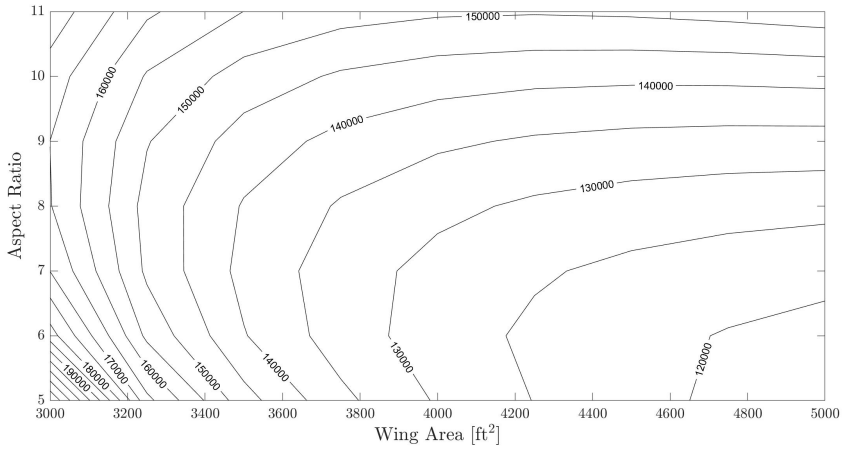

Figure 4 Estimated Difference in MTOW for Single vs. Double Deck Aircraft

The other significant consideration was empennage layout. The three options considered were a traditional layout, T-tail, and V-tail. These options, along with single and double deck fuselages, are shown in Figure 5. The final configuration of the *Argo* is highlighted. The main advantage of a T-tail is that the control surfaces are moved out of the wing wake and therefore are more efficient. However, placing the horizontal stabilizer at the top of the vertical stabilizer significantly increases the weight and complexity of the empennage. A V-tail is the lightest option of the three as it eliminates nearly a third of the empennage surface area. The downside to a V-tail is that coupling the elevators and rudder is a complex controls challenge. Therefore, the decision was made to design a conventional empennage.

B. External Layout

1. Fuselage

A cylindrical fuselage was chosen for several reasons. The main benefit is structural, since it is simpler to build a pressurized aircraft with a circular cross section. A cylindrical fuselage also minimizes structural weight. An ovular cross section would be structurally complex and weigh more. The fuselage is 21.3 ft in diameter and 238.3 ft long. The barrel section is 162 ft long, capped by a 21 ft nose cone and 55 ft tail cone. The belly upsweep angle is 20° in order to avoid tail strikes on takeoff. The size of the fuselage was determined by seating requirements. With 10 seats per row in the economy section and 20 in wide aisles, the cabin will be 20.3 ft wide. Baggage did not limit sizing in any way, but the aircraft will have a cargo hold capable of carrying LD3 shipping containers [10].

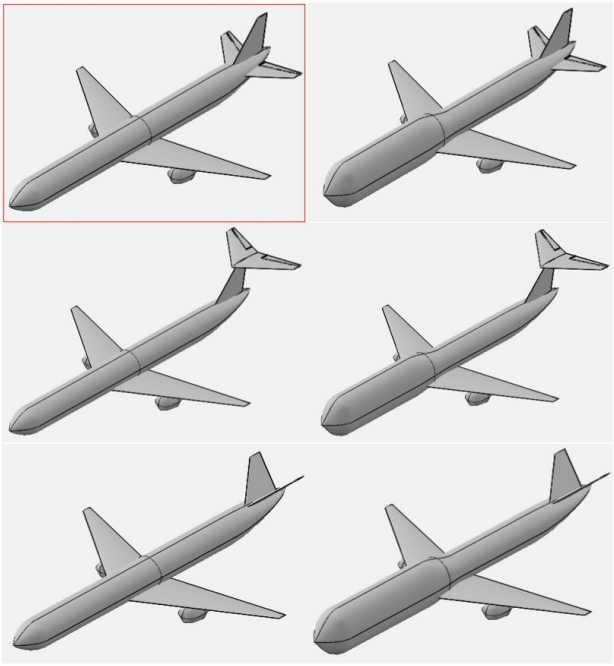

Figure 5 Empennage and Fuselage Configurations Options

2. Engines

The decision to use two under-wing engines was made based on the estimated required thrust and available engines. Using more engines or mounting them in different locations is unnecessarily complex and structurally inefficient. The size of the engines would make mounting them anywhere other than below the wing difficult; it would require larger structural supports and additional weight. Under-wing engines also contribute to wing bending moment relief. This allows the structures team to design a smaller wing box and decrease weight. Additionally, under-wing engines provide a safety benefit. In the case of ditching, the engines absorb energy and break off, allowing the plane to float longer. In the case of an inoperative engine, placing the engine close to the fuselage helps the yawing moment caused by asymmetric thrust. However, placing the engines too close to the fuselage would negatively affect loads. The engines have been placed 29.3 ft away from the fuselage, measured between centerlines.

3. Landing Gear

The landing gear will be in a tricycle configuration with the nose landing gear in front of the center of gravity on the fuselage and the two main landing gear behind the center of gravity on the wings. The gear will be retractable in order to minimize drag in flight. The wing and wing box have the space to stow the large gear that the aircraft will require. Based on the estimated maximum landing weight, the main landing gear will each have four tires. The ground lines are shown in Figure 6. The configuration of the landing gear also depends largely on the mission profile. Large aircraft are much easier to load and unload quickly when the fuselage is level on the ground. A tail-dragger landing gear

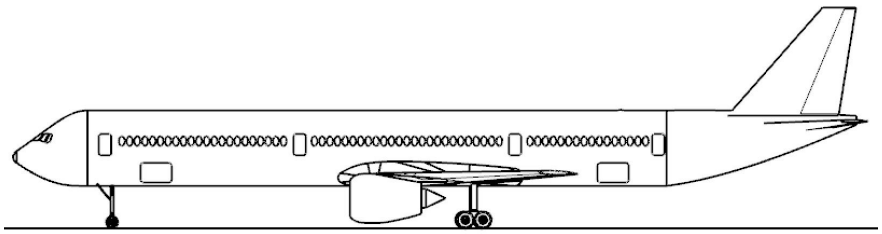

Figure 6 Ground Lines

would complicate the operation of the aircraft. It would also be difficult to design landing gear other than a tricycle type which could safely bear the loads imposed by the *Argo*. Landing gear will be discussed more in depth in Section IX.E.

4. Wing

The wing was primarily sized by weight, as shown in III. The wing area of 4,000 ft^2 provides sufficient lift for the *Argo*. The choice of 7.3 for the aspect ratio achieved a two-fold purpose. It served as a half-way point between the reduction of MTOW and fuel weight. It also limited the wingspan to 170.7 ft and within Class D limits [2].

5. Empennage

The horizontal and vertical stabilizers will be conventional for the sake of simplicity. A T-tail was considered but ruled out because of the structural penalties. It was decided that a V-tail was not a feasible option for an aircraft of this size. Empennage sizing was determined by stability and control and is discussed further in Section VIII. The upsweep of the aft section is determined by aerodynamics and landing gear. In order to avoid a tail strike on landing or takeoff, the belly upsweep has been set to 20 degrees.

6. Doors & Windows

There are four doors on each side of the aircraft. Boarding will typically occur at the first and/or second doors on the left, in keeping with industry standards and existing infrastructure. Each door is 42 in wide and 72 in tall and is certifiable as a Class A emergency exit door [11]. The windows in the cabin are 18 in high and 10 in wide. This size was determined from pressurization and structural requirements and is comparable to the Boeing 787 window size [12]. The windows are larger than other aircraft, but add a feeling of spaciousness and comfort to the cabin. They are symmetrically placed between the fuselage frames.

7. 3-View

A detailed CAD model was created using NX 12. This model shows the exact dimensions of the exterior and shows one potential interior layout. The three-view dimensioned drawing and isometric view is shown in Figure 7. Detailed structural models are shown in Section IX.C.1.

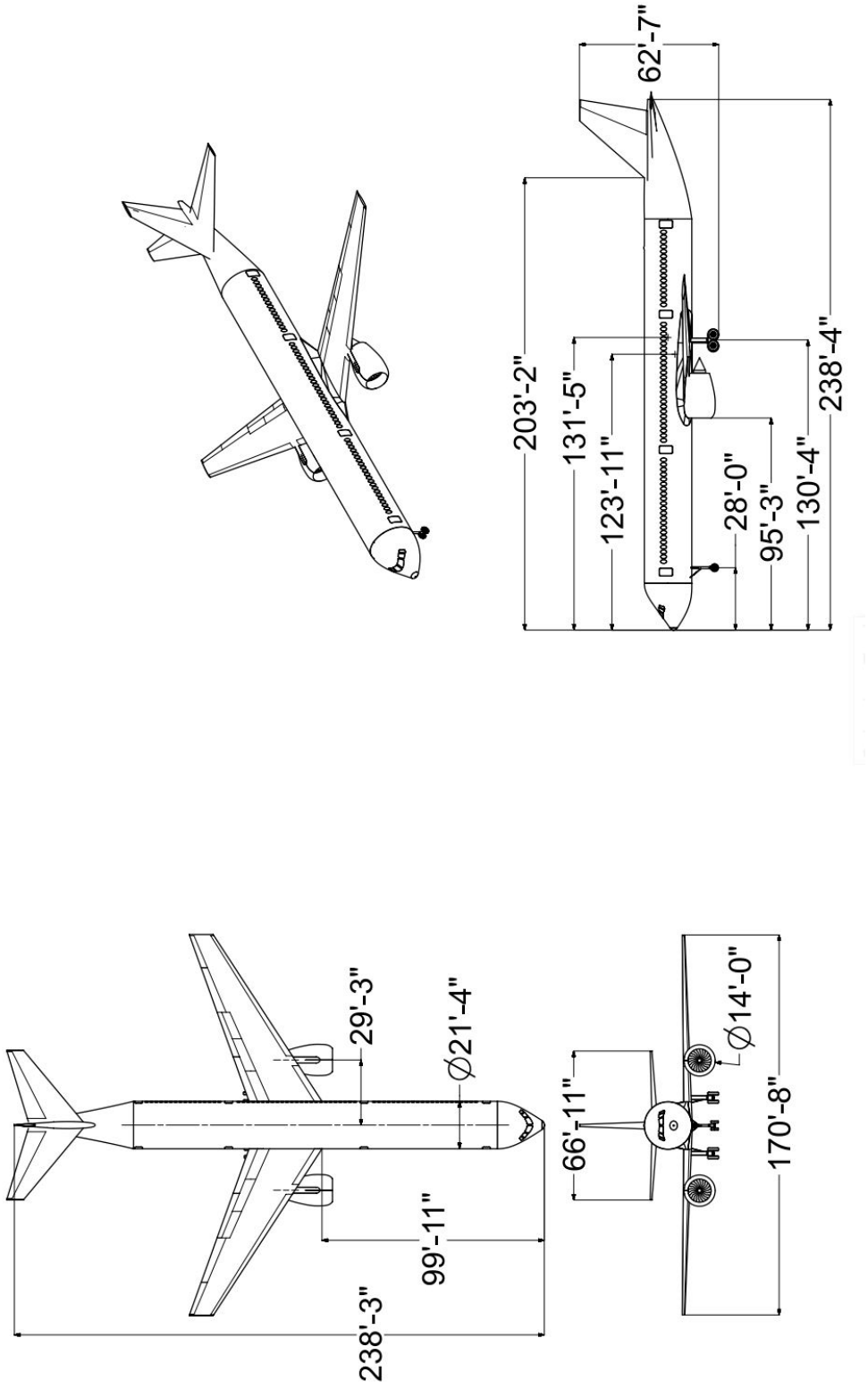

Figure 7 Three View Drawing of *Argo*

C. Internal Layout

The proposed interior layout is shown in Figure 8. The emergency exits are marked in Figure 8 with triangles. The aircraft has nine rows of business class seats and 35 rows of economy. Figure 9 shows a cutaway view of the interior layout of the *Argo*. A staircase leading to four below-deck lavatories is visible near the third emergency exit. The lavatories are discussed further below.

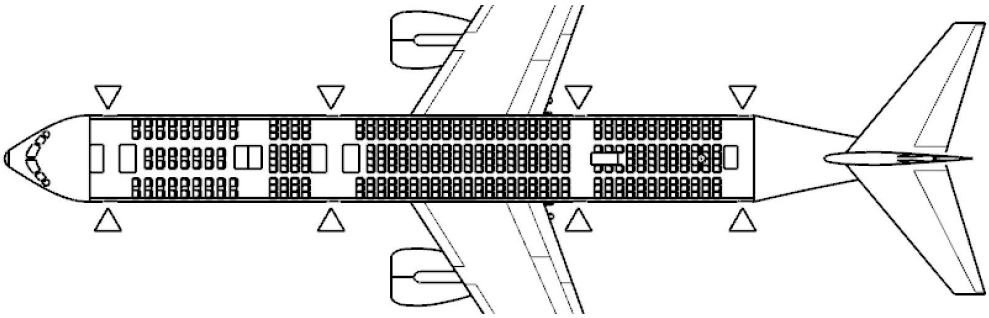

Figure 8 *Argo* Layout

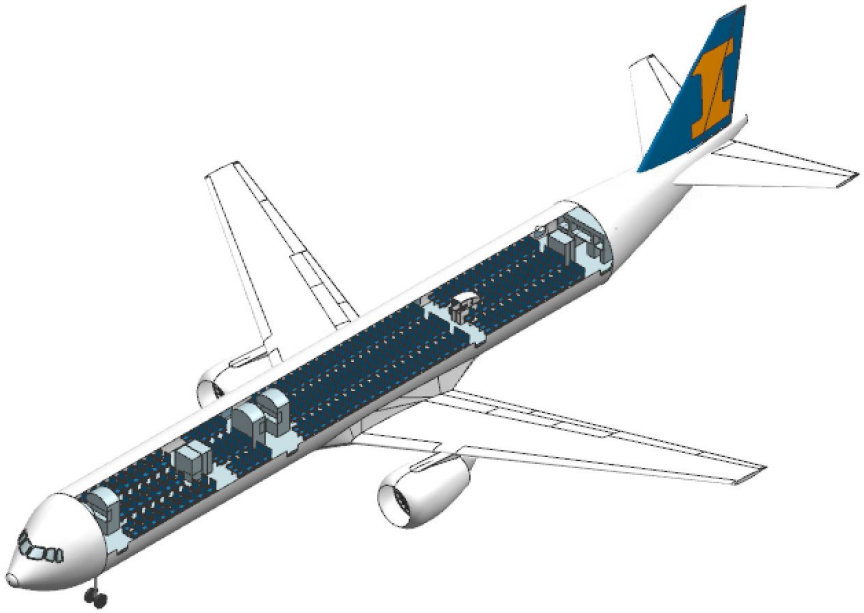

Figure 9 Cutaway View of *Argo* Interior

1. Business Class

The requirements in the RFP call for 50 business class and 350 economy class seats [1]. The business class section consists of nine rows in a 2-2-2 layout. The cross section of the business cabin is shown in Figure 11. These seats have a width and pitch of 21 in and 36 in, respectively. The aisle width in the business section is 28.5 in. A partition (not shown) separates the two classes, which along with the large seats and wide aisles will create an environment of

exclusivity and comfort for business travellers. A galley and pair lavatories will be available for the business customers. The dimensions of the business class seat are shown in Figure 10.

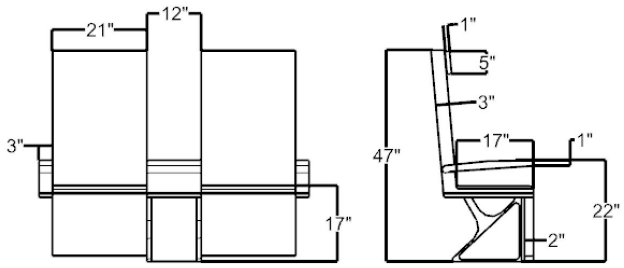

Figure 10 Business Seat Dimensions

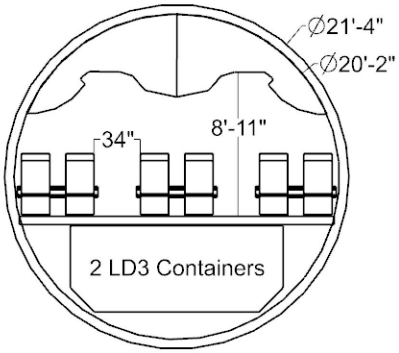

Figure 11 Business Cabin Cross Section

2. Economy Class

The economy section will be arranged a 3-4-3 layout as shown in Figure 13. Each seat will have a width and pitch of 18 in and 32 in, respectively. The seat dimensions are shown in Figure 12. Four rows of economy seats will be placed ahead of the second emergency exit in order to optimize the position of the exit rows. If airlines desire, these rows are in prime position for use as premium economy seats. The *Argo* has a total of seven lavatories. Fewer lavatories are needed than many long-haul airliners have because of the *Argo's* shorter design mission. In addition to the two lavatories in business class, a lavatory will be available on the main level of the economy cabin. Two galleys will service the economy section. The *Argo* will use fewer galleys in total than similarly sized aircraft because the anticipated missions are much shorter. As a result, fewer meals will be served, eliminating the need for large galleys. The most unique feature of the economy section is the below-deck lavatories. In order to save space on the main deck, four lavatories will be located below the floor of the cabin. This section will be pressurized and have a staircase leading down to it. The lower deck lavatories will be closed off during landing and take-off. Should an emergency occur while passengers are below decks, the staircase is located as close as possible to the emergency exits to give them time to get

up and out quickly. Airlines have used a similar configuration before and it is extremely popular among passengers [13]. Six seats will be placed in the last row of the aircraft to create space for the staircase.

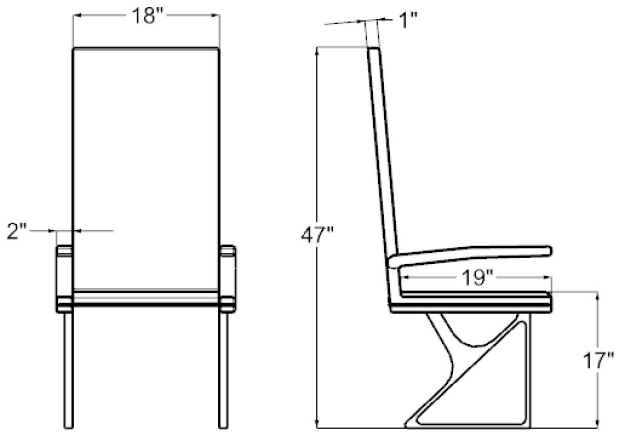

Figure 12 Economy Seat Dimensions

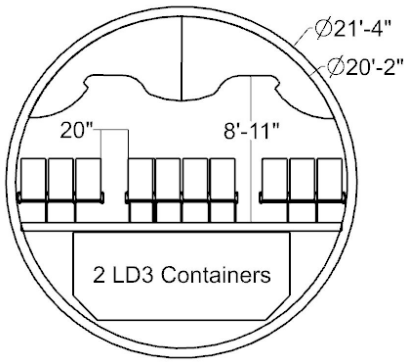

Figure 13 Economy Cabin Cross Section

3. Emergency Exits

The planned exits are marked with triangles in Figure 8. Each side of the aircraft will have four Class A emergency exits in compliance with FAA regulations [11]. Flight attendants will be stationed at each exit for takeoff and landing. Each exit will be equipped with an inflatable slide which can be used as a raft in a ditching scenario. These exits were intentionally arranged to avoid the need for over-wing exits. This was done because over-wing exits add complexity to the structure and certification process.

4. Baggage

Passengers will have the option of storing small items in overhead bins located throughout the cabin. This is in addition to the 5 ft^3 per passenger of baggage space located in the cargo hold [1]. The cargo hold is compatible with LD3 containers, which are the standard in aviation. Each LD3 container has 151.8 ft^3 of space [10]. Therefore, all

passenger and crew baggage fits into 14 LD3 containers which can be placed in the forward cargo compartment. This compartment has the capacity for up to 7 pairs of LD3 containers (14 total).

5. Flight Deck

The *Argo* features a state-of-the-art flight deck. As required by the RFP, the plane is flown by two pilots. The systems present in the flight deck are outlined in Section XI.H. The configuration follows all FAA regulations to keep the aircraft certifiable. The pilot viewing angles are shown from the captain's perspective in Figures 14 and 15.

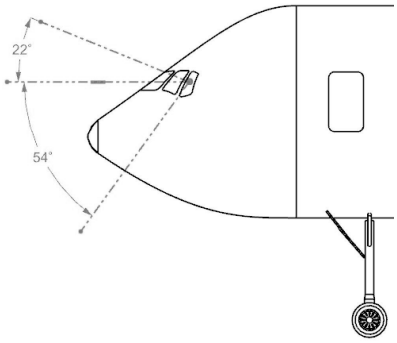

Figure 14 Pilot Viewing Angles - Side

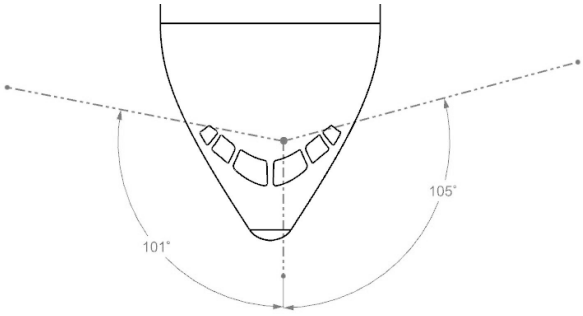

Figure 15 Pilot Viewing Angles - Top

V. Propulsion

A. Engine Selection

The main powerplant was sized by cruise requirements of the aircraft. At an altitude of 36,000 ft and a speed of Mach 0.82, the aircraft requires 17,850 lb of thrust per engine. Due to thrust lapse at high altitudes, this is equivalent to 81,300 lb of thrust per engine at sea level. Therefore, any engine used on the *Argo* should have more than 81,300 lb of available thrust. Excess thrust is important to reduce wear on the engine. Due to a five minute limit on maximum takeoff thrust, engines were compared on the basis of maximum continuous thrust. Table 7 shows the specifications for different engine options.

Table 7 Engine Selections

Engine	Certification Year	Max Thrust [lb]	TSFC [lb/lb/hr]
GE 9X	2020 (Expected)	105,000	0.466
Rolls Royce Trent 800	1995	92,940	0.562
Rolls Royce Trent 900	2004	84,000	0.522
Rolls Royce Trent 1000	2007	81,000	0.506
Rolls Royce Trent XWB-97	2017	97,000	0.477

The Rolls Royce Trent XWB-97 best suits the thrust requirement of the aircraft. It is capable of providing 84,000 lb of MCT per engine at sea level, and 27,000 lb of continuous thrust at the aircraft's cruise conditions. This fulfills the thrust requirement set at the top of climb. Excess thrust is retained for maneuvering capability as well as ETOPS performance. Having been certified in 2017, the Trent XWB demonstrates higher reliability and safety compared to older turbofan engines. Figure 16 shows the Trent XWB-97 and Table 8 details characteristics of the engine.

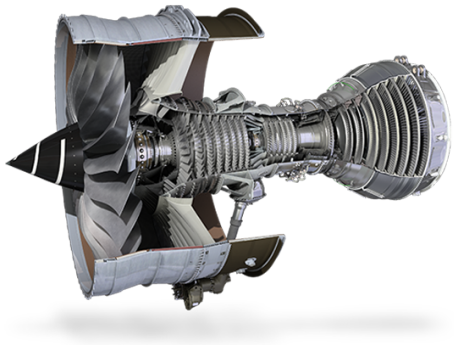

Figure 16 Trent XWB-97, Courtesy of Rolls-Royce [14]

Table 8 Trent XWB-97 Specifications [15]

Property	Value
Maximum Takeoff Thrust	97,000 lb
Max Continuous Thrust	83,984 lb
Bypass Ratio	9
Weight	16,642 lb
Fan Diameter	118 in
Overall Length	176.5 in
Maximum Radius	78.8 in

B. Engine Performance

The performance of the engine varies greatly according to the external conditions the engine experiences. Mach number and altitude both greatly affect the available thrust. Calculating these performance changes is extremely difficult without knowing the exact turbofan geometry, as geometry greatly affects the amount of ram drag. Daidzic [16] suggests a method that uses atmospheric data to calculate both TSFC and available thrust. Daidzic's equations can be applied at any airspeed and at any atmospheric condition to find equivalent values of TSFC and thrust. The calculations are carried out from Mach 0 to Mach 0.82, and 0 ft to 36,000 ft to create an envelope of expected TSFCs and thrusts when takeoff thrust is being applied. These functions are plotted and shown below in Figures 17 and 18. This model is validated by HBPR data and similar graphs found in Raymer [5].

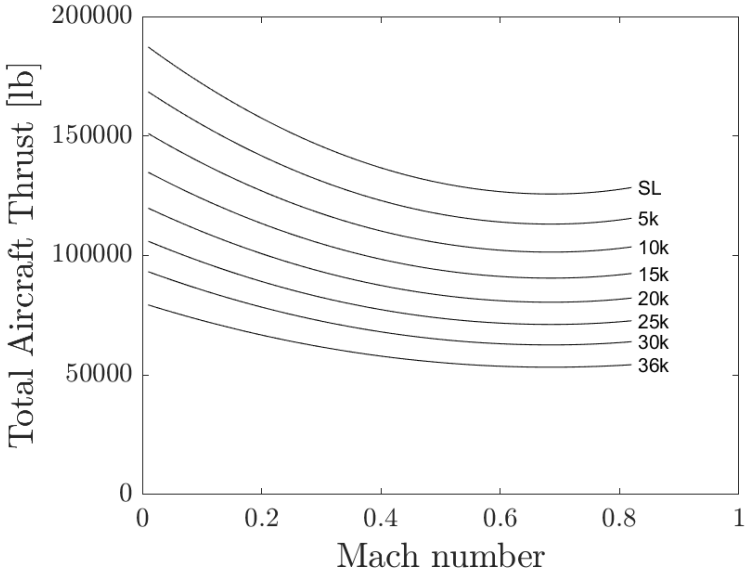

Figure 17 Available Thrust as a function of Mach number and altitude for Trent XWB-97

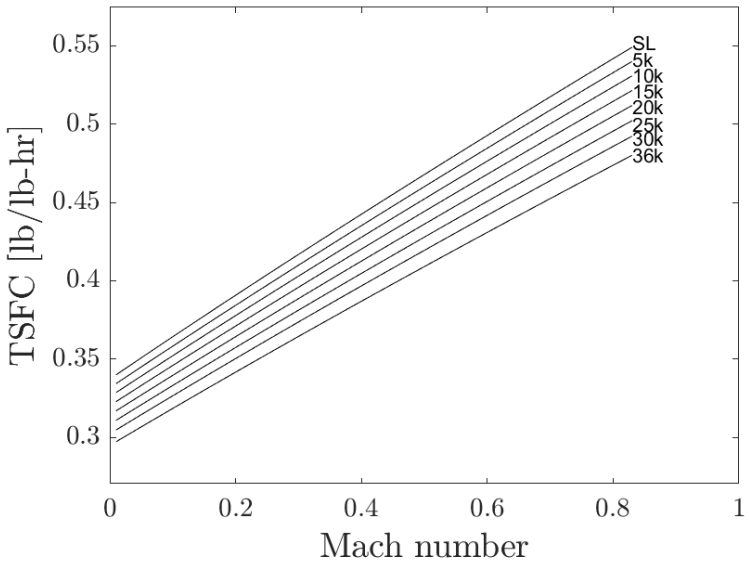

Figure 18 TSFC as a function of Mach number and altitude for Trent XWB-97

C. Inlet and Nacelle Design

One of the most important aspects of engine integration is the size of the inlet. In transonic operation regimes, the flow which the front of the engine experiences is too fast and needs to be slowed down. Raymer suggests an inlet speed of approximately Mach 0.4 to Mach 0.6 [5]. Since much more compression occurs at the inlet, the inlet needs to

be smaller than the fan diameter. Using a cruise speed of Mach 0.82 and a target inlet speed of Mach 0.6, the inlet area is calculated to be 0.75 times the size of the fan area.

Raymer specifies multiple constraints for the nacelle [5]. Firstly, the lip radius of the inlet should be between 3-5% of the radius of the inlet. The inner and outer lip radii were set to 8% and 4% of the inlet radius. This decreases distortion of the air as it enters the inlet [5]. Additionally, nacelle design was derived from existing aircraft with the same engine. A spike was included in the exhaust to reduce noise. Figure 19 shows the engine with integrated nacelle and exhaust spike as well as the pylon.

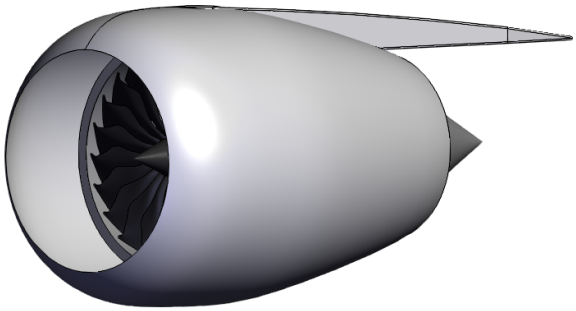

Figure 19 Trent XWB-97 with Nacelle

VI. Aerodynamics

A. Airfoil Selection

1. Empirical Analysis

Transonic drag was a major consideration in the airfoil choice for the wing. While the drag divergence Mach number (M_{dd}) has multiple definitions, the Delta method defines M_{dd} as the Mach number where $\frac{\partial C_D}{\partial M} = 0.1$ [17]. This definition was used for aerodynamic analyses of the *Argo*. As the flow accelerates past M_{dd}, $\frac{\partial C_D}{\partial M}$ increases and wave drag penalties are incurred. It was imperative to select an airfoil that had a high M_{dd} associated with it. Initially, NACA 6-series airfoils and supercritical (SC) airfoils were investigated. However, since SC airfoils have an M_{dd} of about 0.1 higher than their 6-series counterparts [18], only NASA SC airfoils were considered. A trade study was conducted to determine a suitable airfoil for the wing.

Since the weight of the aircraft varies throughout cruise, analyses were performed at a point corresponding to the start of cruise. Given a cruise Mach number of 0.82, the cruise C_L for the aircraft was calculated as 0.539. Choices like the NASA SC(2)-1008 were eliminated because their design C_l was not close to the anticipated aircraft C_L in cruise.

The Korn equation [18] was used to estimate the M_{dd} of wings as a function of the airfoil $\frac{t}{c}$ and $\Lambda_{c/4}$. This relationship is shown in Figure 20. A higher $\frac{t}{c}$ corresponds to a lower M_{dd} for a given $\Lambda_{c/4}$.

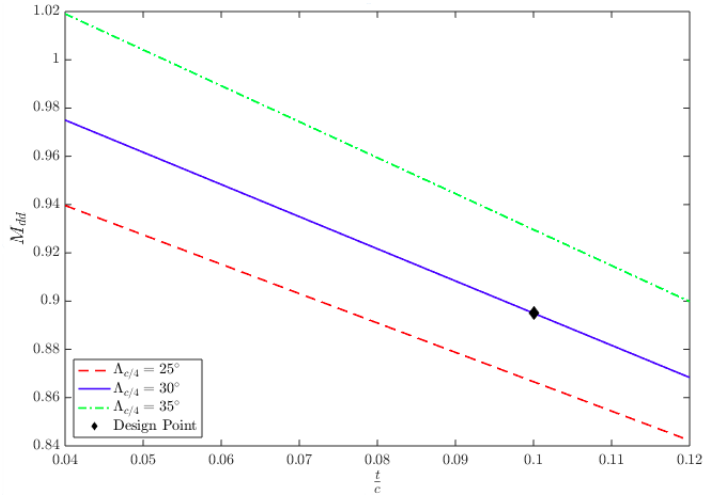

Figure 20 Effect of $\frac{t}{c}$ on M_{dd} [18]

Figure 21 illustrates the effect of $\frac{t}{c}$ on wing structural weight using an empirical relationship from Raymer [5]. For a constant $\Lambda_{c/4}$, the wing structural weight decreased as $\frac{t}{c}$ increased. Thus, there is a trade-off between structural weight and aerodynamic performance.

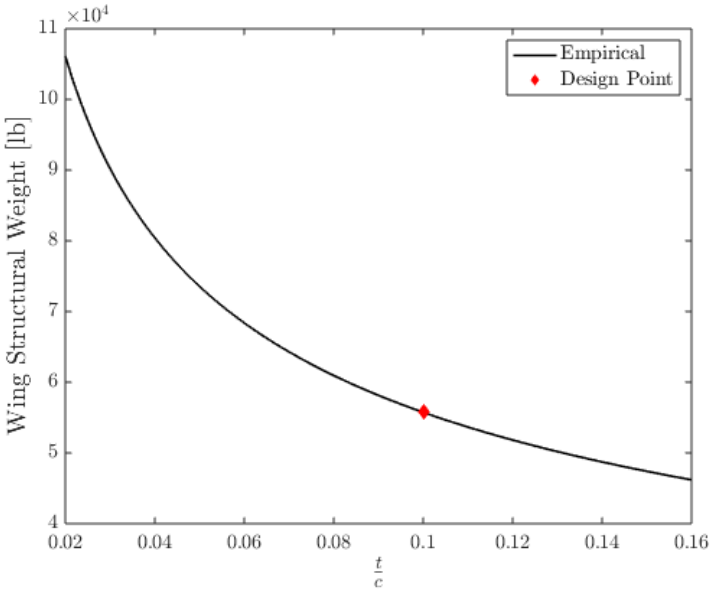

Figure 21 Effect of $\frac{t}{c}$ on Wing Structural Weight [5]

2. XFLR5 Analysis

Based on the constraints imposed on the design lift coefficient and the thickness ratio of airfoils, three airfoils were chosen for XFLR5 analysis: NASA SC(2)-0406, NASA SC(2)-0410, and NASA SC(2)-0610. Plots obtained from XFLR5 analysis are representative of the general trends of the airfoils. Plots of C_l vs α, $\frac{C_l}{C_d}$ vs α, and C_m vs α are shown in Figures 22, 23, and 24 respectively.

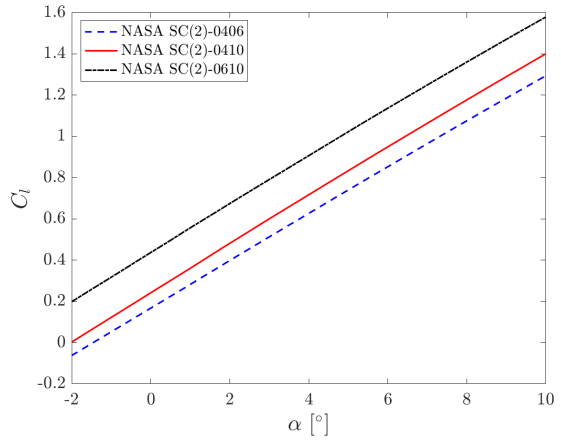

Figure 22 Lift Coefficient versus Angle of Attack

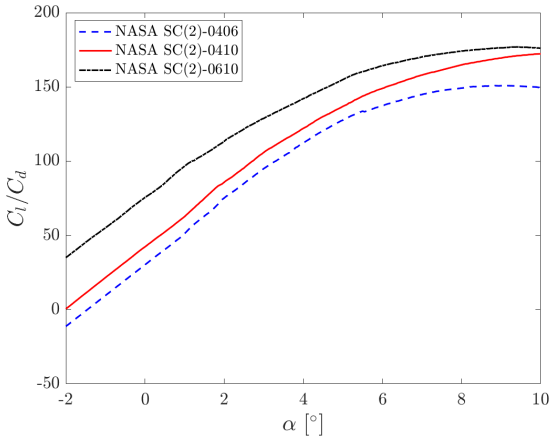

Figure 23 Lift-to-Drag Ratio versus Angle of Attack

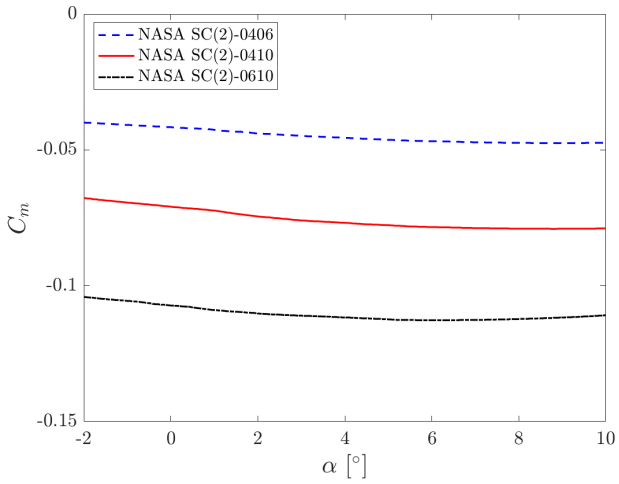

Figure 24 Pitching Moment Coefficient versus Angle of Attack

Figure 22 shows that the NASA SC(2)-0610 exhibits the best lifting characteristics followed by the NASA SC(2)-0410 and the NASA SC(2)-0406. Figure 23 shows the same trends for lift-to-drag ratio. It can be seen from Figure 24 that the NASA SC(2)-0610 has the largest magnitude of pitching moment coefficient. This would have to be countered by a larger horizontal tail than the other two airfoils. Thus, the NASA SC(2)-0610 was not considered.

The NASA SC(2)-0406 has the lowest magnitude of pitching moment coefficient; this would potentially mean a smaller horizontal tail to satisfy longitudinal trim. However, a 10% thickness ratio was chosen as a compromise between aerodynamic considerations and weight considerations from Figures 20 and 21. Thus, the NASA SC(2)-0410 was chosen for the wing.

Airfoil coordinates for the NASA SC(2)-0410 were obtained from the UIUC Airfoil Coordinates Database [19]. These coordinates are plotted and shown in Figure 25.

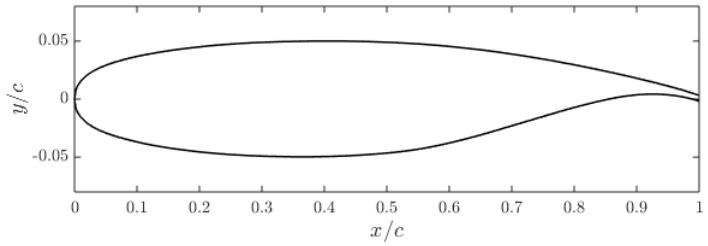

Figure 25 NASA SC(2)-0410

B. Wing Design

1. Wing Sweep

Wing sweep is an important design parameter as the aircraft will be cruising in the transonic regime. Although increasing $\Lambda_{c/4}$ lowers the wave drag penalty by increasing M_{dd}, it also lowers the wing C_L. Figure 20 illustrates the effects of sweep and was used to select a $\Lambda_{c/4}$ of 30°. In addition to being in line with typical values of sweep used in airliners, a $\Lambda_{c/4}$ of 30° led to an M_{dd} of 0.88 via the Delta Method and the Korn estimate [17, 18, 20].

2. Span

The span constraint on the *Argo* is a 171 ft limit to keep the aircraft within Class D limits [2]. Class D compliance allows the *Argo* to service airports accessible to low-capacity short-range aircraft as well as high-capacity high-range aircraft. Thus, a wing span of 170.7 ft was chosen.

3. Wing Area and Aspect Ratio

A preliminary sizing analysis was used to iterate over several combinations of aspect ratio and wing area. Details of the process can be found in Section III. This process resulted in an aspect ratio range of 7 to 8, and a wing area range from 4,000 ft^2 to 4,500 ft^2. While aerodynamic efficiency drives design on long-haul flights, weight is a more important consideration on short-haul flights [7]. Thus, wing area was selected to be 4,000 ft^2, resulting in an aspect ratio of 7.3.

4. Taper Ratio

While taper ratio (λ) did not affect the sizing analysis, it impacts lift distribution and tip stall. A λ below 0.2 negatively affects tip stall [21]. Further, a λ of 0.3 yields the lowest induced drag parameter [21]. Thus, λ was chose to be 0.3.

5. Wing Twist

Wash-out is desired to minimize the possibility of tip stall because it would reduce aileron effectiveness. To completely eliminate tip stall, a complex non-linear twisting function would have to be applied to the wing. High fidelity models of aerodynamically twisted wings at transonic speeds were unavailable. Therefore, a geometric linear twist of -4° was applied based on analysis of twist angles of similar aircraft in Sadraey [22].

6. Wing Positioning

The choice of vertical positioning for the wing is described in Section IV. The placement along the longitudinal axis was determined while analyzing longitudinal stability. The wing was positioned to ensure an aft center of gravity position such that the power-on static margin was at least 10%. This resulted in an apex of 92.5 ft and a X_{LEMAC} of 115.3 ft. Further details are presented in Section VIII.

7. Dihedral

A dihedral angle of 3° met lateral stability requirements. An engine clearance requirement of 5° between the bottom of the landing gear and the bottom of the engine was satisfied. Figure 26 demonstrates sufficient engine clearance.

Figure 26 Engine Clearance

8. Angle of Incidence

The wing is designed to be fixed incidence owing to the mechanical complexity associated with a variable incidence wing. The wing incidence angle is determined via longitudinal trim analysis. A wing incidence of 3° was chosen such that the deck angle remains below 3°. This constraint was determined by considering passenger ergonomics. At the cruise condition, α = 2°, and therefore, the deck angle is 2°.

9. Summary of Wing Design Parameters

Figure 27 and Table 9 summarize the major dimensions of the wing.

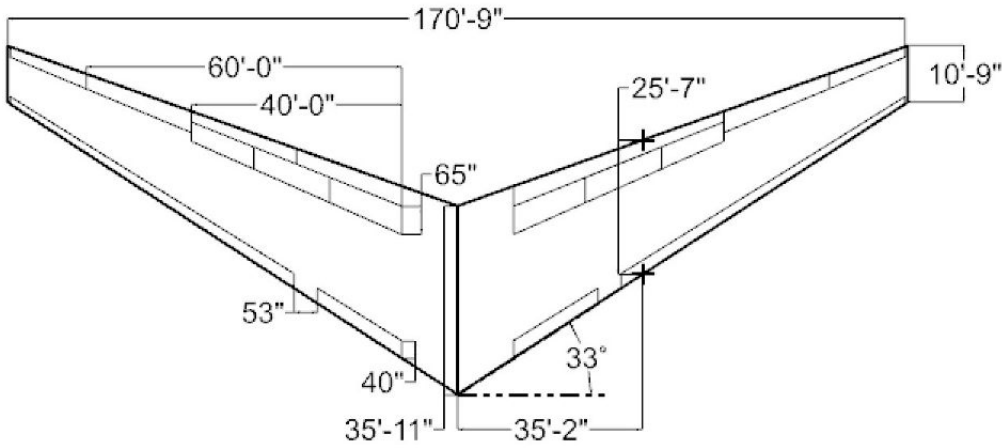

Figure 27 Wing Dimensions

Table 9 Summary of Wing Design Parameters

Parameter	Value
S_{ref}	4,000 ft^2
AR	7.28
b	170.7 ft
$\Lambda_{c/4}$	30°
c_r	36.0 ft
MAC	25.7 ft
i_w	3.0°
α_{twist}	-4.0°
λ	0.30
Γ	3.0°
LEMAC	115.3 ft
Apex	92.5 ft

C. High Lift System

Takeoff and landing performance was considered more important than maneuverability for jet transports of this size, so the high lift system was designed before ailerons.

The sizing of the high lift system is driven by $C_{L_{max}}$ at takeoff and landing. These numbers are determined from takeoff field length and landing field length requirements. The TOFL is achieved with a $C_{L_{max}}$ at takeoff of 1.95 and the LFL is achieved with a $C_{L_{max}}$ at landing of 2.25.

An overview of the different choices available for leading and trailing edge devices was found in Raymer [5]. Krueger flaps and slats were considered for the leading edge system. Krueger flaps are effective but more intricate to manufacture. Slats are simpler, provide sufficient lift increment, and produce an insignificant effect on pitching moment.

Trailing edge flap considerations involved plain flaps, single slotted, double slotted, and triple slotted flaps. Plain flaps were rejected from consideration because they are mainly used on smaller aircraft at lower speeds. They produce significant drag but are mechanically simple. While slotted flaps are structurally intricate, they provide a sizable lift increment. Leading edge slats and trailing edge Fowler flaps were selected and sized on the basis of $C_{L_{max}}$ at takeoff and landing.

The lift increment from slats and Fowler flaps was estimated using techniques presented in Raymer [5]. Table 10 provides the breakdown of lift contributions from the high-lift system. Assuming a takeoff flap deflection of 15° and a landing flap deflection of 35°, the takeoff lift increment sums to 0.72 and the landing lift increment sums to 1.03. The $C_{L_{max}}$ of the clean wing was estimated at 1.25. Therefore $C_{L_{max}}$ at takeoff sums to 1.96 and $C_{L_{max}}$ at landing sums to 2.28. Both these numbers meet $C_{L_{max}}$ requirements.

Table 10 Breakdown of Lift Contributions from High-Lift System

Parameter	Fowler Flaps	Slats
$\frac{c'}{c}$	1.2	1.1
Hinge Line	23.3°	31.9°
$\Delta C_{L_{max}}$ (Takeoff)	0.542	0.177
$\Delta C_{L_{max}}$ (Landing)	0.774	0.252

The results of the high-lift system sizing are presented in Table 11.

Table 11 Summary of High-lift System Capabilities

Flight Condition	Required C_{Lmax}	Designed C_{Lmax}
Takeoff	1.95	1.96
Landing	2.25	2.28

D. Drag Build-up

Several methodologies were combined to construct a drag build-up for the *Argo*: Raymer [5], the Delta method [17], and McCormick [23].

1. Methodologies

Parasitic drag was estimated using techniques presented in Raymer [5]. The components considered were the fuselage, wing, nacelles, horizontal tail, vertical tail, landing gear, and fuselage upsweep. Leakage and protuberance

drag was estimated as 3% of C_{D_0}. C_f was evaluated using the assumption of fully turbulent flow. This provides a slightly conservative estimate of parasitic drag. The induced drag is computed as $C_{D_i} = \frac{CL^2}{\pi e AR}$ where e is estimated via Raymer to account for sweep and aspect ratio. The induced drag includes the lift component of wave drag. Further, Raymer is used to estimate the drag due to flap deployment.

The Delta method splits up drag contributions at cruise as parasitic drag, compressibility drag, induced drag, and wing pressure drag [17]. In determining the parasitic drag contributions, the Delta method only accounts for the wing, fuselage, vertical tail, and horizontal tail. It is important to understand the difference in assumptions between methods of predicting drag before computing percentage differences. The Delta method does not account for nacelles and upsweep. If those contributions are subtracted, C_{D_0} estimated by the Delta method and Raymer only varies by 2%. Thus, the parasitic drag is confidently estimated. Since the Delta method and Raymer method closely correlate, the Raymer method of parasitic drag estimation is used as it is more robust to changes in flight conditions.

The Delta method was used to compute the zero lift wave drag at cruise. To mitigate the robustness issue, plots from the Delta method were digitized over a small range of Mach numbers from 0.78-0.88. Trim drag was computed using equations in McCormick [23].

2. Drag Build-up

Table 12 shows a complete drag build-up of the aircraft at takeoff, cruise, and landing. A takeoff speed of 1.15 V_{stall} was chosen. The cruise speed of the *Argo* is Mach 0.82. The landing speed is 1.15 V_{stall}. It is worth noting that the stall speeds at takeoff and landing differ and are computed using $C_{L_{max}}$ at these conditions.

Takeoff and landing computations were performed at sea level at 15°C DISA. Cruise computations were performed at 0° DISA and a cruise altitude of 36,000 ft. The cruise drag components in Table 12 correspond to the top of climb. $\frac{S_{wet}}{S_{ref}}$ for the aircraft is 6.845.

Table 12 Drag Build-up for the *Argo*

Drag Component		Takeoff	Cruise	Landing
Parasitic Drag	Fuselage	0.0065	0.0055	0.0068
	Wing	0.0055	0.0058	0.0055
	Nacelle	0.0014	0.0012	0.0015
	Vertical Tail	0.0009	0.0009	0.0009
	Horizontal Tail	0.0017	0.0018	0.0017
	Aft Upsweep	0.0020	0.0020	0.0020
	Landing Gear	0.0105	0	0.0105
	Leakage & Protuberance	0.0008	0.0005	0.0009
	Total	0.0293	0.0177	0.0298
Lift Induced Drag		0.1558	0.0208	0.2074
Zero-lift Wave Drag		0	0.0008	0
Flap Drag	Takeoff: δ = 15°, Landing: δ = 35°	0.0485	0	0.0988
Trim Drag	Takeoff: i_t = -4.3°, δ_e = -5.0° Cruise: i_t = -1.1°, δ_e = 0.0° Landing: i_t = -4.5°, δ_e = -5.0°	0.0055	0.0005	0.0120
Summary	C_L	1.475	0.539	1.701
	C_D	0.2391	0.0398	0.3480
	$\frac{L}{D}$	6.17	13.54	4.89

E. Aircraft Lift Curves and Drag Polars

The lift curves and drag polars for the *Argo* are theoretically constructed. The lift curves for takeoff, cruise, and landing are plotted in Figure 28. Takeoff and landing lift coefficients are adjusted by the lift increment at takeoff and landing to account for flap deployment. The resultant drag polars are plotted in Figure 29. Key mission points are highlighted in these plots. Key aircraft information at takeoff, cruise, and landing are tabulated in Table 13.

Table 13 Key Aircraft Information

Parameter	Takeoff	Cruise	Landing
C_L	1.475	0.539	1.701
C_D	0.2391	0.0398	0.3480
α	7.3°	2.0°	6.3°

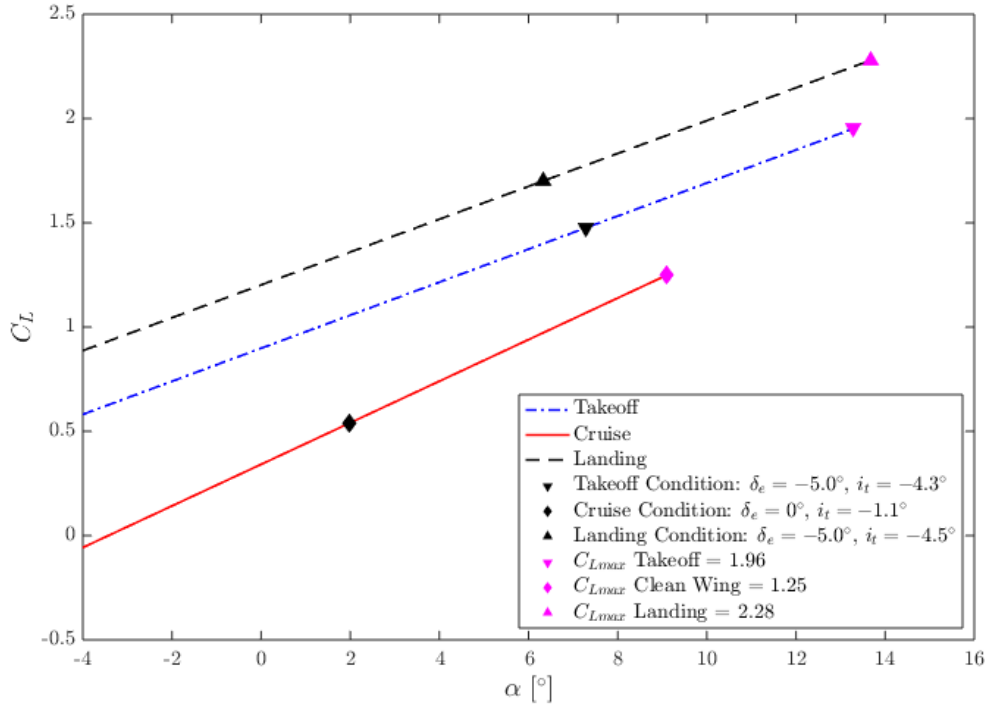

Figure 28 Aircraft Lift Curves

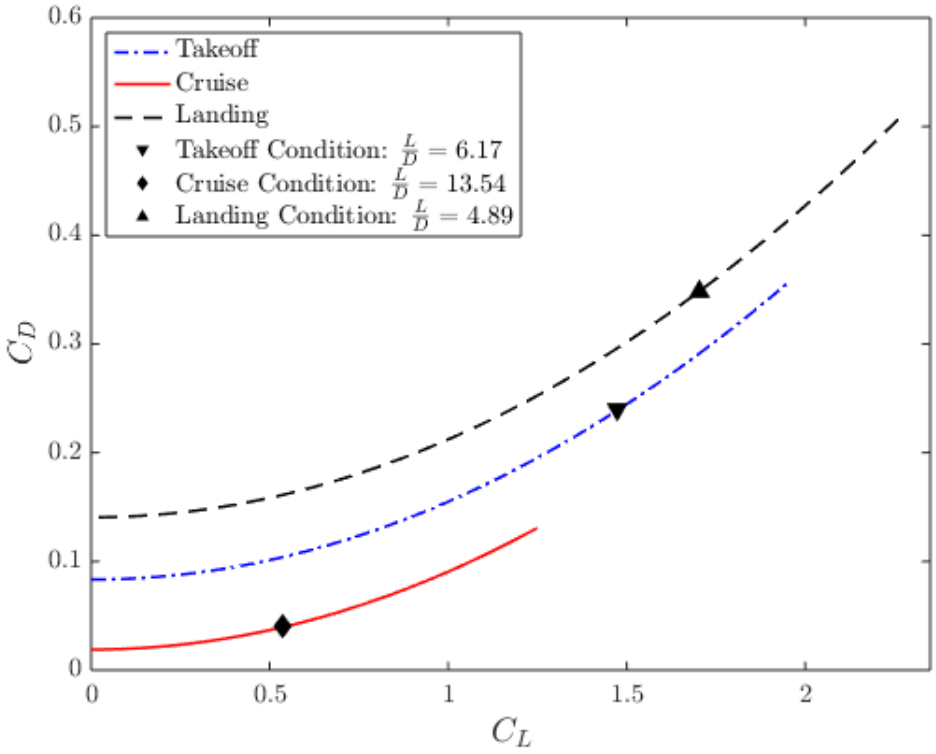

Figure 29 Aircraft Drag Polars

VII. Performance

The performance of commercial transport aircraft is vital to their economic viability. The RFP [1] outlines multiple performance requirements, as described in Table 1. Performance capabilities are analyzed on a segment by segment basis. The following analysis was completed for the aircraft with the payload prescribed by the RFP and performing a 3,500 nmi mission [1].

A. Requirements

As described in Table 1, the aircraft must be able to perform a mission of 3,500 nmi, divert to an alternate airport 200 nmi away, and hold 5% contingency fuel for the main 3,500 nmi mission. It must also have a BFL less than 9,000 ft. With the aircraft's current configuration, all of these requirements are met. Since performance is a primary driver of requirements, the aircraft's configuration was ultimately changed structurally and aerodynamically to meet the performance requirements. BFL is met by appropriately choosing takeoff thrust and range is met by properly sizing fuel tanks. One requirement not met is the approach speed of 145 KCAS. The approach speed at the end of the design mission is 147 KCAS. As this is a tradable requirement, more emphasis was placed on minimizing the size of high lift devices to reduce weight. Additionally, aircraft such as the Boeing 777-300ER have an approach speed of 150 KCAS [24]. With an approach speed 2 KCAS above a tradable requirement, the approach performance was deemed sufficient.

B. Takeoff

The RFP [1] requires a BFL of 9,000 ft. Raymer's method was used to calculated BFL and average thrust on takeoff [5]. Raymer's equation yields a BFL of 9,000 ft when using 70,000 lb of thrust per engine [5]. Since the engine is sized primarily for cruise, using takeoff thrust is unnecessary to achieve a BFL of 9,000 ft. Takeoff thrust for the Trent XWB is limited to 5 minutes [15] as the takeoff thrust condition can shorten the lifespan when used too often.

The takeoff field length was calculated by splitting the takeoff roll into multiple segments: a ground-roll length, a transition length, and a climb length. Transition and climb length were found using Raymer [5], while the ground length was calculated using two methods. The first method for determining ground-roll distance is presented by Raymer [5]. This method splits the thrust terms and aerodynamic terms into two separate variables for calculation, K_T and K_A, and integrates them with respect to V_{TO}^2. This equation yields a ground-roll length of approximately 4,950 ft.

The second method used to calculate ground-roll length was a time step integration using the aircraft's MTOW configuration. This method gives an approximate ground-roll distance of 4,890 ft. There is reasonable confidence in the accuracy of these calculations because the difference between them is a mere 60 ft.

The transition length is defined as the distance the aircraft travels from the moment of liftoff to a stabilized climb angle. The aircraft also accelerates from V_{LOF} to V_2, so the transition speed is assumed to be the average of the two speeds, V_{TR} [5]. Raymer presents a method for determining the radius of the transition arc, which is used to

calculate both the horizontal and vertical distance travelled through transition. Raymer also suggests a climb flight path angle determined by the aircraft's thrust-to-weight ratio (T/W) and the lift-to-drag ratio (L/D).

With these equations, the transition length is determined to be 940 ft. The vertical distance travelled in this segment is 150 ft, meaning the aircraft has cleared the 35 ft obstacle through the transition period, and a length for climb out will not be necessary [1].

Table 14 Take Off Field Length by Segment

Segment	Length [ft]	Method
Ground-Roll	4,950	Raymer
Ground-Roll	4,890	Time Step
Transition	940	Raymer
Climb	0	Raymer
Total Field Length	5,890	Raymer
Total Field Length	5,930	Time Step
Balanced Field Length	9,000	Raymer

Takeoff field length segments were evaluated at ISA + 15°C, MTOW, and the thrust required to meet a BFL of 9,000 ft. Although the TOFL is consistently below the target takeoff field length of 9,000 ft, the BFL is not. BFL is determined by the accelerate-stop and accelerate-go distances in the event of an engine failure. Per Raymer, V_1 is iterated until the braking distance at V_1 is equal to the distance needed to clear a 35 ft obstacle [5]. At a takeoff speed of 152 KIAS and equivalent lift and drag characteristics, the BFL is determined to be 9,000 ft.

C. Climb

Climb to cruise is performed using MCT in order to reach a maximum ROC. This unrestricted climb burns the least amount of fuel as well as taking the least time to reach cruise altitude [25]. However, due to FAA regulations, the aircraft cannot exceed 250 KCAS under 10,000 ft. To mitigate this issue, the aircraft will accelerate to 250 KCAS under 10,000 ft and accelerate to cruise speed once passing that threshold. Climbing in this configuration burns 13,600 lb of fuel. A time step integration method was used to determine the fuel burn in 30 second increments. All parameters were updated according to atmospheric effects, namely available thrust and TSFC. During climb, the aircraft travels 85 nmi over the 13 minute period it takes to reach the cruising altitude of 36,000 ft.

D. Cruise

The weight of the aircraft at the end of climb is used as the initial weight for cruise performance. The speed is held constant at Mach 0.82 at an altitude of 36,000 ft. A weight step integration is used to determine fuel usage, time, and range. Fuel burn increments of 100 lb are used to create a high fidelity estimation of range and fuel usage. Cruise

ends when the aircraft is 92 nmi from the destination. The *Argo* burns 105,300 lb of fuel during cruise, which covers 3,270 nmi.

E. Descent & Loiter

Descent is flown at cruise speed above 10,000 ft and at 250 KCAS below this altitude. Idle thrust is used per Raymer [5]. A rate of descent of -1,500 ft/min yields a descent time of 24 minutes. Between 5,000 ft and 2,000 ft the aircraft will travel at 200 KCAS, and below 2,000 ft to ground level the aircraft will decelerate linearly to the approach speed, which is 145 KCAS. Also accounted for in the descent is a five minute loiter at 5,000 ft. No ground travel is accounted for in this segment. The aircraft's speed throughout loiter is set to 200 KCAS. Descent consumes 2,200 lb of fuel, which is 2% of the mission fuel. Fuel burn during loiter, which accounts for 650 lb of fuel, is also included in this total.

F. Landing

Landing is broken into the same segments as take off, and is computed identically. An approach distance, flare distance, free roll distance, and ground roll distance are calculated. The free roll distance is a three second period upon touchdown before the brakes are applied. The landing analysis was performed at 87.5% of the MTOW to account for a potential emergency landing. MLW is approximately 437,000 lb. The value of each segment and their sum are tabulated in Table 15.

Table 15 Landing Field Length by Segment

Segment	Length [ft]	Method
Approach	430	Raymer
Flare	590	Raymer
Free Roll	660	Raymer
Braking Ground Roll	3,170	Raymer
Braking Ground Roll	3,180	Time Step
60% Ground Roll Margin (14 CFR § 121.195)	2,900	-
Total Landing Field Length	7,750	Raymer
Total Landing Field Length	7,760	Time Step

G. Divert, Fuel Reserves, & Fuel per Segment

The RFP [1] requires fuel reserves to climb, cruise, loiter, and land at an alternate airport 200 nmi away. During the divert segment, cruise is required to last at least five minutes. This sets the divert cruise conditions to a speed of Mach 0.82 and an altitude of 25,000 ft, resulting in a cruise time of approximately seven minutes. The aircraft requires 16,600 lb of fuel to meet divert reserves, and another 6,400 lb for the contingency fuel required by the RFP. The required fuel broken into segment by segment quantities is presented in Table 16.

Table 16 Fuel Weight per Segment of 3,500 nmi Mission

Description	Fuel Weight [lb]
Warm-up, taxi & takeoff	4,800
Climb	13,600
Cruise	105,300
Descent	2,600
Approach, landing, & taxi	1,800
Mission Fuel	128,100
Reserves	
Climb	6,000
Divert	2,100
Descent & 30 Minute Hold	8,500
Contingency fuel	6,400
Reserve Fuel	23,000
Total Fuel	151,100

H. Service Ceiling

An aircraft's service ceiling is determined by the altitude where the ROC is less than 500 ft/min[5]. For this aircraft, the conditions of the service ceiling will determined by design cruise Mach, the weight at top of climb after taking off at MTOW, and maximum continuous thrust. With these conditions determined, the ROC can be found for an entire range of altitudes. The altitude at which the ROC becomes less than 500 ft/min is 38,000 ft. Another important parameter is the absolute ceiling, where the aircraft cannot possibly climb any higher. This altitude is determined at the same conditions prescribed above, and occurs at an altitude of approximately 40,000 ft at the same weight as described above.

I. Flight Envelope

An aircraft's flight envelope details the minimum and maximum speeds it is capable of flying as a function of altitude. This is important for pilots to know to safely operate the aircraft. The method used to generate the flight envelope, seen in Figure 30, involves calculating the stall speed and speeds at which the ROC is equal to zero. These speeds are found using two constants, A and B, which translate to the aerodynamic and weight properties respectively. The absolute minimum and maximum speeds, as well as the absolute ceiling, are found using the flight envelope.

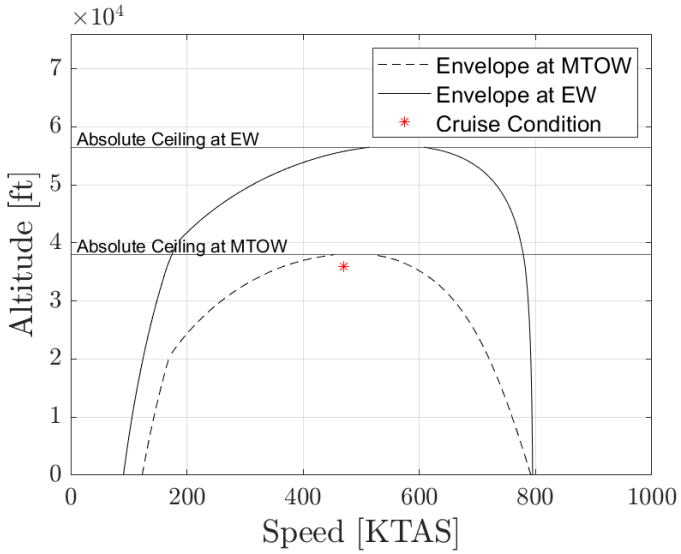

Figure 30 Flight Envelope at MTOW and EW

J. Payload - Range

The RFP [1] details a mandatory amount of cargo (passengers and their bags) to operate the 3,500 nmi mission. However, it is possible to increase range by decreasing the amount of passengers, and thus the overall weight, on the aircraft. A payload-range diagram allows aircraft operators to view increases in range with decreases in payload. Seen in Figure 31, when carrying the maximum payload, which includes 17,500 lb of revenue payload, the *Argo* can fly 2,800 nmi. When carrying the payload specified in the RFP, the *Argo* is able to fly 3,500 nmi [1]. To fly further than 3,500 nmi, the payload must decrease. The diagram shows a maximum range of approximately 4,580 nmi, which is the condition with zero payload and maximum fuel.

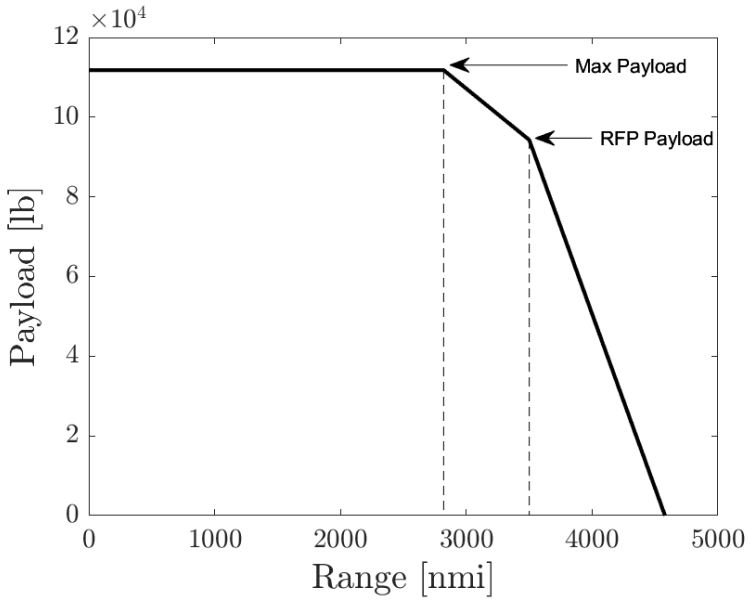

Figure 31 Payload-Range Diagram

K. Drag per Segment

It is important to determine the drag which the aircraft will encounter at each condition in order to properly size the engine. The aircraft's engines are sized almost entirely by the performance needed at cruise. The range of drag which the aircraft experiences is shown in Table 17.

Table 17 Drag per Segment of 3,500 nmi Mission

Description	Drag [lb]
Takeoff	0 - 65,200
Start of Climb	37,900
Top of Climb	36,000
Middle of Cruise	31,500
End of Cruise	27,700
Descent	25,000 - 40,000
Approach, landing	77,000 - 0

L. Specific Excess Power

When evaluating overall performance of an aircraft, the specific excess power is vital in understanding the maneuvering capabilities at different conditions. The specific excess power is similar to the rate of climb; in this case, it is maximized at all conditions. Excess power is typically normalized by the weight of the aircraft, and shown as a contour plot against speed and altitude. The specific excess power plot at TOC can be seen below in Figure 32. This plot shows a maximum altitude of 40,000 ft at TOC weight and a specific excess power of 100 ft/s at sea level and 300 KTAS.

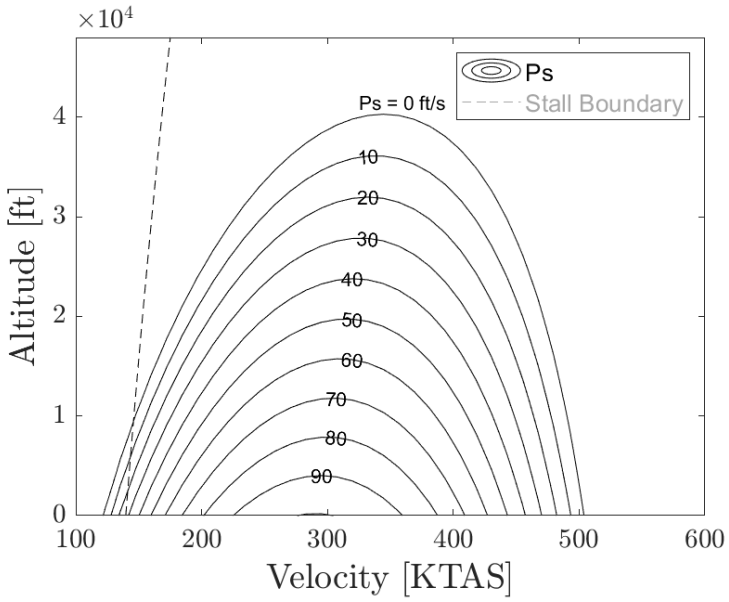

Figure 32 Specific Excess Power at TOC Weight

VIII. Stability and Control

A. Stabilizer Design

1. Horizontal Stabilizer

The minimum horizontal tail area and wing placement for sufficient longitudinal stability and controllability were determined via a trade study using a scissor diagram. The ratio of horizontal tail area to wing area $\frac{S_t}{S_{ref}}$ was determined as a function of the center of gravity position h for each critical boundary. The resulting plot is shown in Figure 33.

The controllability boundary was determined via pitching moment equilibrium at the landing condition with flaps deployed. The neutral stability boundary was found by setting $C_{M\alpha}$ to zero. A minimum of 10% power-on static margin was desired at the most aft center of gravity location. However, since the computations were carried out with the power-off assumption, an allowance of 1.5% static margin was made to compensate for power-on effects [5]. The neutral stability boundary was offset by 0.115 in the negative x axis to obtain the stability boundary in the scissor plot. The landing gear line confirms that the main landing gear is placed behind the aft center of gravity location. The center of gravity travel is used to determine the wing position for a balanced design.

From the plot, a minimum horizontal stabilizer area ratio of 0.28 is recommended such that the stability, controllability, landing gear, and center of gravity travel requirements are met. Consequently, an area of 1,120 ft^2 was chosen for the horizontal stabilizer. The choice of tail area yielded a horizontal tail volume coefficient V_H of 1.08. This is in line with longitudinal stability expectations of jet transports from Torenbeek [26].

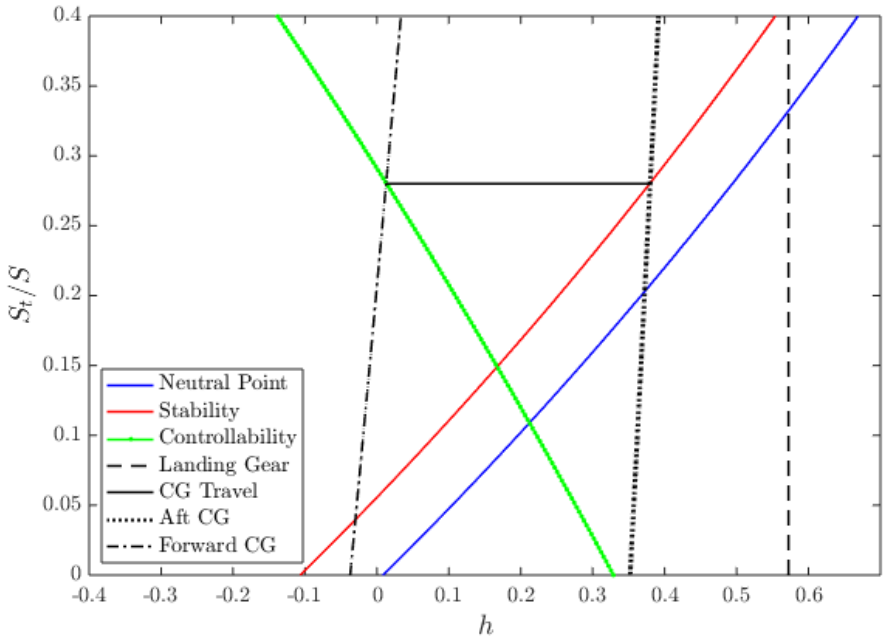

Figure 33 Scissor Diagram for Horizontal Stabilizer Sizing

A supercritical airfoil of comparable thickness to the wing was sought for the horizontal stabilizer. This ensures the effectiveness of the horizontal stabilizer at higher speeds. A symmetric supercritical airfoil was chosen initially and checked against stability and controllability requirements later in the design process.

The airfoil on the horizontal stabilizer need not be symmetric. An upside-down cambered airfoil could be used instead. However, this option is more applicable in designs where the tail is required to produce relatively large tail loads. Since this is not the case for this design, a symmetric airfoil was chosen.

The NASA SC(2)-0010 airfoil was chosen for the horizontal tail. The normalized section is plotted in Figure 34. The coordinates were obtained from the UIUC Airfoil Coordinates Database [19].

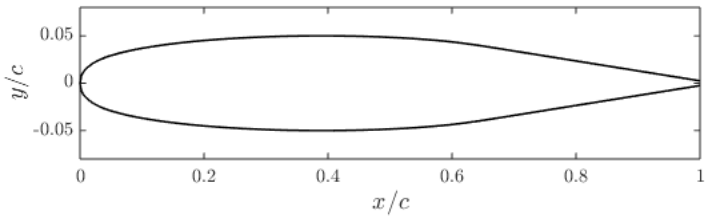

Figure 34 NASA SC(2)-0010

A taper ratio of 0.3 was chosen due to the relatively low induced drag at this taper ratio [21]. As AR decreases, structural weight decreases and drag increases. Since the horizontal stabilizer produces a fraction of the parasitic drag produced by the wing, the structural weight of the horizontal stabilizer is more important than the reduction of drag [27].

Consequently, an AR of 4 was chosen from a similarity analysis of a list of aircraft in Torenbeek [26]. A $\Lambda_{c/4}$ of 35° was chosen to delay the onset of M_{dd} on the horizontal stabilizer such that empennage effectiveness is guaranteed at higher Mach numbers.

In addition to having an elevator, the horizontal stabilizer is designed to be variable incidence. This is done to ease the elevator's effort during flight. Using just the elevator to trim would result in large deflection angles at takeoff and landing. This would result in a large drag penalty. Additionally, there is a limit on maximum elevator deflection to avoid elevator stall. Further, a variable incidence horizontal stabilizer is compliant with current industry standards. Design parameters for the horizontal stabilizer are summarized in Table 18.

Table 18 Horizontal Stabilizer Design Parameters

Parameter	Value
b	66.9 ft
c_r	25.4 ft
λ	0.3
$\Lambda_{c/4}$	35°
AR	4
S_t	1,120 ft^2
V_H	1.08

A top-down dimensioned view of the horizontal stabilizer is shown in Figure 35.

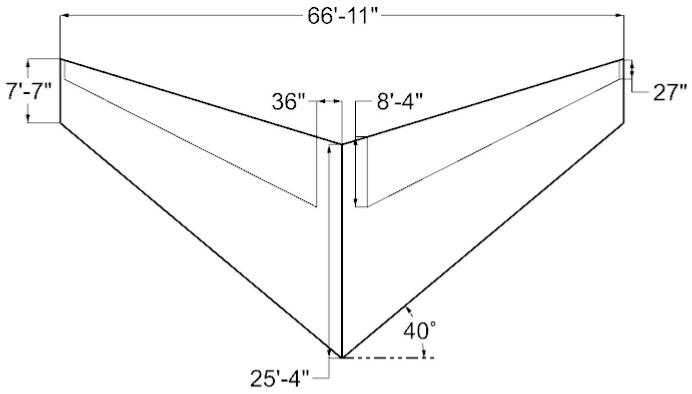

Figure 35 Horizontal Stabilizer

2. Vertical Stabilizer

The area of the vertical stabilizer is driven by static lateral and directional stability requirements. $C_{l\beta}$ and $C_{n\beta}$ are comprised of wing, fuselage, and vertical tail contributions. An estimate of S_v was chosen during the preliminary design phase. This was iterated upon such that the stability derivatives fell in ranges recommended by Sadraey [22]. This estimate was tested while determining engine position along the wing such that the rudder could counter the yaw

produced due to one engine inoperative situations. This resulted in a vertical tail area of 625 ft^2. The choice of S_v yielded a vertical tail volume ratio of 0.096, which is in line with comparable aircraft from Torenbeek [26].

A taper ratio of 0.3 was selected to keep the induced drag due to the vertical stabilizer at a minimum [21]. The geometric aspect ratio of the full span vertical stabilizer was chosen as 3 from analysis of vertical stabilizers of similar aircraft from Torenbeek [26]. Thus, the aspect ratio of the half-span vertical tail is 1.5. This is different from the effective aspect ratio of 2.33, which accounts for the reduced efficiency of half-span wings as compared to full-span wings and is used in a few aerodynamic calculations. A quarter-chord sweep of 35° was chosen to delay the onset of M_{dd} on the vertical stabilizer.

The vertical tail uses the same airfoil as the horizontal tail. A symmetric section is necessary so that no side force is produced when the rudder is aligned with the vertical stabilizer. A summary of the design parameters for the vertical stabilizer is presented in Table 19. A dimensioned view of the vertical stabilizer is shown in Figure 36.

Table 19 Vertical Stabilizer Design Parameters

Parameter	Value
h_v	30.6 ft
c_r	31.4 ft
λ	0.3
$\Lambda_{c/4}$	35°
AR	1.5
S_v	625 ft^2
V_V	0.096

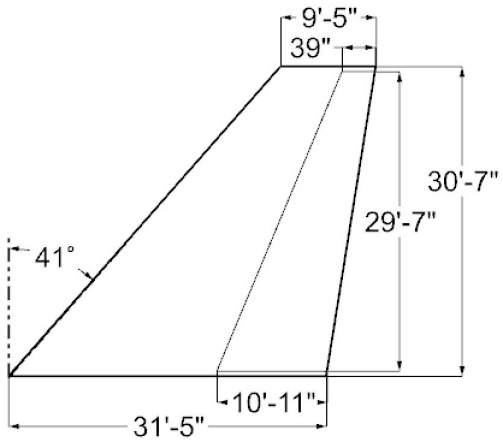

Figure 36 Vertical Stabilizer

B. Control Surface Sizing

1. Rudder Sizing

The rudder was sized such that it could adequately trim in one engine inoperative situations at the minimum controllable speed (14 CFR §25.149) [28]. Rudder effectiveness was preliminarily chosen and iterated upon such that the engine placement was in line with similar aircraft. The rudder was sized at a speed 10% lower than the theoretical minimum controllable speed for a slightly conservative design. This process resulted in a rudder effectiveness, τ_r, of 0.6. This resulted in a rudder chord ratio of 0.4 [22]. A span ratio of 1 was chosen. A dimensioned view of the rudder is shown in Figure 36.

2. Aileron Sizing

The wing trailing edge is split between trailing edge high lift devices and ailerons. The space allocation depends on what is more important for the aircraft: roll control or takeoff and landing performance. Maneuverability is not as important as takeoff and landing performance for jet transports. Consequently, the high lift system was designed first and the remaining space was allocated to outboard ailerons. The outboard aileron effectiveness, τ_a, was chosen from Sadraey as 0.41, resulting in a chord ratio of 0.2 [22]. This helps in maintaining continuity with the trailing edge flap system. The outboard aileron occupies the outer 20% of the half-span. However, outboard ailerons are not sufficient for lateral-directional controllability in all flight conditions.

At high Mach numbers, ailerons are subject to a phenomenon called aileron reversal. Wing flexibility is one cause. If the load due to aileron deflection acts at a point behind the elastic axis of the wing, this results in wing twist. The aileron control power reverses sign and an undesired rolling moment is produced. This happens at the aileron reversal speed. However, at low Mach numbers, the possibility of adverse yaw exists. When ailerons are deflected at low speeds, the section with the aileron deflected upwards produces more lift and consequently more induced drag. This drag differential causes an undesired yawing moment that needs to be countered.

A trade study was conducted to find an aileron arrangement that could handle aileron reversal and adverse yaw. One metric used to find this arrangement was aileron control power. This was computed by using a strip method [5]. Possible solutions include stiffening the wing, employing only inboard ailerons, employing inboard ailerons or flaperons in addition to outboard ailerons, moving the outboard ailerons more inboard, or employing roll spoilers.

Making the wing stiffer would add structural weight. This goes against the design philosophy of the aircraft, which is to reduce weight wherever possible. Using just inboard ailerons would not work; this would reduce the aileron control power since the moment arm would decrease. Employing inboard ailerons or flaperons in addition to outboard ailerons would mean that the complexity of the high lift system (and consequently weight) would have to increase. Moving the outboard ailerons inboard would not work for the same reason as solely having an inboard aileron.

Roll spoilers were chosen for three reasons. First, at high Mach numbers, roll spoilers can be used as the primary roll control device. Second, roll spoilers are capable of handling adverse yaw at low Mach numbers. If there is a drag increment on one side of the wing, the roll spoiler on the opposite side can deflect to produce the same drag increment so that a yawing moment will not be generated. Third, roll spoilers can overlap with the trailing edge devices. When overstowed, the gap and overlap can be tuned to provide lift augmentation. This will be examined in the next phase of design. Dimensioned views of the ailerons and spoilers are shown in Figure 27.

3. Elevator Sizing

The elevator size was preliminarily selected on the basis of historic data of jet transports [20]. A span ratio and chord ratio of 1 and 0.3 were chosen, respectively. Longitudinal stability analyses were performed with these numbers and produced satisfactory results at different flight conditions. A dimensioned view of the elevators is shown in Figure 35. Table 20 summarizes the parameters involved in control surface design.

Table 20 Control Surface Design Parameters

Parameter	Rudder	Elevator	Aileron
Chord Ratio	0.40	0.30	0.20
Span Ratio	1	1	0.19
δ_{max}	±30°	±20°	±30°

C. Longitudinal Static Stability

1. Trimmability

Longitudinal trim analyses were performed at takeoff, cruise, and landing conditions by solving the trim system of equations. At takeoff and landing, the lift increment and the pitching moment contribution from flaps were incorporated. The pitching moment about the aerodynamic center was adjusted for sweep, taper, and twist.

While the system comprises two equations, there are four unknowns: α, i_t, i_w, and δ_e. Since the wing is designed to be fixed-incidence, i_w is specified a priori. i_w was chosen as 3° after a few iterations to achieve balance between low enough deck angle and trim drag. While low trim drag is desired from an aerodynamic efficiency standpoint, a low deck angle is desired from an ergonomic standpoint. Research suggests that female flight attendants are likely to overload themselves if they have to frequently move heavy trolleys on an inclined cabin floor [29].

Either i_t or δ_e were specified during these analyses. At cruise, δ_e of 0° was desired. Thus, α and i_t were solved for. At takeoff and landing, there are several physically permissible combinations of α, i_t and δ_e that solve the trim system of equations. To fully understand the ramifications of picking one combination over the other, higher fidelity analysis is required. The set of values presented in the report were obtained by constraining δ_e to be −5°. The set of α,

i_t, and δ_e for each flight condition are specified in Table 21. A plot of C_M versus α at the different flight conditions using i_t and δ_e as specified in Table 21 is shown in Figure 37.

Table 21 Trimmed Flight Conditions

Parameter	Takeoff	Cruise	Landing
α	6.9°	1.1°	-2.0°
i_t	-4.3°	-1.1°	-4.5°
δ_e	-5.0°	0.0°	-5.0°
i_w	3.0°	3.0°	3.0°

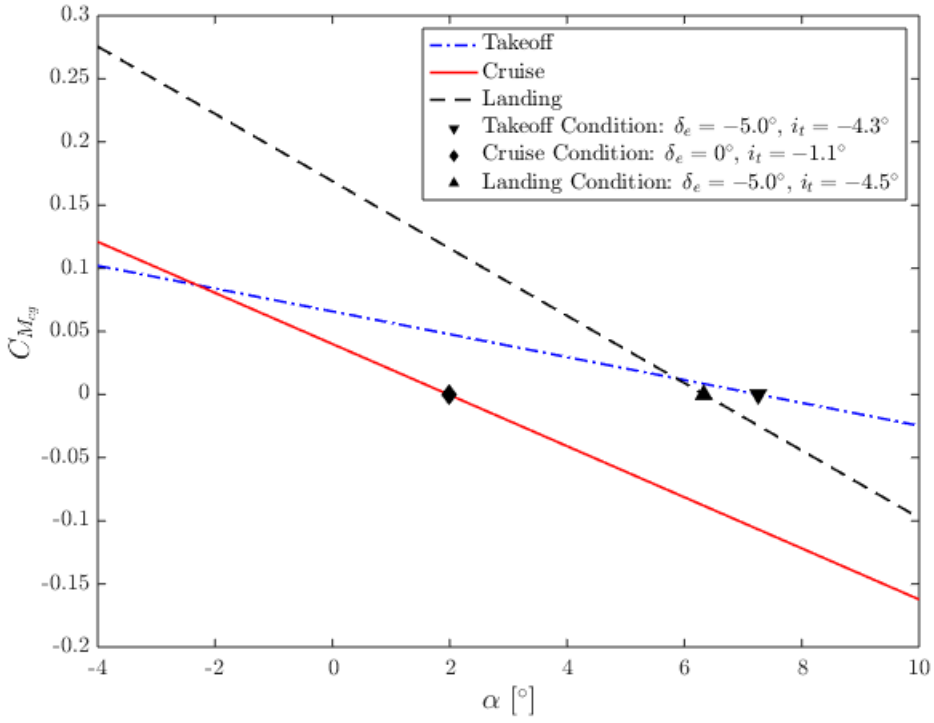

Figure 37 Aircraft Pitching Moment Curves

2. Static Stability

In addition to trimmability, longitudinal static stability was ensured by evaluating the static margin at the forward and aft center of gravity locations. Static margin was evaluated as $-\frac{C_{M_\alpha}}{C_{L_\alpha}}$. 10% power-on static margin was desired at the most aft center of gravity location. Since the trim requirements were determined at power-off conditions, a 1.5% allowance is made to compensate for power-on effects [5]. Horizontal tail area and wing position were iterated until this criteria was satisfied.

The neutral point of the aircraft is the aircraft's aerodynamic center. To compute the neutral point at cruise, $C_{M\alpha}$ was set to zero to solve for the center of gravity location. Table 22 details the center of gravity positions used in this analysis (in absolute terms and % MAC), neutral points, and static margins. The origin of the absolute reference frame is at the tip of the aircraft nose. Figure 38 shows how the neutral point of the aircraft varies with Mach number. A static margin range of 11.4% - 33.8% is achieved in flight. This is shown in the aircraft trim diagram in Figure 39.

Table 22 Static Margins

Flight Condition		CG [ft]	CG [% MAC]	Neutral Point [% MAC]	Static Margin [% MAC]
Cruise	Forward	122.1 ft	26.6%	51.3%	24.7%
	Aft	124.6 ft	36.3%	51.3%	15.0%
Takeoff		125.1 ft	38.0%	49.4 %	11.4%
Landing		119.3 ft	15.7%	49.5%	33.8%

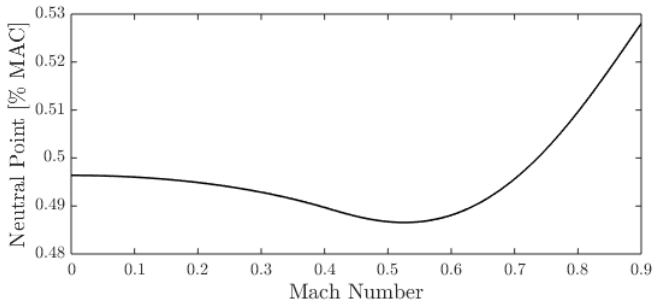

Figure 38 Variation of Neutral Point with Mach Number

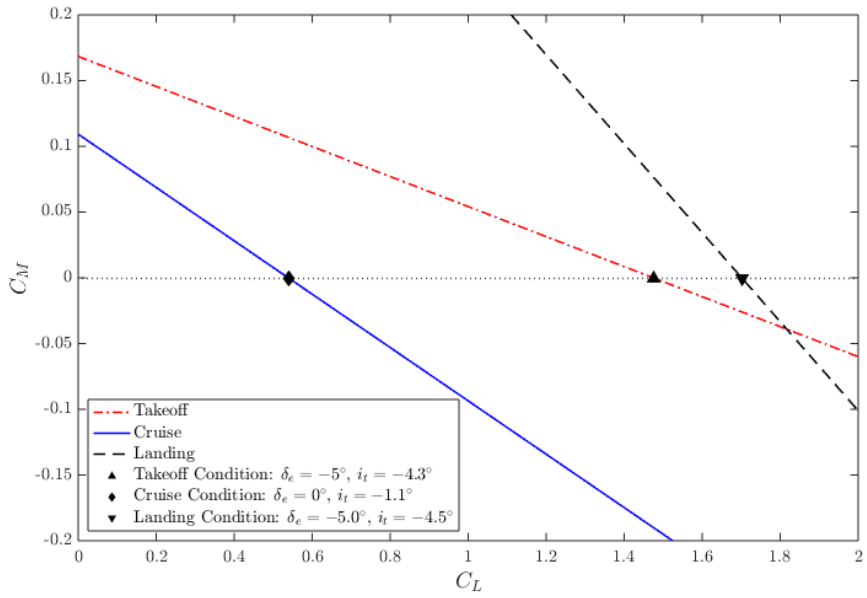

Figure 39 Aircraft Trim Curves

D. Stability Control Derivatives

1. Longitudinal Stability and Control Derivatives

Longitudinal stability and control derivatives that were used in the longitudinal static stability and longitudinal dynamic stability analyses are presented in Table 23. These derivatives are presented at a cruise condition corresponding to top of climb.

Table 23 Longitudinal Derivatives

Derivative	Value	Method
$C_{L\alpha}$	0.0997 deg^{-1}	Raymer [5]
$C_{M\alpha}$	-0.0202 deg^{-1}	Raymer [5]
ϵ_{α}	0.4523	Sadraey [22]
C_{Mq}	-0.5005 deg^{-1}	Nelson [30]
$C_{M\delta e}$	-0.0341 deg^{-1}	Sadraey [22]
$C_{L\delta e}$	0.0089 deg^{-1}	Sadraey [22]

Since $C_{M\alpha}$ is negative, the aircraft is longitudinally statically stable. The pitch stiffness (ratio of $C_{M\alpha}$ to $C_{L\alpha}$) determines how stable the aircraft is, i.e. its static margin. As the magnitude of pitch stiffness increases, the static margin increases. ϵ_{α} represents how the downwash angle at the tail changes with angle of attack. C_{Mq} determines how changes in pitch rate affect the pitching moment of the aircraft. A negative C_{Mq} is essential to meet the short period damping requirement [31]. The response of pitching moment coefficient to changes in elevator deflection is given by $C_{M\delta e}$. Similarly, the response of the lift coefficient to changes in elevator deflection is given by $C_{L\delta e}$.

2. Lateral-Directional Stability and Control Derivatives

Lateral and directional stability and control derivatives that were used in the lateral and directional static and dynamic stability analyses are presented in Table 24. These derivatives are presented at a cruise condition corresponding to top of climb.

Table 24 Lateral-Directional Derivatives

Derivative	Value	Method
$C_{l\beta}$	-0.0044 deg^{-1}	Roskam [32]
C_{lp}	-0.0121 deg^{-1}	Nelson [30]
$C_{n\beta}$	0.0063 deg^{-1}	Raymer [5]
C_{nr}	-0.0067 deg^{-1}	Nelson [30]
$Cl_{\delta a}$	0.0016 deg^{-1}	Raymer [5]
$Cl_{\delta r}$	0.0010 deg^{-1}	Nelson [30]
$Cn_{\delta a}$	-0.0003 deg^{-1}	Nelson [30]
$Cn_{\delta r}$	-0.0034 deg^{-1}	Sadraey [22]

A negative $C_{l\beta}$ implies static lateral stability. C_{lp} is the roll damping derivative. It is necessary for C_{lp} to be negative to meet roll handling requirements [31]. A positive $C_{n\beta}$ implies static directional stability. Since C_{nr} is the yaw damping derivative, it must be negative to meet yaw handling requirements [31]. $Cl_{\delta a}$ and $Cn_{\delta r}$ are the aileron and rudder control power.

E. Directional Stability

Directional stability is demonstrated by the rudder adequately trimming in one engine inoperative situations at the minimum controllable speed. Rudder effectiveness τ_r was chosen from Sadraey. Since assumptions of zero sideslip angle and zero aileron deflection were made, the rudder was sized at 90% of the minimum controllable speed to yield a slightly conservative estimate for rudder size. The maximum deflection of the rudder is ±30°. Even though one engine inoperative is the worst case, the rudder deflection was selected to be ±25° in this scenario. The drag due to the inoperative engine was estimated via Torenbeek [26]. This was followed by the computation of the rudder control power, $Cn_{\delta r}$. Finally, the engine moment arm was computed.

This design depends largely on the vertical tail area and the rudder effectiveness, τ_r. Fixing τ_r at 0.6 while iterating through rudder deflections resulted in the engine moment arms in Table 25.

Table 25 Engine Moment Arms

Condition	δ_r	$C_{n\delta r}$	Moment Arm
Takeoff	±25.0°	-0.0029 deg^{-1}	29.3 ft
Landing	±3.6°	-0.0030 deg^{-1}	29.6 ft

The drag from one engine inoperative is much larger in the takeoff case than in the landing case. Consequently, the rudder has to counteract a much larger yaw in the takeoff case. This is why the rudder was sized by the yaw it has to counteract at the minimum controllable speed at takeoff.

F. Lateral Dynamic Stability

An expression for roll rate in terms of speed, aileron control power, roll damping derivative, and aileron deflection was found using Nicolai [31]. The aileron control power was computed using the strip method suggested in Raymer [5].

Since V_2 is decided by the manufacturer, a value of 1.2 V_{stall} was chosen. Further details can be found in Section VII.K. V_2 is the worst case scenario that the aircraft has to be compliant with in terms of time taken to roll. Per FAA requirements, the roll time for banking from +30° through -30° should be fewer than 11 s [33]. Table 26 demonstrates that the designed aileron meets these requirements.

Table 26 Aileron Peformance

Parameter	Value
V_2	285.9 ft/s
$C_{l\delta_a}$	0.0013 deg^{-1}
C_{lp}	-0.0097 deg^{-1}
δ_a	15°
Bank Angle	60°
Roll Rate	6.59 deg/s
Roll Time	9.1 s

G. Flying Qualities Analysis

The flying qualities of an airplane are stability and control characteristics that form the pilot's opinion about the ease with which the airplane can be controlled in steady and maneuvering flight [30]. The Cooper-Harper Handling Qualities Rating Scale is used by test pilots to provide a numerical rating of their opinion of the aircraft [5]. The scale ranges from 1 to 10, with 1 indicating the best handling characteristics and 10 the worst. Flying qualities are evaluated based on MIL-F-8785C standards for large transport aircraft. Based on this, Level 1 flying qualities are desired for the Argo [34].

1. Longitudinal Flying Qualities Analysis

The linearized longitudinal equations of motion were adopted from Nelson [30]. Stability and control derivatives involved in the calculation of the state space matrices were estimated from Nelson [30], Raymer [5], Roskam [32], and Sadraey [22]. In addition to stability and control derivatives, the equations of motion required the three mass moment of inertia of the airplane. These were estimated from Roskam Part V [6].

The linearized system is shown in Equation 1 in the form $\dot{x} = Ax + Bu$, where x is the set of states $[u, w, q, \theta]$ and u $[\delta_e]$ is the set of inputs.

$$\begin{bmatrix} \dot{u} \\ \dot{w} \\ \dot{q} \\ \dot{\theta} \end{bmatrix} = \begin{bmatrix} X_u & X_w & 0 & -g \\ Z_u & Z_w & u_0 & 0 \\ M_u & M_w & M_q & 0 \\ 0 & 0 & 1 & 0 \end{bmatrix} \begin{bmatrix} u \\ w \\ q \\ \theta \end{bmatrix} + \begin{bmatrix} 0 \\ Z_{\delta e} \\ M_{\delta e} \\ 0 \end{bmatrix} \begin{bmatrix} \delta_e \end{bmatrix} \tag{1}$$

After substituting the stability and control derivatives calculated at cruise in Equation 1, the state space matrices A and B were computed.

Upon calculating the eigenvalues of A, the system was found to be unstable. Thus, a state feedback controller was implemented to stabilize the system. The gain matrix K was iterated upon until the system met Level 1 longitudinal flying qualities. The control law is shown below.

$$\delta_e = -0.0005u + 0.0051w + 2.0404q + 0.0950\theta$$

Table 27 shows the Level 1 requirements for longitudinal dynamic stability [30], the open-loop system characteristics, and the closed loop system characteristics. The *Argo* satisfies all of these requirements.

Table 27 Longitudinal Dynamic Stability

	Phugoid ω_n	**Phugoid ζ**	**Short Period ω_n**	**Short Period ζ**
Level 1 Requirement	-	$\zeta > 0.04$	2.513 rad/s < ω_n < 3.769 rad/s	0.35 < ζ < 1.30
Open Loop System	0.076 rad/s	-0.025	1.309 rad/s	0.359
Closed Loop System	0.081 rad/s	0.041	2.891 rad/s	0.678

2. Lateral-Directional Flying Qualities Analysis

As with longitudinal dynamics, the lateral-directional linearized equations of motion were adopted from Nelson[30]. The stability and control derivatives were estimated from Nelson [30], Raymer [5], Roskam [32], and Sadraey [22].

The linearized system is shown in Equation 2 in the from $\dot{x} = Ax + Bu$, where x is the set of states $[\beta, p, r, \phi]$ and u $[\delta_a, \delta_r]$ is the set of inputs.

$$\begin{bmatrix} \dot{\beta} \\ \dot{p} \\ \dot{r} \\ \dot{\phi} \end{bmatrix} = \begin{bmatrix} \frac{Y_\beta}{u_0} & \frac{Y_p}{u_0} & -(1 - \frac{Y_r}{u_0}) & \frac{g\cos\theta_0}{u_0} \\ L_\beta & L_p & L_r & 0 \\ N_\beta & N_p & N_r & 0 \\ 0 & 1 & 0 & 0 \end{bmatrix} \begin{bmatrix} \beta \\ p \\ r \\ \phi \end{bmatrix} + \begin{bmatrix} 0 & \frac{Y_{\delta r}}{u_0} \\ L_{\delta a} & L_{\delta r} \\ N_{\delta a} & N_{\delta r} \\ 0 & 0 \end{bmatrix} \begin{bmatrix} \delta_a \\ \delta_r \end{bmatrix} \tag{2}$$

After substituting the stability derivatives calculated at cruise in Equation 2, the state space matrices A and B were computed.

The system was found to stable after eigenvalue analysis. However, Level 1 lateral-directional flying qualities were not achieved initially. Therefore, a state feedback controller was implemented. The gain matrix K was iterated

upon until the system met Level 1 lateral-directional flying qualities. The control laws are shown below.

$$\delta_a = 1.0425\beta - 0.8238p - 0.1540r - 0.0268\phi$$

$$\delta_r = -0.0649\beta - 0.0398p + 0.1239r - 0.0065\phi$$

Table 28 shows the Level 1 requirements for lateral-directional dynamic stability [30], the open-loop system characteristics, and the closed loop system characteristics. The *Argo* satisfies these requirements. Care was taken to avoid aggressive damping of longer period modes like phugoid and dutch roll. If the damping is too aggressive on the longer period modes, passengers will experience discomfort due to sudden up-down pitching motion or yaw-roll motion.

Table 28 Lateral-Directional Dynamic Stability

	Dutch Roll ω_n	**Dutch Roll ζ**	**Dutch Roll $\zeta\omega_n$**	**Roll τ_R**	**Spiral T_2**
Level 1 Requirement	$\omega_n > 0.4$ rad/s	$0.19 < \zeta < 0.70$	$\zeta\omega_n > 0.35$ rad/s	$\tau_R < 1.4$ s	$T_2 > 20$ s
Open Loop System	1.496 rad/s	0.299	0.448 rad/s	0.447 s	14.298 s
Closed Loop System	1.323 rad/s	0.387	0.597 rad/s	0.289 s	20.122 s

IX. Structures and Loads

A. Loads

1. V-N Diagram

A V-N diagram was made in order to illustrate the flight envelope for the aircraft, making use of various velocities as well as limit loads factors. All values were calculated in terms of knots equivalent air speed (KEAS) at sea level where the aerodynamic forces on the aircraft would be the greatest using equations from Roskam Part V, Chapter 4 [6]. V_A, V_C, and V_D were calculated to be minimums of 225 kt, 301 kt, and 377 kt respectively. A safety factor of 1.5 was implemented as per 14 CFR Part 25.303 [4]. The positive and negative ultimate limit loads were calculated to be 3.75 and -1, respectively. These fall within the limits detailed in 14 CFR Part 25.337 [35]. Furthermore, the stall velocity was calculated to be 116 kt. In Figure 40, the gust lines are demoted by dashed lines. The maximum gust intensity design speed, V_B, was calculated to be 182 kt and is shown to be significantly less that than V_C. This is due to the fact that V_C has to be sufficiently greater in order to accommodate inadvertent speed increases a result of severe turbulence. Since the *Argo* is a heavy aircraft, gusts will not have a significant impact on the loads affecting the aircraft and will therefore not size the aircraft. This gust effect is much more pronounced in lighter general aviation aircraft.

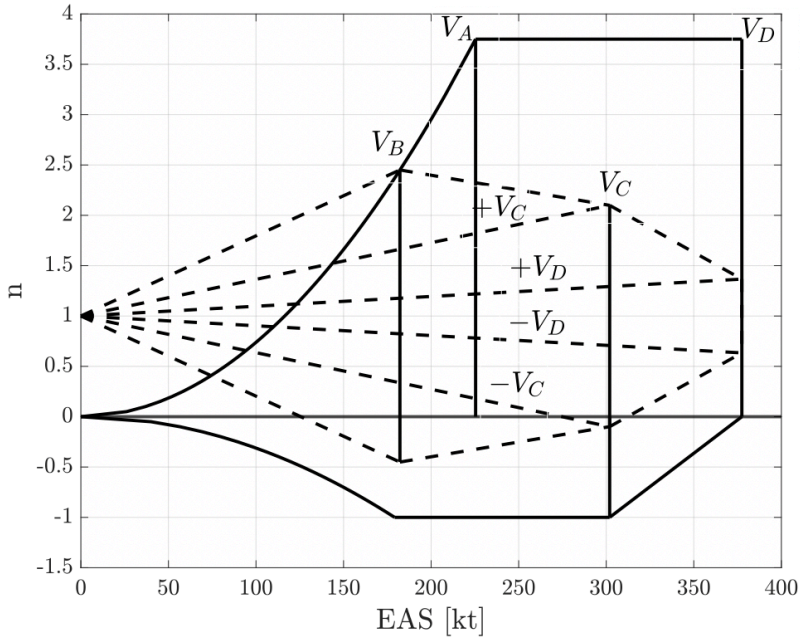

Figure 40 V-N Diagram with Incorporated Gust Loads

2. Wing Loading

The span-wise wing loading was approximated for the *Argo* by using a trapezoidal method, elliptical method, and a Schrenk's approximation. Schrenk's approximation was found averaging the wing loading from the elliptical and trapezoidal methods. It is a good method for span-wise loading estimations for a non elliptical wing [5]. The span-wise wing loading is shown in Figure 41.

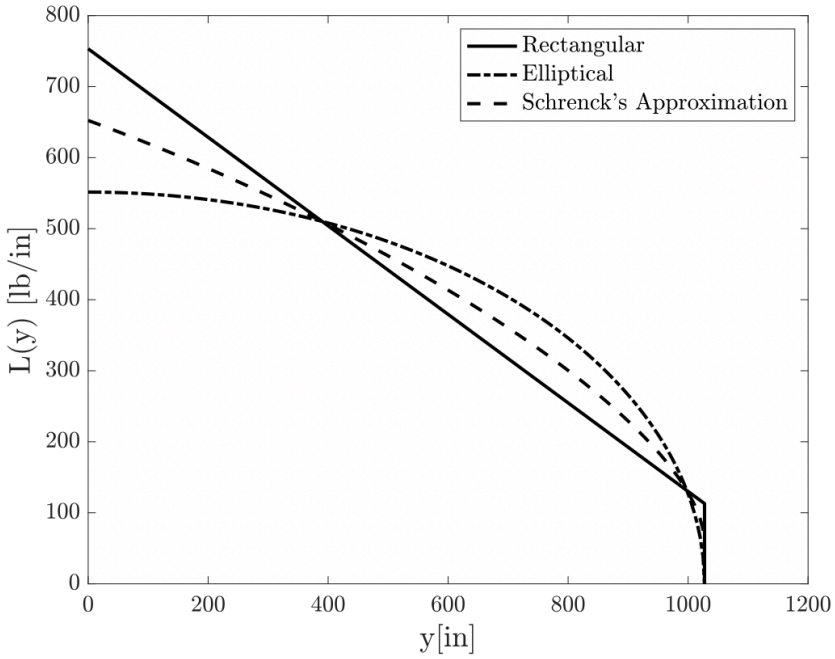

Figure 41 Span-wise Wing Loading Diagrams

3. Shear Force and Bending Moment

The span-wise shear force and bending moment are found numerically integrating the wing loading from Schrenk's approximation and shear diagrams, respectively. The ultimate shear force and bending moment occur at the the point where the wing is connected to the fuselage and are approximately -363,000 lb and 129,000,000 lb-in respectively. The shear force and bending moment diagrams are shown in Figures 42 and 43.

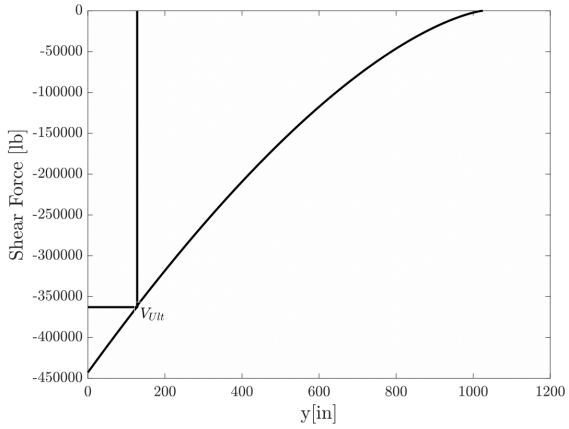

Figure 42 Span-wise Shear Force Diagram

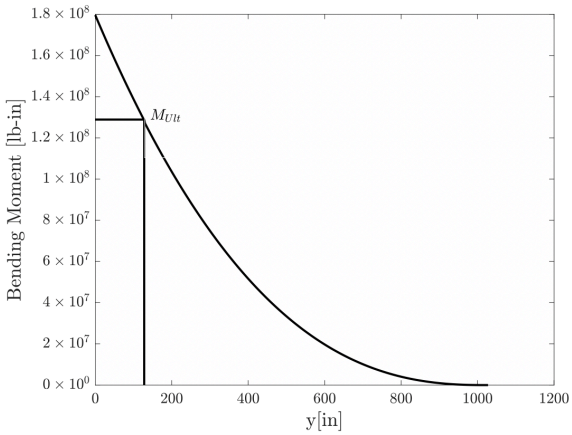

Figure 43 Span-wise Bending Moment

4. Load Cases

There are several load cases of interest on the *Argo*. These are taxi, takeoff, climb, cruise, turning, landing and descent. The highest loads will be at turning due to lift induced vertical acceleration. At cruise during steady level flight, the internal pressure within the cabin will contribute a significant load on the structure of the fuselage. During takeoff and climb, the loads will primarily be due to lift. At 8,000 ft of altitude, the cabin will start to pressurize introducing additional loads. During descent, the loads on the exterior surfaces aircraft will be minimal, and the the loads due to cabin pressurization will dissipate once the aircraft descends below 8,000 ft. Upon landing, the loads will immediately transfer to the main landing gear as the aircraft comes into contact with the ground. Once the aircraft is on the ground, internal loads are negligible and the only loads come from dynamic loads due to the movement of the aircraft.

5. Load Paths

Load path diagrams showing the aircraft at cruise and on the ground are shown at in Figures 45 and 44. The arrows represent the direction of the loads as they travel throughout the aircraft and are symmetrical about the aircraft's vertical axis.

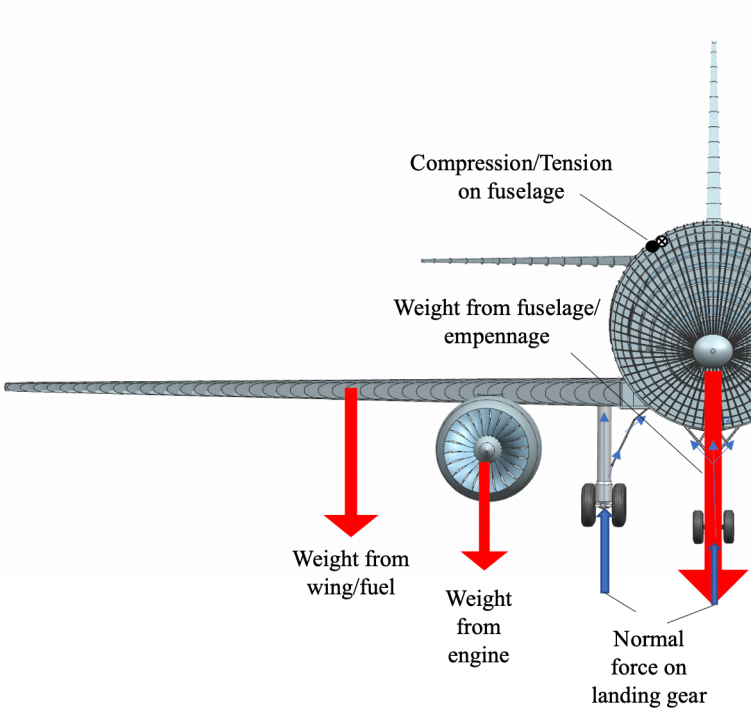

Figure 44 Load Paths for the *Argo* on the Ground

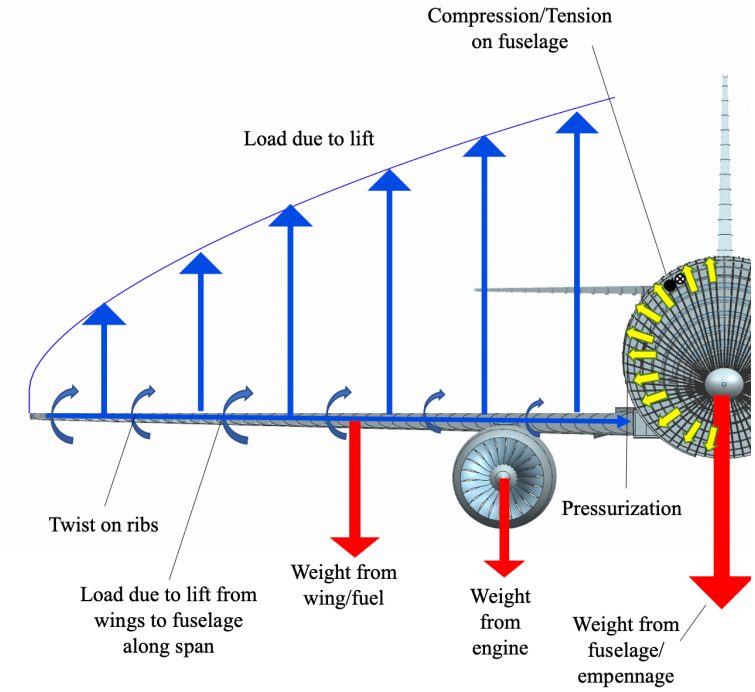

Figure 45 Load Paths for the *Argo* at Cruise

B. Material Selection

Sections IX.B.1 through IX.B.3 will cover the materials selected for various components of the *Argo* detailing the selection process as well as notable characteristics of the selected material.

1. Fuselage Material

For the fuselage, an aluminum alloy was chosen as the material due to its relatively light weight and high strength. Due to these traits, aluminum has been the material of choice in the aerospace industry. Other considerations included using a composite fuselage much like that of the Boeing 787, which makes use of a carbon fiber composite. In the case of the Boeing 787, using a composite body offered an average of 20% less weight in comparison to more traditional aluminum fuselage. A composite fuselage reduced the amount of both non-routine and scheduled maintenance, as composites eliminate metal fatigue and corrosion [36]. However, there are several drawbacks that come with composites. The first drawback is that most composites are anisotropic, including the carbon laminar composites used in the Boeing 787. The anisotropic properties cause the composite to primarily display its properties in a single direction which is not ideal for the complex loads that an aircraft will see during flight. Also, using composites would drastically increase non-recurring costs such as development, material and manufacturing costs [37]. Ultimately, Al2024-T3 was chosen as the fuselage material due to its more favorable maximum yield stress and densities when compared to other commonly used aluminium alloys, as seen as Table 29 with data gathered from MatWeb [38]. Another reason why Al2024-T3 was ultimately chosen as the fuselage material is that the fuselage cabin is prone to fatigue due

to repeated pressurization [39]. By comparison, Al7075-T6, another commonly used aluminium alloy in aircraft, is much stiffer and has a much higher tensile strength. Due to this fact, Al7075-T6 is much more commonly used in areas where there are high compression stresses such as aircraft wings and aircraft with an unpressurized fuselage.

2. Wing Material

In order to choose the wing material, a trade study was conducted. For this trade study, a wing material will be chosen primarily for its strength and secondarily its weight. Ultimately, four materials were considered: Epoxy/carbon fiber composite, Al7075-T6, Al6061-T6, and Al2024-T3 ,as shown in Table 29.

Table 29 Fuselage and Wing Material Properties [38]

Material	Average density [lb/in^3]	Max σ ultimate [psi]	Max σ yield [psi]
Epoxy/Carbon Fiber (CFRP)	0.0614	550,000	437,000
Al7075-T6	0.102	83,000	73,000
Al6061-T6	0.0975	45,000	40,000
Al2024-T3	0.100	63,800	42,100

Since the wing will undergo a lot of compression stress due to the wing bending from lift, the chosen material will need to have a high ultimate tensile stress. The density of the material will have to be comparatively low in order to minimize weight which in turn will minimize cost. Using the data collected, a decision matrix was created in which the ultimate tensile strength was weighted 0.8 and the material density was weighted 0.2. These weights were determined from the fact that while reducing weights and cost is important, ensuring that the wing does not experience material failure mid-flight is imperative. From this, the choice of material was narrowed down to CFRP and Al7075-T6. A cost analysis was then performed to select the better material. The methodology of this cost analysis is described in detail in Section XII. The result of this analysis was that using Al7075-T6 would save roughly $81 million dollars per aircraft for a 1,000 aircraft production run over using CFRP. Al7075-T6 was selected as the wing material because the the performance benefits and weight savings of CFRP could not outweigh the $81 million dollar cost savings. Additionally, the skin of the leading edge will be further reinforced with aluminum. For this aluminum was chosen over composites, because aluminum has more favorable heating properties than composites that will allow it to run an anti-icing system through the leading edge. Additionally, aluminum and other metals will absorb the impact better than composites will in the event of a foreign object strike as the leading edge has the highest probability of such strikes [40].

3. Landing Gear Material

Recently aircraft manufacturers have opted for landing gear struts made out of a high strength steel and titanium alloy hybrid [41]. While these materials are heavier and more expensive than more common aerospace materials, they are commonly used due to the need for the landing gear to withstand heavy MTOWs and high impact landing loads.

Therefore, materials with high yield strengths are needed. Properties for the commonly used materials in landing gear are shown below in Table 30. Following industry trends, the *Argo*'s landing gear will be made from a steel and titanium alloy hybrid using Steel 4340 and Ti-6Al-4V. Further details on the landing gear will be provided in more depth in Section IX.E.

Table 30 Landing Gear Materials [38]

Material	Density [lb/in^3]	Yield strength [psi]	Poisson's ratio	Young's modulus [ksi]
Steel 4340	0.284	68,200	0.29	27,800
Ti-6Al-4V	0.160	120,000	0.33	16,500

C. Structural Arrangement

Figure 46 shows the complete structure of the aircraft. All structural component models shown in Figures 46 - 57 were made using NX 12.

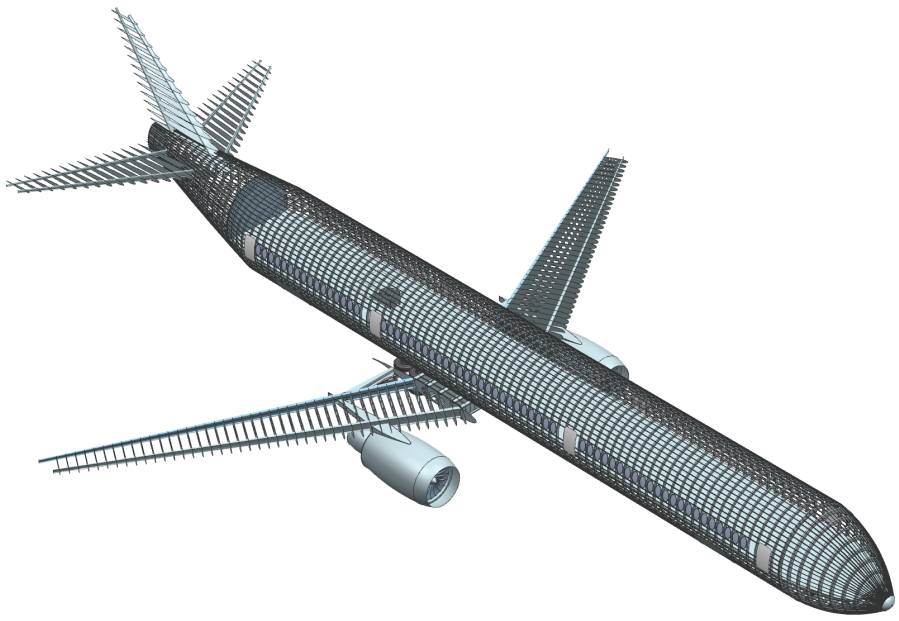

Figure 46 The *Argo's* Structural Layout

1. Fuselage Structure

The fuselage structure is composed of three major elements: the frames, stringers, and the skin. The calculated minimum skin thickness is 0.2 in assuming a fatigue allowable tension stress of 14,000 psi. This value falls directly in the middle of the range of values suggested by Niu [39] and was chosen in order to gain a proper balance between skin thickness and number of flights per design life of the airframe. In order to determine the shape of stringers a trade study

was conducted. The criteria for this trade study were that the stringer shape has to be structurally efficient and resistant to corrosion in hard to inspect areas. The stringer shapes considered are shown below in Figure 47.

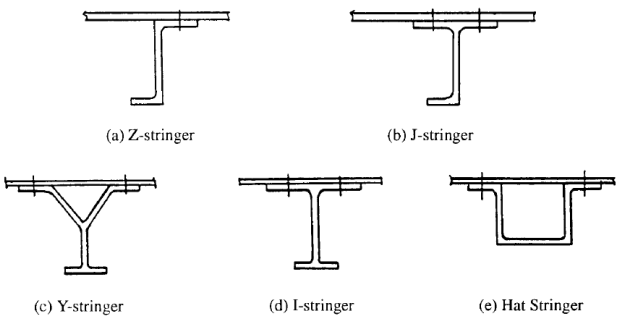

Figure 47 Typical Skin-stringer Panels adapted from Niu[39]

Table 31 Stringer Characteristics Adapted from Niu [39]

Type	Structural efficiency	Corrosion inspection difficulty
Z-Stringer	High	Negligible
J-Stringer	Medium to high	Negligible
Y-Stringer	Highest	Significant
I-Stringer	Medium to high	Negligible
Hat Stringer	Medium to high	Signficant

The Y- and hat-stringers are not viable options due to their corrosion inspection difficulty. The I-stringer is known to have difficulty attaching to structure. Ultimately, a Z-stringer was chosen in due its higher structural efficiency than that of a J-stringer. The frame depth and spacing as well as stringer spacing are based on values calculated by using methods described in Roskam Part III [42]. The values are shown below in Table 32.

Table 32 Fuselage Frame Values

Component	Value [in]
Frame depth	6.12
Frame spacing	20
Stringer spacing	12

Pressure bulkheads are an integral part of the fuselage structure as they seal in the cabin and flight deck from the rest of the aircraft. They help maintain the cabin pressure once the aircraft flies above 8,000 ft. There are three possible configurations for bulkheads: flat, hemispherical, and semispherical [39]. The flat and hemispherical configurations are shown in Figure 48. The flat configuration provides more usable space when placed in the forward radome and is used when a passageway in the aft bulkhead is a necessity. The drawbacks to a flat bulkhead are that they

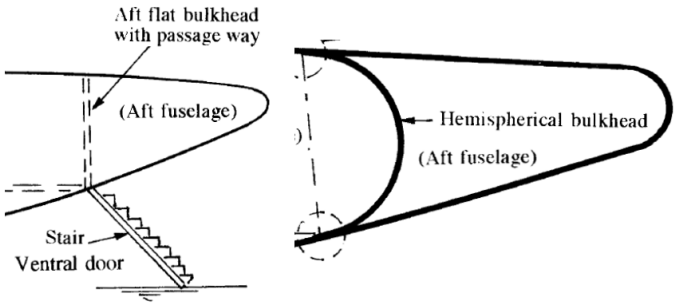

Figure 48 Flat and Hemispherical Aft Bulkhead Configurations Adapted from Niu [39]

are structurally inefficient and are often times heavier than other types of bulkheads. Hemispherical bulkheads are more structurally sound and support pressure loading by converting it to membrane stress. The immediate drawback of the hemispherical bulkhead is that it is extremely difficult and costly to properly manufacture. Due to this a semi-spherical bulkhead was chosen. Like the hemispherical bulkhead, it supports pressure loading by converting it to membrane stress. Additionally, a bulkhead ring is required in order to fasten the bulkhead to the fuselage and resist compression loading and a keel beam will be added in order to help transfer loads from the wingbox to the fuselage. A model of the fuselage structure is shown in Figure 49.

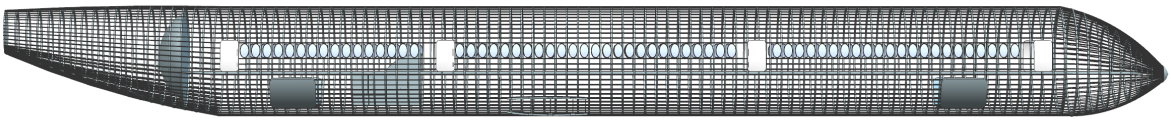

Figure 49 The *Argo's* Fuselage Structure

2. Wing Structure

The wing structure consists of ribs, spars, and stringers. For the purposes of preliminary design, stringers were not taken into consideration in the structure. The front and rear spars are located at 15% and 60% of the chord respectively. This leaves room for anti-icing systems located in the leading edge and room for high lift systems at the trailing edge. An I-beam was chosen due to its superior geometry; the caps of the I beam resist bending stress while the web resists shear stress. The spars were sized using methods found in Megson [43]. The ribs are placed perpendicular to the front spar rather than perpendicular to the flight path for easier installation and buckling analysis. By comparison, having the ribs parallel to the flight path will be easier to mount to the fuselage but may be heavier overall [39]. The thickness and spacing of the ribs were determined by the methods introduced by Roskam [42]. The values for the wing box structure are shown below in Table 33.

Table 33 Wing Structure Values

Component [units]	Value [in]
Spar cap cross section [in^2]	31
Web thickness [in]	0.25
Rib thickness [in]	0.23
Rib spacing [in]	24.00

The wing torque box will be a wet wing, containing all of the fuel the necessary inside of it. This will help with the loads acting on the wing as the weight of the fuel will help offset the upward bending of the wings due to lift. For this reason, the wing ribs are equipped with holes that allow fuel to freely flow from the fuel tanks to the engines. The fuel system will be explained in more detailed in Section XI.C. Furthermore, the wing structure will connect to the fuselage via a wingbox fairing located underneath the fuselage. This fairing will also house the landing gear once it is retracted. The wingbox structure will consist of a series spar-like support structures made out of titanium. This was based on a similar analysis done on a Boeing 777-X [44]. This attachment point where the wing is bolted to the fuselage is also where the aircraft experiences the largest bending moment and shear force. Additionally, a third spar was added onto the wing structure. This spar will serve as the attachment point for the main landing gear. A model of the wing torque box structure is shown in Figure 50.

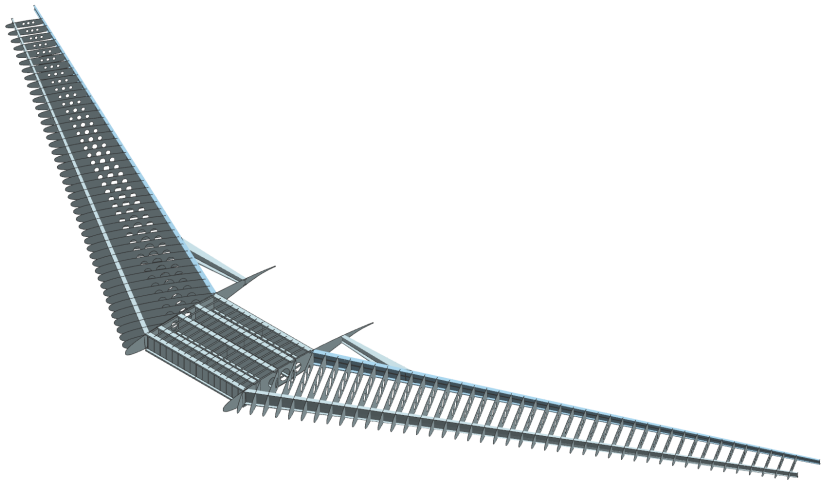

Figure 50 The *Argo's* Wing Structure

3. Structural Analysis

Structural analysis was done on the wing in order further analyze the structural capabilities of the *Argo's* wing. Two analyses were done; using the Euler-Bernoulli theory and using finite element analysis. For the Euler-Bernoulli, the wing structure was idealized as a cantilever I beam spar. The tip deflection in this analysis was equal to 4.22 ft. For the

finite element analysis, a NASTRAN software was used and the tip deflection is equal to 3.38 ft. Figures 51 and 52 show representations of the two analyses.

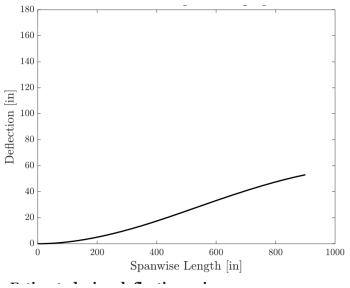

Figure 51 Euler-Bernoulli Analysis for Wing Deflection

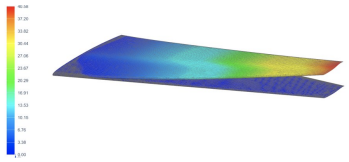

Figure 52 Finite Element Analysis for Wing Deflection

4. Empennage Structure

The vertical and horizontal tails were constructed in a similar manner to that of the wing structure. The front and rear spars are located at 15% and 60% of the chord respectively in order to leave sufficient space for elevators and a rudder. The vertical and horizontal tails will be mounted onto the tail cone and will help provide stability and control as previously discussed in Section VIII. A model of the empennage structure is shown in Figure 53.

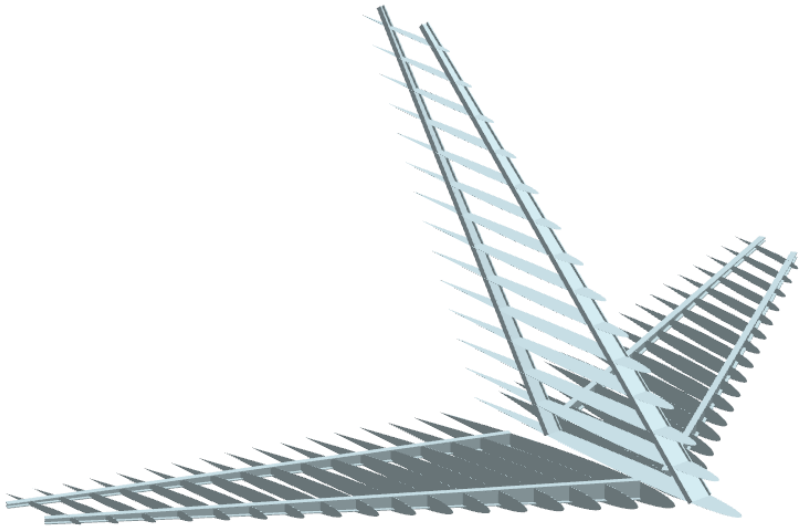

Figure 53 The *Argo's* Empennage Structure

D. Pressurization

The *Argo's* cabin will be designed for 8,000 ft altitude pressure which corresponds to 10.92 psi as specified the RFP [1]. This will be done with bleed air from the engines. At cruise, this corresponds to a ΔP of 7.92 psi. The constant cabin pressure will be bounded by the forward and aft bulkheads described in Section 49 as well as the floor

and ceiling of the cabin. The exception to this case is the lavatories located below the main deck as shown in Figure 49. To accommodate this, the cabin pressurization will extend to this lower area.

E. Landing Gear

The landing gear of the *Argo* will be retractable with the nose gear retracting into the nose cone and the main gear retracting into the body of the aircraft. The aircraft structure with the retracted landing gear is shown in Figures 55 - 57.

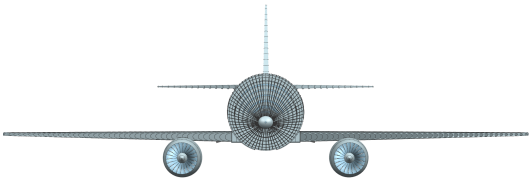

Figure 54 Front View of the *Argo* with Landing Gear Down

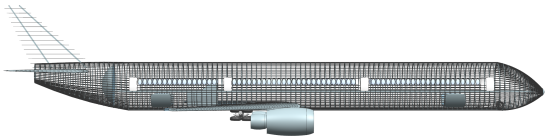

Figure 55 Side View of the *Argo* with Landing Gear Up

Figure 56 Models of Landing Gear

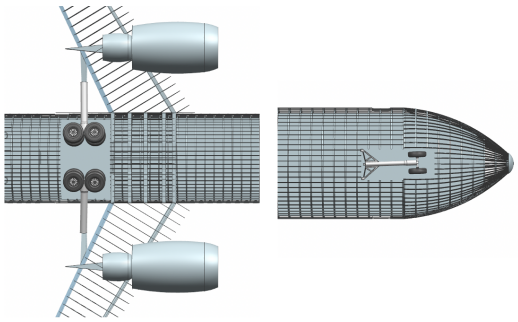

Figure 57 View of the *Argo's* Stowed Landing Gear

1. Landing Gear configuration

A trade study was conducted in order to determine the landing gear configuration that best suits the *Argo*. The criteria for this trade study is that the visibility over the nose must be sufficient in order to give pilots a good field of vision, floor attitude on the ground must be level in order to simplify passenger boarding and cargo loading, steering must be sufficiently good in order for the aircraft safely taxi at airports, and the groundloop behavior must be stable so that the aircraft does not tip over during ground maneuvers. Three landing gear configurations were considered: tricycle, bicycle, and tailwheel. Data was collected and is presented in Table 34.

Table 34 Landing Gear Configuration Characteristics Adapted from Roskam Part IV [45]

Characteristic	Tricycle	Bicycle	Tailwheel
Visibility over nose	Good	Good	Poor
Floor attitude	Level	It depends	Not level
Steering while taxiing	Good	Good	Poor
Steering after touchdown	Good	Marginal to good	Poor
Groundloop behavior	Stable	Depends on cg location	Unstable

Based on the data collected, a tricycle configuration is best suited for the *Argo*. In addition to the characteristics mentioned in Table 34, a tricycle configurations also provides good takeoff rotation and an easy takeoff procedure.

2. Landing Gear Sizing

The landing gear locations were determined using methodology detailed in Roskam Part IV [45]. Notable landing gear data are shown below in Table 35.

Table 35 Landing Gear Characteristics

Characteristic	Value
Nose gear distance from nose [ft]	28
Main landing gear distance from nose [ft]	130.3
Main landing gear height [ft]	12.5
Main landing gear track [ft]	26.7
Tail strike angle [°]	15.7

The landing gear configuration and locations on the *Argo* were compared to historical industry standards and found to be in line as shown in Table 36. For the *Argo*, a double bogey configuration was chosen for the main landing gear instead of a triple bogey configuration. This was because while there was no significant weight savings using either configuration, using a double bogey configuration saved several counts of drag when the gear was extended.

Table 36 Landing Gear Configuration and Location Data

Plane	Nose gear configuration	% of Fuselage length from nose	Main gear configuration	% of Fuselage length from nose
Boeing 777-9 [46]	1xSingle bogey	7.84	2xTriple bogey	50.82
Boeing 787-10 [47]	1xSingle bogey	8.02	2xDouble bogey	50.81
Boeing 777-300ER [48]	1xSingle bogey	8.06	2xTriple bogey	50.79
Airbus A340-500 [49]	1xSingle bogey	9.77	3xDouble bogey	50.73
Airbus A330-200 [50]	1xSingle bogey	11.30	2xDouble bogey	48.90
Airbus A350-1000 [51]	1xSingle bogey	6.29	2xTriple bogey	50.43
Argo	1xSingle bogey	13.01	2xDouble bogey	55.19

In this configuration, the nose gear supports 8% of MTOW which is the ideal amount necessary in order to properly steer the aircraft [5]. In addition, this landing gear configuration uses a conservative estimate and assumes 100% of the landing weight is applied to the main landing gear upon landing.

3. Tires

The tires for the landing gear are sized by the maximum static load per tire using anti-skid brakes on dry concrete. The maximum static load per tire is multiplied by a safety factor of 1.07 as per 14 CFR Part 25.733 [52] as well as an aircraft growth factor of 1.25. With these factors in place, the main landing gear and the nose landing gear will have a maximum static load of 74,700 lb and 19,700 lb respectively. Additionally, the maximum tire operating speed of the *Argo* was calculated to be 185 mph. The tires used for the landing gear are shown in Table 37. The tires chosen meet both maximum tire operating speeds and maximum tire static loads required for the *Argo*.

Table 37 Landing Gear Tire Data Adapted from Goodyear Tires [53]

Location	Type	Size	Ply rating	Rated max static load [lb]	Speed rating [mph]
Nose	VII	40x12	18	21,000	210
Main	VII	56x16	38	76,000	217

4. Shock Absorbers and Brakes

Shock absorbers are a critical component of the aircraft that helps absorb the kinetic energy associated with landing and taxiing loads. The *Argo* will use oleo-pneumatic struts since it is the most common type of shock absorbers found in jet transports and have the highest energy absorption efficiency [45]. The minimum shock absorber height and diameter are calculated using methodology detailed in Roskam Part IV [45]. The minimum shock absorber height based on the shock absorber stroke was calculated to be 16.6 in and 27.2 in for the main and nose gear respectively. The absolute minimum diameter of the struts are 14.9 in and 5.6 in for the main and nose gear respectively. The brakes used for the landing gear will be anti-skid carbon brakes as they have a deceleration factor of 0.5g [45].

X. Mass Properties

A. Weight Build-up

A bottom-up approach was used to estimate the MTOW of the *Argo*. The masses of individual components are listed in Table 38. Individual component weights were estimated by averaging values obtained using mass equations for transport aircraft listed in Raymer and the Torenbeek method introduced by Roskam [5][6]. Manufacturer specified component weights were used over these estimates when available. Averages were not used when there was a significant discrepancy between the values computed by Raymer and Roskam. For instance, Roskam's estimate for instruments,

Table 38 Comparison of Component Weights

Parameter [lb]	Raymer [5]	Roskam [6]	*Argo* Weights	Methodology
Wing Group	55,900	64,900	60,400	Average
Empennage Group	10,400	9,610	10,000	Average
Fuselage Group	48,000	61,700	54,900,	Average
Nacelle Group	23,200	15,000	19,100	Average
Nose Landing Gear	2,740	1,050	1,900	Average
Main Landing Gear	20,400	10,200	15,300	Average
Total Structural Weight	161,000	162,000	**162,000**	-
Engine(s)	-	-	33,300	Actual Weight
Engine Controls	226	-	226	Raymer
Fuel System	169	-	169	Raymer
Total Power Plant Weight	-	-	**33,700**	-
Avionics + Instruments + Electronics	1,800	4,090	4,090	Roskam
APU	1,540	-	1,800	2.2x Uninstalled Weight [5]
Pneumatic Systems	355	4,910	4,910	Roskam
Flight Controls	2,230	3,760	3,000	Average
Furnishings	12,500	65,400	39,000	Average
Air-Conditioning System	4,780	7,090	5,940	Average
Handling Gear	135	225	180	Average
Fixed Equipment Weight	23,300	86,300	**58,900**	-
Empty Weight	-	-	**255,000**	-
Fuel Capacity	-	-	151,000	Performance
Payload	-	-	94,300	RFP
Flight Design Gross Weight	-	-	**500,000**	-

avionics and electronics was used without considering the Raymer value. This is because the Raymer prediction was significantly below the industry norm [6]. A similar reasoning was used to reject Raymer's estimate for pneumatic systems. Components were grouped by structural weight, powerplant weight, and fixed equipment weight. The *Argo*'s EW was computed as 255,000 lb and MTOW was 500,000 lb.

B. Center of gravity estimate

To estimate the center of gravity of the aircraft, the component weights were multiplied by their respective moment arms and divided by the sum of the individual weights. Guidelines from Roskam [6] were used to estimate the location of components in NX 12. In this calculation, only components whose center of gravity could be reasonably estimated were accounted for. Systems which were distributed throughout the cabin, such as electrical and pneumatic

systems, were not included. Moment arms were measured by taking the lateral distance from the tip of the aircraft nose to each component's center of gravity. The longitudinal distance was measured from the nadir of the fuselage. The CG and component moment arms at empty weight can be found in Table 39. This table also serves as a legend for Figures 58 and 59. Figure 58 shows the side view of the *Argo* with component CG locations in black boxes and the aircraft CG location at empty weight marked with a blue cross. A top view with the same information is shown in Figure 59.

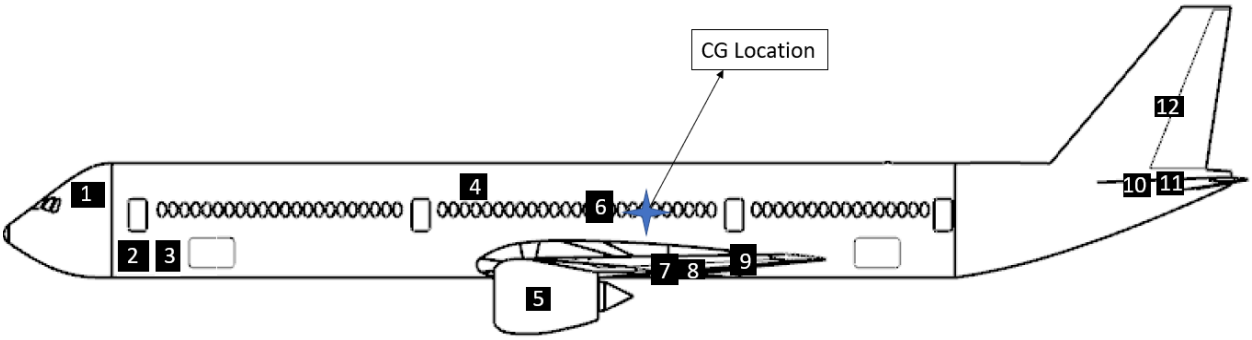

Figure 58 Component and Aircraft CG Locations - Side View

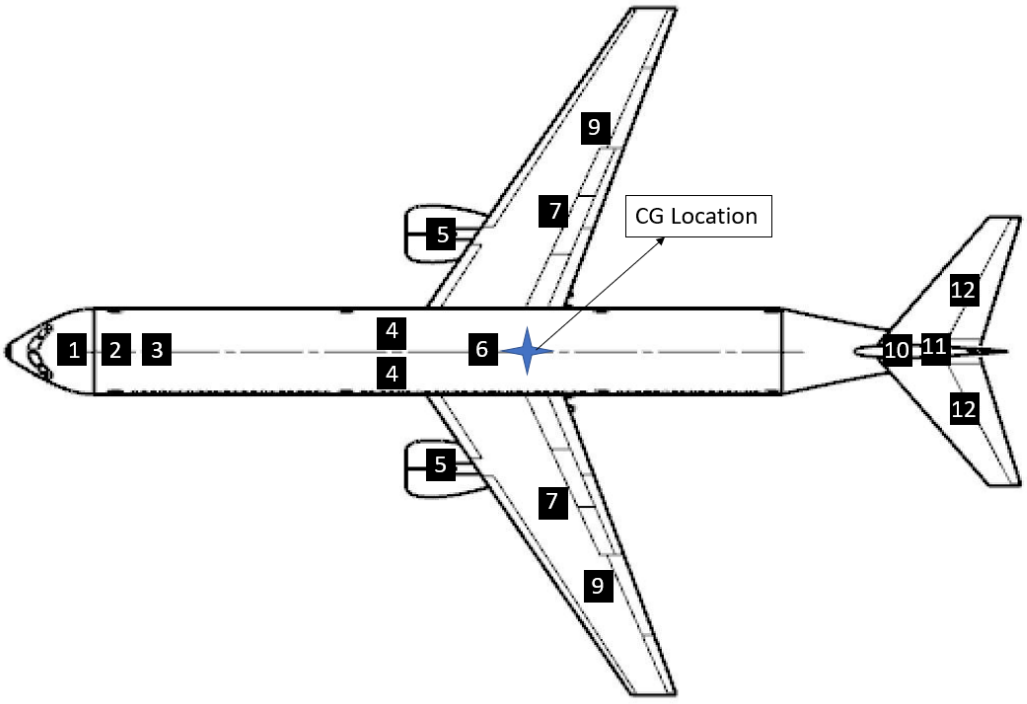

Figure 59 Component and Aircraft CG Locations - Top View

Table 39 Component CG Locations

Label Number	Description	X-Location [ft]	Y-Location [ft]
1	Instruments	15.5	15.0
2	Electronics	28.3	2.56
3	Nose Landing Gear	30	2.56
4	Air-Conditioning	96.7	17.8
5	Engine(s)	102.5	-5.21
6	Fuselage	114	12.1
7	Wing	128	4.74
8	Main Landing Gear	128	2.80
9	Fuel System	141	4.84
10	APU	213	16.5
11	Horizontal Tail	229	16.6
12	Vertical Tail	229	31.7
13	**Empty Weight Center of Gravity of Aircraft**	**117 (6.64 %MAC)**	**8.14**

C. CG Travel with Fore and Aft Loading

To show the CG shift in flight, data from Section VII.G was used to characterize the fuel burn during each mission segment. The CG was then calculated during each mission segment to show how the CG changes with fuel weight. The CG of the aircraft can also be affected by the movement of passengers on a flight. As passengers stand up and move about the cabin, the CG is affected. Passengers may get up to stretch their legs, use the lavatory, or speak to the flight attendants. Extreme forward loading was simulated by assuming four passengers from each of the last two rows moved to the forward-most galley of the aircraft. Extreme aft loading was simulated by assuming four passengers from each of the first two economy rows were using the lower-deck lavatories. In both cases, the aircraft was at full capacity to compare the CG to a neutral case where each passenger was sitting in his or her assigned seat. CG travel for the aft case, forward case, and the neutral case are shown in Figure 60, and the CG at different mission segments are shown through the dotted lines in the same plot. CG is found to vary from 3.6% MAC to 39.8% MAC from the most forward case to the most aft case. The aft shift in CG due to fuel loading can be explained by the fuel being stored entirely in the wings as detailed in Section XI.C.

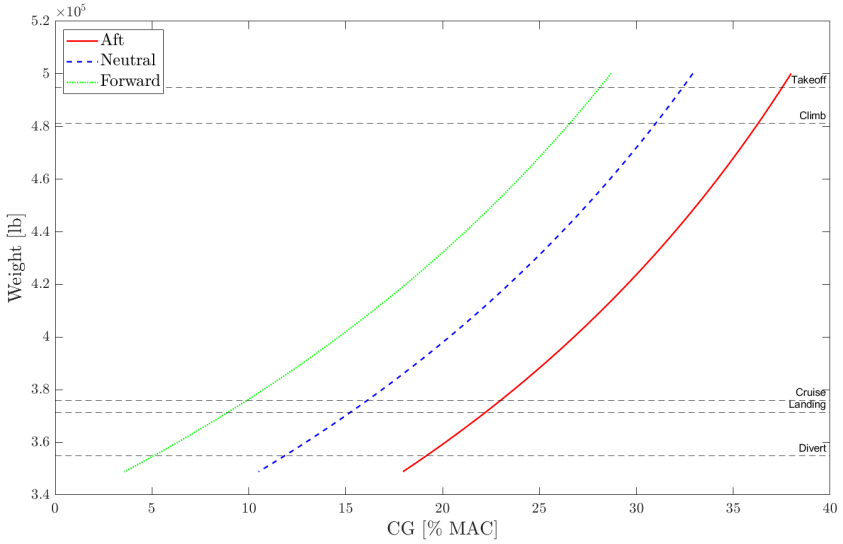

Figure 60 CG Travel for Aft, Forward and Neutral cases

D. Passenger Loading

Figure 60 shows the shift in CG in flight when *Argo* is at full capacity. However, there is a significant shift in CG as passengers board the aircraft, so further analysis was carried out to determine the resulting CG shift. To account for both forward and rear loading extremes, passengers were loaded exclusively from front to back and back to front at ZFW. For both loading scenarios, window seats were filled first, followed by aisle seats and finally center seats until all seats were filled. A 5% safety margin was used at the most forward and aft points to account for unusual loading scenarios. Figure 61 shows the ZFW CG envelope as passengers are loaded. The forward and aft limits of CG due to passenger loading were found to be 1.28% MAC and 19.5% MAC respectively.

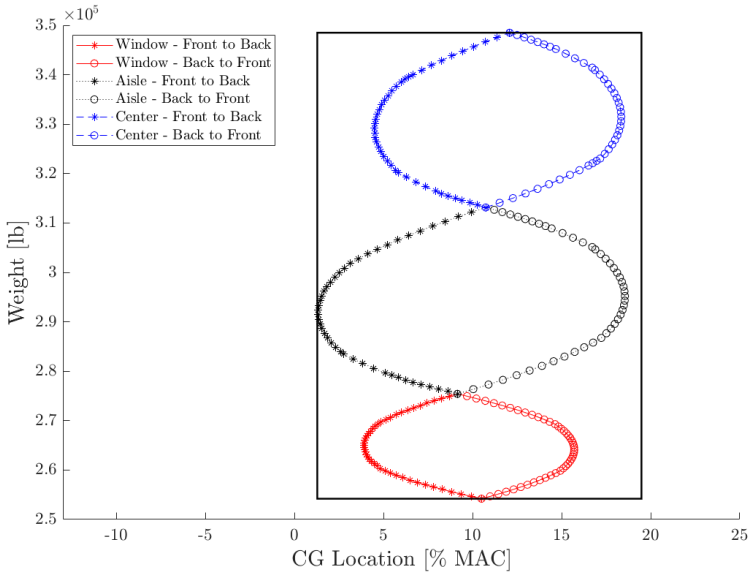

Figure 61 ZFW CG Envelope During Passenger Loading

E. Flight CG Envelope

The goal of the flight CG envelope is to provide a comprehensive picture of the CG location encompassing various loading scenarios on the aircraft. The outer bounds of Figures 60 and 61 formed the basis of the flight envelope seen in Figure 62. Forward and aft CG limits are obtained from the CG envelope. The forward and aft limits correspond with the most forward and aft cases due to passenger and fuel loading which are 1.28% MAC and 39.8% MAC respectively. These limits were used in sizing the horizontal stabilizer to obtain a balanced design. This process is detailed in Section VIII.

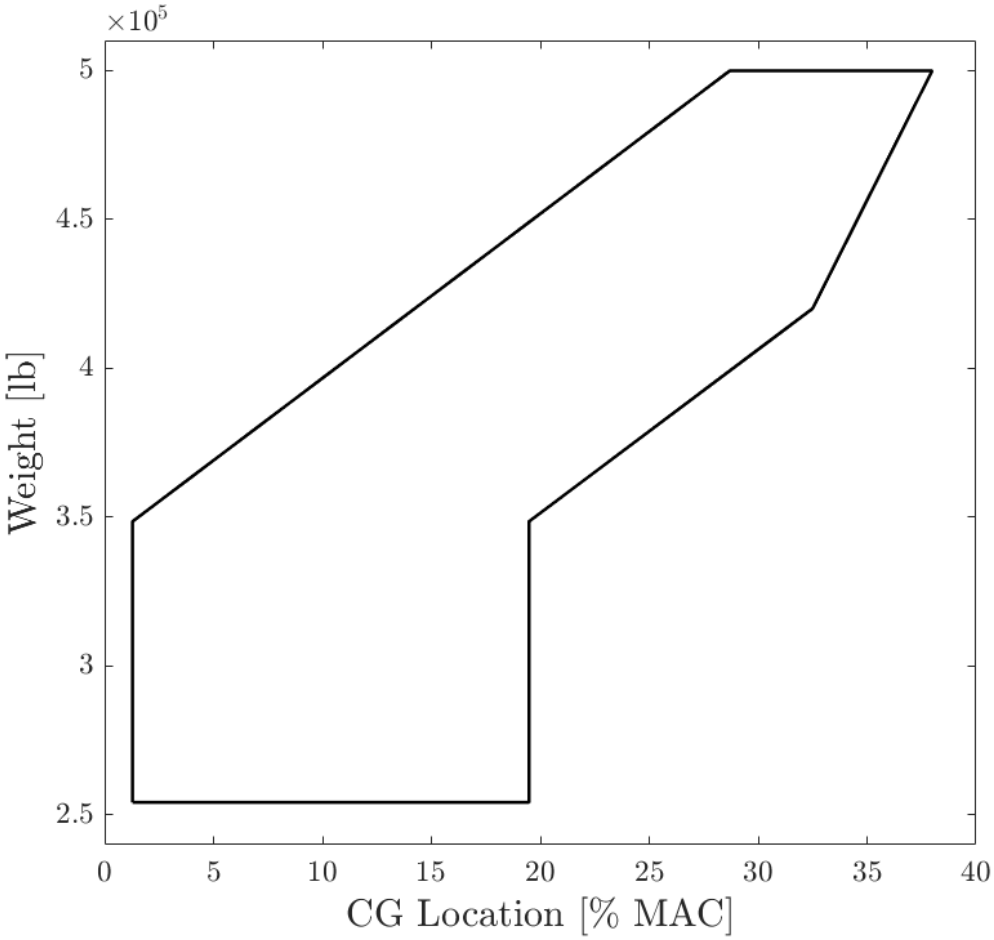

Figure 62 Flight CG Envelope

F. Main Landing Gear Effect on CG

Main landing gear placement has a significant effect on CG since it is a major structural component of the aircraft. It can affect the stability of the aircraft on the ground. In other words, moving the landing gear forward shifts the CG forward, increasing the static margin of the aircraft. However, this negatively affects the stability and controllability of the aircraft on the ground. Moving the landing gear aft has the opposite effect. As long as the CG of the landing gear lies behind the CG of the aircraft, the aircraft will not tip over. The main landing gear CG location was plotted against CG location of the aircraft in Figure 63 to quantitatively determine whether the potential benefits of shifting the gear forward would overshadow the loss in ground stability. Based on the trade study, it can be concluded that there is some room to shift the landing gear forward without affecting stability. The CG of the aircraft still lies in front of the wing for all points on Figure 63.

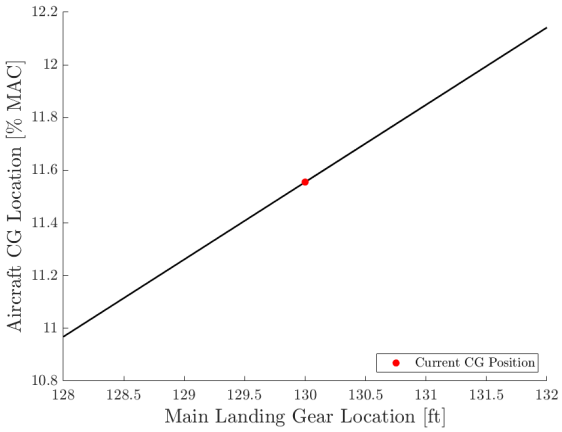

Figure 63 Plot Showing Effect of Main Landing Gear Placement on CG of aircraft

XI. Auxiliary Systems

The primary systems aboard the *Argo* are flight controls, fuel, hydraulics, electrical, pneumatics, environmental controls, emergency systems, water and waste, and a comprehensive suite of avionics. All of these systems integrate together without interference to provide a safe, reliable flight experience for both crew and passengers.

A. Flight Controls & Hydraulics System

Primary flight control systems include ailerons, spoilers, elevators, and a rudder. Secondary flight control systems manage trim surfaces and high lift systems. These are discussed in more detail in Section VI.C.

These flight control systems, while mechanically are powered by hydraulics, utilize a fly-by-wire system powered by electrically signaled actuators. The pilot's movements on a yoke with a central column drive the aircraft's attitude control in both pitch and roll. These movements send electrical signals to the hydraulic pumps which actuate the control surfaces.

Traditional cable-and-pulley flight control systems were considered. However, a fly-by-wire system was selected due to the weight savings and improved handling capabilities [54]. These advantages contribute to a more comfortable and stable passenger experience. A yoke was chosen over a joystick for the *Argo* since it is preferred by a majority of pilots [55]. Most pilots agree that the yoke enhances the feeling of control, despite being bulkier. Further, because the *Argo* is designed for short-haul missions, having less room in the flight deck as a result of the yoke is a non-issue.

Hydraulic systems are utilized aboard the *Argo* for actuating the aircraft control surfaces, as well as for extending and retracting the landing gear. Hydraulics are also used for nose landing gear steering, as detailed by Figure 64. The hydraulic system is composed of three independent hydraulic reservoirs to account for increased safety resulting from redundant systems. The system also uses a network of hydraulic pumps, accumulators, and a system of valves and

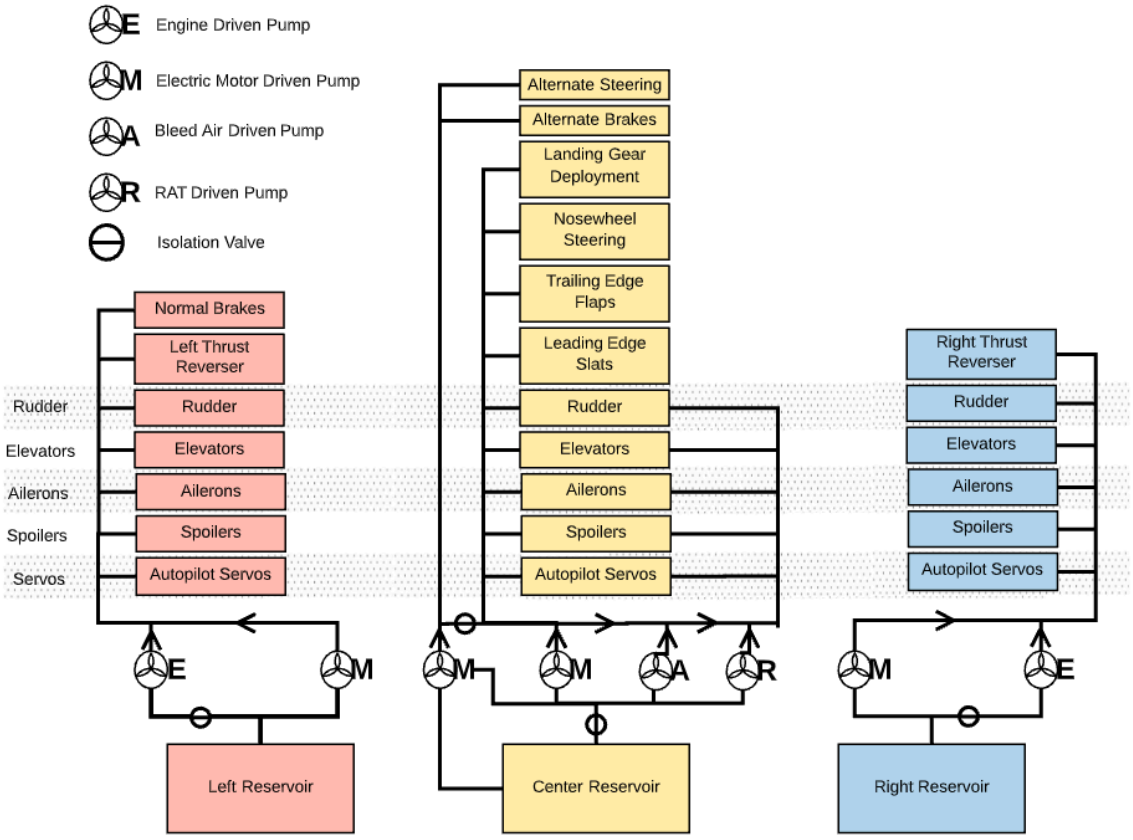

Figure 64 Flight Controls and Hydraulic System Schematic

lines. To further improve the safety of the hydraulic system, the pumps are powered by different sources. The left and right reservoirs are powered by engine driven pumps, while the center tank utilizes electric power from the APU. In the event that one of these systems fails, backups are in place, and the pumps can be driven by the RAT, bleed air, or by the APU.

As the *Argo* is designed to be a commercial use vehicle, it will make use of a phosphate ester hydraulic fluid, Skydrol 5 [5]. The system will be pressurized to 3,000 psi in order to both reduce the weight that a larger pump would necessitate [54] and to adhere to industry standards.

B. Engine Controls

The engine control system on the *Argo* features a Full Authority Digital Electronic Control (FADEC), which is comprised of the engine control unit (ECU) and fuel management unit (FMU). The engines are started by the APU. The FADEC is responsible for providing the optimal engine efficiency for the aircraft's current flight condition. Figure 65 demonstrates how variables from air data and engine sensors initiate the closed loop feedback system. By analyzing

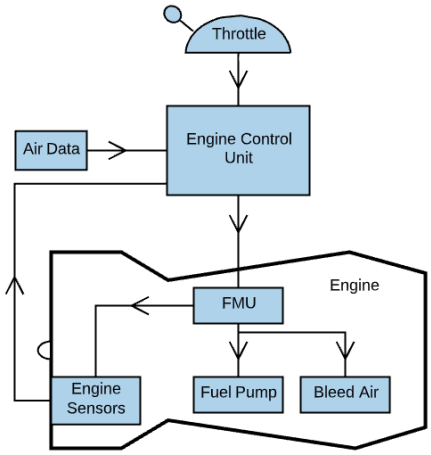

Figure 65 Engine Control System Schematic

variables, including air density, throttle position, engine temperature, and engine pressure via a system of probes and instruments, the ECU computes the proper engine operating parameters [56]. The FMU is a mechanical device mounted on the engine that directs and restricts fuel flow and bleed air. It receives digital information from the ECU and interacts with it to send signals to the fuel pumps which keep the engine running efficiently. The FMU, along with engine sensors, then send data about engine rotation speed and temperature back to the ECU. Bleed air from the engine is utilized for pneumatics. This cyclical system operates at a rate of 70 times per second. The major benefits of this fully digital system include engine health monitoring, engine restart in flight, better systems integration with the engine and other aircraft systems, and heightened safety as a result of system redundancies.

C. Fuel System

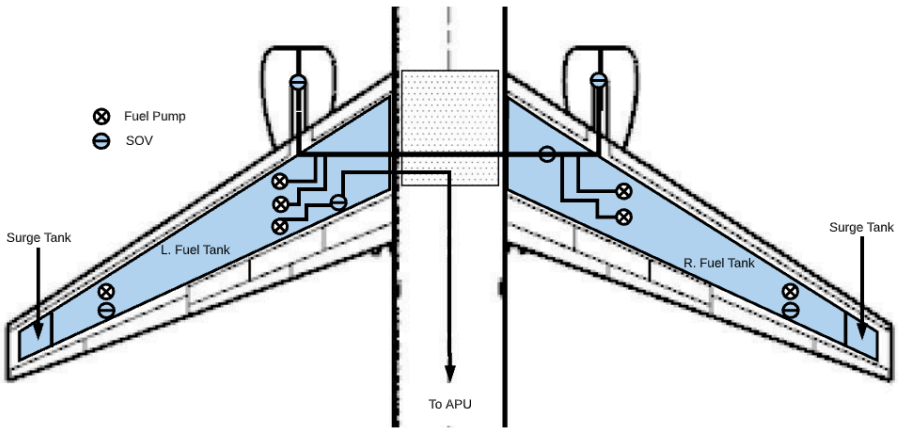

Figure 66 Fuel System Configuration

The fuel system for the *Argo* is located solely in the wings, with each wing containing one fuel tank, as depicted in Figure 66. Because the design mission for the aircraft is only 3,500 nmi, the required fuel volume is less than the volume of the wing. The fuel that the *Argo* will run on is the industry standard Jet-A, as specified by the RFP [1]. The volume of the fuel tank is 5% greater than required fuel quantity, and is displayed in Table 40. The fuel tank is designed so that it sits between the front and rear spar of the wing. This ensures that it does not interfere with flight control systems. The fuel tanks are constantly maintained at equal volumes via a fuel transfer line, as seen in Figure 66. In the event of a pump failure, backup pumps connect the fuel transfer line from each fuel tank. Additional pumps offer the option to jettison fuel from each tank as necessary. The left fuel tank has an additional pump that enables fuel to be delivered to the APU. Customers will have the option to add an auxiliary fuel tank to the system to extend the range of the *Argo*. This is detailed further in Section XII.C.

Table 40 Fuel Tank Sizing

Fuel Quantity [lb]	Volume [ft^3]	Volume [gallons]
158,655	3,148	23,538

D. Electrical System

The electrical systems aboard the *Argo* provide electrical power to internal and external lighting, food and beverage heating, backup systems, and avionics. The aircraft is equipped with a 28 V DC electrical system with two three-phase 115 V AC generators. These systems ensure battery capacity that can provide power for up to 30 minutes following primary power loss [54]. This system, which is typical of other wide body aircraft, includes two batteries, ammeters, circuit breakers, backup converters, alternators, and all of the associated electrical wiring.

Figure 67 details how the electrical load is handled. Electrical power is primarily driven by engine integrated drive generators (IDGs), however, it can be backed up in case of an emergency by the RAT. The primary power panels are connected to both engines and distribute and protect electrical loads generated from the IDGs. The power is then routed through the power management panels and delivered to the main data buses, which deliver power to the necessary systems. There are also backup converters onboard the *Argo* which are engine driven but independent of the IDGs. They enable the aircraft to operate OEI for up to 180 minutes, which is a mandatory airworthiness requirement for ETOPS flights [54].

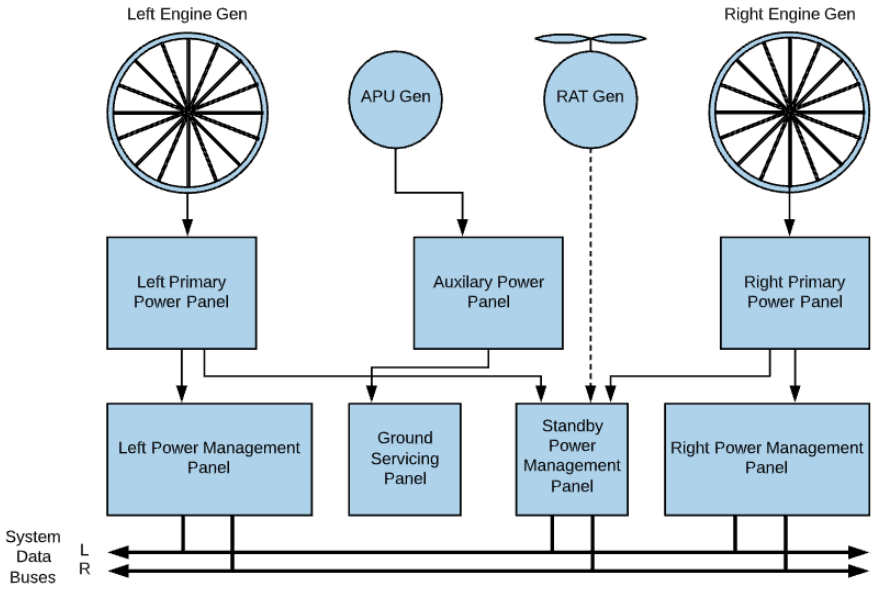

Figure 67 Electrical System Configuration

One important electrical consideration to note is that the *Argo* does not have seatback monitors for in-flight entertainment (IFE). Because the *Argo* is a short-range aircraft, adding in the additional weight for IFE could not be justified. By choosing to not have monitors on the back of every seat, IFE maintenance, costs related to IFE electrical power, and significant weight are eliminated due to the lack of monitors and associated wiring. Therefore, the choice to not include IFE results in cost reductions on both a production and operating basis. However, there are still entertainment options in place for passengers. In-flight WiFi will be made available by means of a wireless connectivity suite, and is accounted for in Section XI.H, which enables consumers to access the internet while aboard the *Argo*. The bump on the fuselage caused by the satellite connectivity device can be seen in Figure 68.

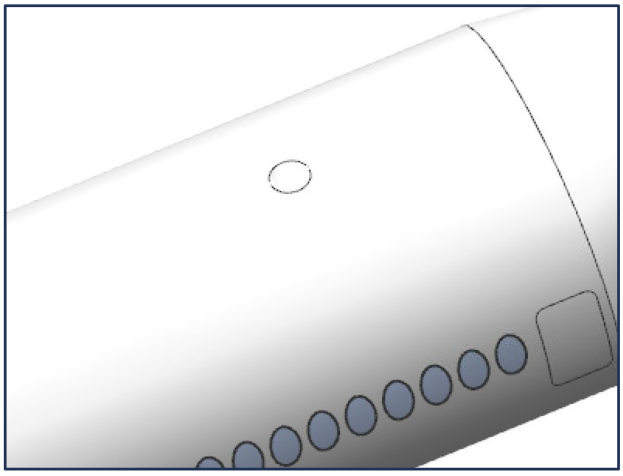

Figure 68 Internet Bump on the Fuselage

E. Pneumatic, De-Icing, and Environmental Control Systems

The role of the pneumatic system is to channel high-pressure, high-temperature bleed air from the engines to power other subsystems. As demonstrated in Figure 69, the pneumatic system is comprised of two air conditioning units. Air will pass from the left and right engine through PRSOVs and into the respective left and right A/C units located at the bottom of the fuselage in between the wings. The PRSOV regulates the pressure of the bleed air entering the aircraft and provides for reverse air flow protection. It functions as the on/off control for the engine bleed system. The pneumatic system is used to start the engine. By utilizing hot bleed air from the APU, a pneumatic starter motor on the engine accessory gearbox is activated and is able to crank the engine to 20% of full speed. At this point ignition is achieved and the engine is started [56].

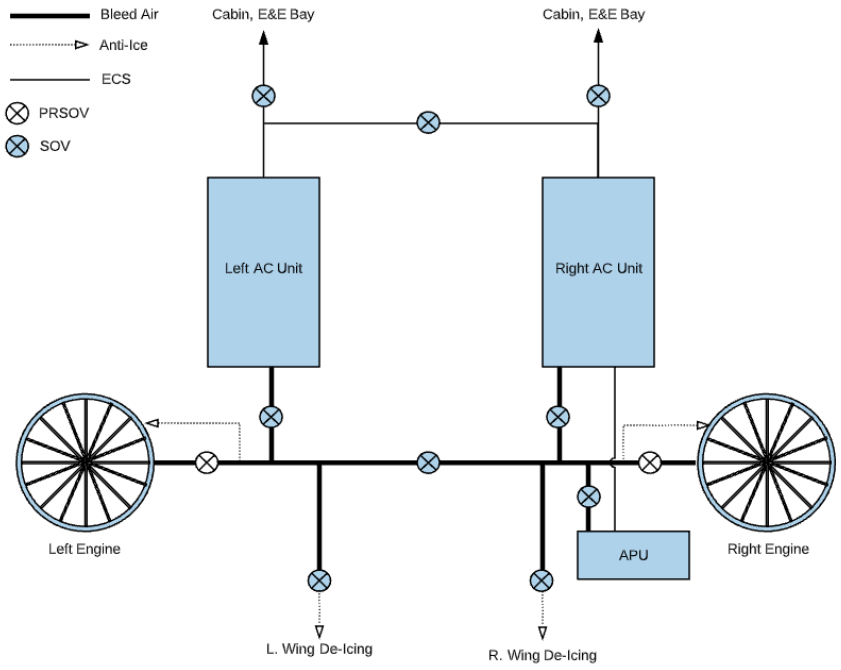

Figure 69 Pneumatic, Environmental Control, and De-Icing Systems Configuration

The available bleed air has a number of uses beyond engine starting. Hot bleed air is diverted from the engines and is used for thermal de-icing of the wing leading edges and engine cowlings. A wing anti-ice valve will enable hot air to flow to the outer wing leading edges through a leading edge heating duct. The engine is de-iced using an engine anti-ice valve and an engine cowling heating duct.

For the environmental control systems aboard the aircraft, bleed air from the engines and APU is passed into one of two air conditioning units, and is pressurized to 8,000 ft, as mandated by the RFP [1]. This pressurized, cooled air passes through a filter to remove any bacterial contaminants, and enters the cabin through a system of overhead ducts, as demonstrated by Figure 70. The air is then cycled out of the cabin at floor level. The air is circulated from top to

bottom as opposed to front to back in an effort to reduce cross-contamination between passengers to ensure their health and safety. The air filters on the *Argo* are high efficiency, and are similar to filters used in hospital operating rooms, making them effective in removing not only bacteria, but also viruses and any other particles that might contaminate the cabin [54]. Consumers have historically expressed concerns about possible health effects due to cabin air contamination, which is especially relevant in the COVID-19 era. Studies have shown, however, that people are no more likely to catch an infection on an aircraft than if they were travelling on other public transportation, attending a conference, or participating in any other similar activity that puts them in close contact with other individuals [57]. Further, evidence from these studies did not establish a link between cabin air contamination and ill passenger health [57].

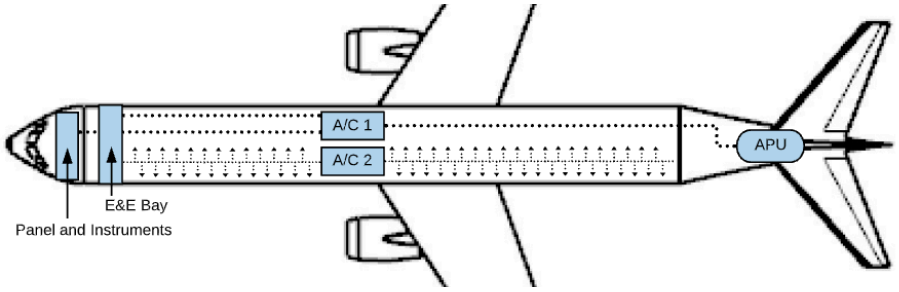

Figure 70 Environmental Control Systems Cabin Airflow Configuration

Further, the *Argo* also utilizes pneumatic bleed air to regulate the temperature of the E&E bay and APU. Many of the avionics components, as well as the APU, utilize electric components, which can only safely operate beneath 100° C [54]. As a result, it is necessary to keep the E&E bay and aft portion of tail where the APU is housed regulated between −20° C and 90° C to ensure the reliability of the electrical components. This cooling is done in a similar way to the cabin cooling system as shown in Figure 70.

F. Emergency System

The first component of the emergency system is the pilot warning system within the flight deck. First, system warnings are detected by sensors, which then send a signal to the flight deck panels. Emergency power is provided by the RAT. The RAT is an air-driven turbine that is stowed in the ventral section of the aircraft, and is automatically extended when an emergency begins. Once it is extended, it remains in that position for the duration of the flight, and must be restowed by a maintenance crew. It is an ideal component, as the RAT does not require any power source other than forward movement of the aircraft. The minimum aircraft speed required to power the RAT is 125 kt [54]. In the event of a cabin pressurization failure, the *Argo* has emergency oxygen masks stored in compartments above every passenger and crew seat. These face masks will drop automatically upon depressurization if the aircraft is above 14,000 ft. The emergency oxygen system consists of chemical oxygen generators above every seat block. By pulling down on a mask once it descends, the oxygen supply will be opened for every mask in the compartment, and will last for fifteen

minutes. This is sufficient time for the aircraft to descend to an altitude at which it is safe for passengers to breathe without the need for supplementary oxygen [58].

In the event that passenger evacuation is necessary, the aircraft has eight doors that can be used as emergency exits. All exits are fitted with illuminated signs to mark them as exits, and are equipped with emergency slides that are powered by the aircraft's batteries. The floor of the cabin is illuminated to direct passengers to the nearest exit. Life vests are stored beneath every passenger seat and crew seat, and life rafts are stored in overhead bins on each aircraft. One of the key emergency components is the flight recorder, which stores information about the aircraft's flight conditions and is a valuable tool in crash analyses.

G. Water and Waste System

Potable water systems in the *Argo* will be able to transport both warm and cold water. Warm water will be supplied by passing cold water through an electrical heat exchanger. Waste systems on the aircraft are self-contained, and there are 7 lavatories on board. There are waste tanks which mix waste with chemicals in the flushing liquid. The tanks will be emptied by means of a drain mast and panel. The lines that connect the potable water system and the waste system will be located far from any other access panel to avoid contamination and to limit interference with aircraft loading, unloading, and maintenance [45].

H. Avionics

In order to comply with the FAA, the avionics systems on the *Argo* meet all the requirements stated by CFR Part 14 [59]. After careful research, it was determined that an a la carte suite of avionics would not only be the most cost effective for the *Argo* in terms of component cost, but would result in lower maintenance costs as well. The a la carte suite allows components on the *Argo* to be replaced individually, as opposed to replacing the entire avionics system. Special attention has been given to ensure that avionics systems from different manufacturers are able to integrate seamlessly. In-house integration will drive up research and development cost slightly to ensure proper integration, but the difference in cost is mitigated by the weight, unit, and operating cost savings from the a la carte method.

By examining supplier data for the avionics equipment aboard similar aircraft and completing a trade study, a number of avionics components have been selected, as noted in Table 41. These products represent the most recent, most advanced, and lowest weight models for the given systems. The arrangement of many of these components can be seen in Figure 71. One unique feature of the *Argo* is the utilization of heads-up displays, which give pilots access to critical flight information while still allowing them to focus their attention outside the flight deck, ultimately leading to a safer flight.

Special attention has also been given to the selection of the autopilot. The RFP states that the onboard autopilot system must be capable of VFR and IFR flight. The Honeywell Primus 1000, noted in Table 41, is capable of meeting

Figure 71 Flight Deck Configuration

this requirement [1]. VFR regulations apply when weather conditions are clear enough to allow pilots to have an unobstructed view outside of the flight deck. 14 CFR §91.205 [59] mandates instruments and equipment which are required for VFR flight. These include, but are not limited to, an altimeter and fuel gauge for the engines, whose suppliers for the *Argo* are detailed in Table 41. When operation under VFR is deemed unsafe, usually due to adverse weather conditions, IFR flight must be used instead. Additional components necessary for IFR flight include navigation aids such as an ADIRS, an MMR, and distance measuring equipment in addition to two-way communication, which is satisfied by ADS-B [59]. Suppliers and models for all of these components are detailed in Table 41.

The ADIRS acts as a single source of navigational data by supplying air and inertial reference information to both the pilots and other systems, including the engines, autopilot, flight control system, and landing gear system. MMRs also aid in navigation, but are multi-function units that provide the aircraft's primary position, velocity, GPS, and time references. The MMRs enable instrument and GPS route and landing functions [60]. The ADS-B component serves as the automatic connector between the aircraft and ATC, which allows the *Argo* to be tracked in flight and have its satellite position periodically broadcast. This enables ATC and other aircraft to be aware of the *Argo's* position [61]

Because of the unique selection of avionics components and their in-house integration, the *Argo* will utilize a data concentration network (DCN) to more accurately monitor each system and its health and consolidate the data. By utilizing all onboard sensors, the DCN will be able to detect, predict, and isolate the majority of avionics issues on the aircraft, which will reduce overall avionics costs and operating cost in the long run.

All avionics components will be located in the main E&E bay, which is located at the bottom of the fuselage behind the flight deck. The weather radar will be located in the nose of the *Argo*. The forward and aft equipment centers will house and provide access to many of the sensors utilized across the systems.

Table 41 Selected Avionics Equipment

Category	System	Model
Communications	Intermediate Gain Antenna	CMC Electronics CMA-2200SB
Communications	Communications Mgmt Unit	Collins Aerospace ACARS
Communications	Omnidirectional Radio	Collins Aerospace VOR-900
Communications	ADS-B	ACSS NXT-800
Communications	High Gain Antenna	CMC Electronics CMA 2102SB SATCOM High Gain Antenna
Communications	VHF	Collins Aerospace VHF-2200
Communications	HF	Collins Aerospace HFS-900D
Communications	SATCOM	Collins Aerospace Iridium Certus SATCOM
Communications	Wireless Connectivity System	Gogo 2Ku Global Connectivity
Communications	Data Link	Collins Aerospace AOC-900
Communications	Mode S Transponder	Collins Aerospace Mode S Transponder
Indicating Systems	Angle of Attack Sensor	Collins Aerospace Angle of Attack Sensor
Indicating Systems	Pitot Probes	Collins Aerospace Pitot Probes
Indicating Systems	ETACS Ground System	Collins Aerospace ETACS Ground Maneuvering System
Indicating Systems	Radio Altimeters	Collins Aerospace Radio Altimeters
Indicating Systems	Weather Radar	Collins Aerospace WXR-2100
Indicating Systems	TCAS	Collins Aerospace TCAS
Indicating Systems	Fuel Quantity Indicator	Collins Aerospace Fuel Quantity Indicator
Navigation Aids	Omni-Range Receivers	Collins Aerospace DME-2100 VOR
Navigation Aids	ADIRS	Honeywell Aerospace ADIRS
Navigation Aids	MMR	Honeywell Aerospace IMMR
Navigation Aids	Distance Measuring Equipment	Collins Aerospace ADF-900
Navigation Aids	Heads-up Display	Collins Model 2200 HUD
Flight/Data Mgmt	flight deck Printers	Collins Aerospace FlightDeck Printer
Flight/Data Mgmt	Flight Control Electronics	BAE Systems Integrated Flight Controls
Flight/Data Mgmt	Flight Mgmt System	Honeywell Aerospace Pegasus
Flight/Data Mgmt	flight deck Voice Recorder	L3 Aviation flight deck Recorders
Flight/Data Mgmt	Flight Data Recorder	L3 Aviation AFIRS228S
Flight/Data Mgmt	AIMS	Collins Aerospace AIMS
Flight/Data Mgmt	Autopilot	Honeywell Aerospace Autopilot Primus 1000
Warning Systems	EGPWS	Honeywell Aerospace EGPWS

XII. Cost Analysis

A. Production Cost

The main method used to estimate the production cost for the *Argo* is the DAPCA IV cost model, developed by the RAND Corporation, which estimates cost on the basis of a five year production run [5]. The model outlines

production cost, including RTD&E costs, as well as the flyaway cost, which includes the labor and material costs to manufacture the aircraft. The DAPCA model takes inputs of aircraft empty weight, maximum velocity, production quantity, flight test aircraft, and avionics weight in order to determine production hours by the engineering, tooling, manufacturing, and quality control groups. By multiplying these production hour estimates by hourly wrap rates, outlined in Table 42 and price adjusted for inflation in 2029, a reasonable estimate for production cost can be determined. Based on historical data, which estimates that inflation over the past decade has risen 1.3% annually, prices for 2029 have been inflated by a conservative 2% annually, causing a cumulative price change of 18% over the next nine years.

Table 42 Wrap Rates Adjusted for Inflation

Labor Area	2012 Dollars per Hour [5]	2029 Dollars per Hour
Engineering	$115	$152
Tooling	$118	$156
Quality Control	$108	$143
Manufacturing	$98	$130

The *Argo's* production run will feature five test aircraft, which are factored into the cost estimate. These aircraft will be designated for max stress testing, max fatigue testing, interiors testing, and the remaining two aircraft will be designated as flight test aircraft. It is expected that three of these flight test aircraft will be sold to customers at a discounted price after testing is complete. The selected engine, the Rolls Royce Trent XWB-97, is listed at a purchase price of $35 million [62]. It is estimated that the customer will be able to purchase the engine at a lower unit price than listed. It is anticipated that a contract will be formed between the *Argo's* manufacturer and Rolls Royce. For the purposes of conservative cost estimation, the list price has been utilized. The avionics cost of the *Argo* is based upon the anticipated weight of the avionics components aboard the aircraft. The cost per pound of avionics components is estimated to be $4,500 per pound of avionics adjusted to 2029 inflation [5]. Taking these assumptions into consideration, estimates were made for 5-year production quantities of the *Argo* aircraft, as detailed in Table 43.

Table 43 DAPCA IV Estimates for Production Cost [in billions of dollars]

5-year AC Production Quantity	500 units	1000 units	2000 units
Engineering Cost	$8.565	$9.590	$10.737
Tooling Cost	$5.824	$6.988	$8.386
Manufacturing Cost	$28.120	$43.850	$68.380
Quality Control Cost	$4.121	$6.427	$10.022
RDT&E + Flyaway	$105.981	$180.016	$304.315
Unit Cost	$0.190	$0.162	$0.136
Unit Cost + 15% Profit	$0.219	$0.186	$0.157

On the lower end of the cost, a 5-year 2,000 unit production run of the *Argo* will cost an estimated $136 million per aircraft. At the high end, a 500 unit production run will cost $190 million per aircraft.

As a secondary method of cost estimation, a linear relationship between aircraft empty weight and average aircraft sales price has been calculated. This CER is a statistical cost estimating method, and has been shown to have an accurate, correlated relationship between empty weight and purchase price [5]. In order to compile the most accurate model possible, empty weight and purchase price data were collected for over 55 commercial aircraft currently in service. Because many of these models are derivatives of prior aircraft, two models were compiled: the first investigated the relationship between the empty weights of the 55 different aircraft and their purchase price, while Figure 72 focuses solely on the relationship between parent aircraft cost and empty weight.

The second model was selected to estimate the *Argo's* purchase price because it accounted for the higher development cost of parent aircraft. It also had a stronger correlation than the first model. Because the *Argo* is a clean-sheet aircraft and will serve as the parent aircraft for a series of aircraft, it will have the high research and development costs similar to existing parent aircraft.

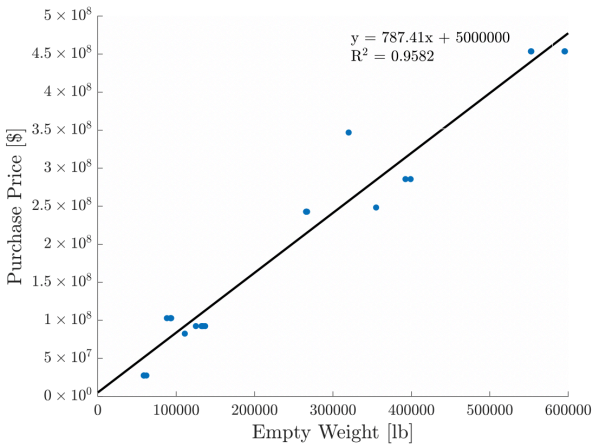

Figure 72 Linear Cost-to-Weight Model

By utilizing the linear equation from Figure 72, it can be estimated that the average sales price of the *Argo* will be $234 million. This estimate falls close to the upper range of the DAPCA IV cost estimation model. However, the linear model faces uncertainties as it relies on published sales prices which incorporate an unknown amount of manufacturer profit. Therefore, the DAPCA IV method is a higher fidelity cost model, and the team is confident that a production run of 1,000 units of the *Argo* will cost $186 million.

Figure 44 compares the *Argo* price to other similar aircraft published purchase prices, adjusted for 2029 inflation. When the DAPCA IV cost estimation values are adjusted for a 15% profit margin, as mandated by the RFP [1], and a commercial aircraft correction factor of 0.9 is applied, the *Argo* is cost competitive. The *Argo* is less expensive than other high-capacity (but longer range) aircraft like the Boeing 777-200ER or the Airbus A350-1000, and more

Table 44 Cost Similarity Analysis [63], [64]

Aircraft	Cost [millions of dollars]
Airbus A350-1000	$432.48
Boeing 777-200ER	$361.79
Boeing 787-8	$293.00
Airbus A330-200	$286.49
Argo (linear estimate)	$233.55
Argo (500 units)	$219.38
Argo (1000 units)	$186.32
Boeing 737 MAX 10	$159.19
Argo (2000 units)	$157.48
Airbus A321-200	$144.40
Boeing 757-300	$134.14

expensive than short-range (but lower capacity) aircraft like the Boeing 757-300 or the Airbus A321-200. Because the *Argo* lies in the middle of these two categories both in price and capability, it enables the *Argo* to be the first mover in a new market segment that caters to high-capacity, short-range transport aircraft.

B. Direct Operating Costs

Because aircraft more frequently fly their optimized mission than their maximum-range mission [5] and often land with substantial amounts of fuel remaining in the fuel tanks, the operating costs have been determined for the *Argo's* 700 nmi optimized mission. This mission is similar to a fight route between ORD and DFW, which is a 697 nmi distance.

1. Fuel and Oil Cost

The RFP mandates Jet-A fuel for the *Argo*. The cost of fuel per gallon is $3.00, and is also subject to a $3.00 per gallon carbon tax [1]. On a typical 700 nmi mission, which burns 8,635 gallons of fuel, the typical fuel burn per mission hour was calculated to be $24,454.

2. Crew Salaries

The cost of commercial aircraft crew is estimated by block hours as opposed to flight time hours. This accounts for fifteen minutes of ground maneuver time and six minutes of air maneuver time, as well as the adjusted mission distance as a result of federal airway routes, which are not straight-line distances from airport to airport. Taking these considerations into account, one flight hour equates to an hour and eleven minutes of block time. The aircraft requires a flight crew of 2 pilots and 8 flight attendants [1]. By drawing from average captain, first officer, and flight attendant salaries detailed by Roskam [65] in 1990 and adjusting for 2029 inflation, the following hourly rates detailed in Table 45

are calculated. Roskam values for flight crew salaries were used in lieu of current flight crew salary data, as current data takes a multitude of factors into account, including airline, years of experience, benefits, and fleet specialization, which are beyond the scope of preliminary design.

Table 45 Crew Salary [dollars per hour]

Captain	First Officer	Flight Attendant
$286	$145	$81

By multiplying these salary rates by the aforementioned block hour to flight hour relationship, crew salary cost per year is calculated and described in Table 46. It is important to note that this crew salary cost does not equate to an individual flight crew member's salary, but rather, equates to the cost of staffing the aircraft for every hour that it is in flight per year. An aircraft averages between 2,500 and 4,500 flight hours per year, while flight crew work an average of 800 flight hours per year [5].

3. Maintenance Expenses

Maintenance costs depend largely on how often the aircraft is serviced, and the cost required to fix faulty components. It is broken down into two parts: maintenance labor cost and material cost. The range of maintenance man hours needed per flight hour varies between 5 and 15 for the average civil transport vehicle according to flight hours. Maintenance man hours are the largest driver of maintenance cost and should be as low as possible [5]. Due to the ambiguity of the Raymer range for maintenance man hours, the average standard commercial aircraft maintenance scheduling method was considered. There are four types of maintenance checks that an aircraft goes through: A check, B check, C check, and D check. A checks are the most frequent, occurring every 500 flight hours, and since the *Argo* flies anywhere from 2,500 to 4,500 flight hours per year, the Argo will go through 5-9 A checks each year. A checks require 60 maintenance man hours each. The *Argo* will undergo 2 B checks per year, one C check every two years, and one D check once every six to ten years. By coupling these statistics with their required maintenance man hours, the average maintenance man hours per flight hour can be calculated to be 7.9, which is within the range offered by Raymer [5]. This accounts for an extra 30 minutes per flight hour, which is a conservative correction factor put in place to account for unscheduled maintenance. In the absence of any comparable data, the labor cost per hour estimate for maintenance workers can be assumed to be equal to the engineer wrap rate evaluated previously. The material cost for the components that need to be repaired, replaced, and scrapped are also factored in to the maintenance expenses.

4. Depreciation, Insurance, and Landing Cost

A key aspect of cost for commercial aircraft is depreciation, which can be estimated to follow a straight line depreciation trend. The method used to determine the rate of depreciation is the difference between the airframe cost and

the final resale value divided by the number of years used for depreciation prior to aircraft scrap or retirement. Because neither the *Argo's* lifespan nor the its final resale have been determined, the depreciation rate cannot be modeled with any certainty. There are, however, credible models that estimate that the depreciation accounts for 12% of the aircraft's operating costs [5]. This estimate was used to calculate depreciation expenses for the *Argo*. Similarly, insurance costs account for 1% of the total cost. Airport landing fees also add an additional 2% on top of the total cost.

5. Total Operating Cost

The total operating cost for flight hours ranging from 2,500 to 4,500 flight hours per year per aircraft is detailed in Table 46. Cost per flight hour remains constant regardless of the various operator flight hours per year. The cost per flight hour is detailed in Table 47.

Table 46 Maintenance and Operation Cost per year and per flight hour [in millions of dollars]

Cost per Year	2,500 FH/yr	3,000 FH/yr	3,500 FH/yr	4,000 FH/yr	4,500 FH/yr
Fuel	$61.135	$73.363	$85.590	$97.817	$110.044
Crew Salaries	$3.083	$3.699	$4.316	$4.933	$5.549
Maintenance	$18.941	$22.729	$26.518	$30.306	$34.095
Depreciation	$13.535	$16.242	$18.949	$21.656	$24.363
Insurance	$1.127	$1.353	$1.579	$1.804	$2.030
Landing Fees	$2.255	$2.707	$3.158	$3.609	$4.060
Total Cost	$97.498	$116.998	$136.498	$155.997	$175.497

Table 47 Cost per Flight Hour

Fuel	Crew Salaries	Maintenance	Depreciation	Insurance	Landing Fees	Total
$24,454	$1,233	$7,576	$5,414	$451	$902	$38,999

C. Cost Saving Options

The linear cost model as well as the DAPCA IV model are based heavily on aircraft empty weight, production quantity, and maximum velocity. Due to data unavailability, avionics cost is currently determined by avionics weight estimates multiplied by the anticipated cost per pound of the equipment. Therefore, the avionics cost could be reduced by choosing lighter components, thereby making a compromise between capability and cost. The engine cost also plays heavily into the aircraft's total cost. The given figure for engine cost is manufacturer list price per engine. Establishing a relationship between Rolls Royce, the engine supplier, and forming a contract to purchase the engines in bulk, and therefore at a discount, could also reduce the *Argo's* anticipated cost. Further, there is not a condition where the aircraft is utilizing the full capability of the engine, which makes the purchase of a de-rated engine possible. This would reduce the cost of the engine.

The design team has also already taken measures to reduce cost in terms of systems. First, the there will be no seatback monitors for IFE onboard the aircraft. This was discussed in Section XI.D. Team Dauntless is also able to immediately create a new extended range version of the *Argo* by incorporating an auxiliary fuel tank between the wings and keeping the rest of the design the same. This additional tank is marked with the dotted box region in Figure 66. This enables customers to make the decision to purchase the current range design, or an extended range design for an additional cost. Because the *Argo's* suggested retail price already lies so far below other high-capacity, long-range aircraft, a long-range version of the *Argo* would be cost competitive with existing aircraft in the same market segment.

Lastly, a trade study was conducted to compare materials for the wing structure. Both aluminum and graphite-epoxy composites were considered. In terms of weight savings, substituting a graphite-epoxy composite for aluminum yields 25% weight savings [5]. The *Argo* is primarily driven by weight saving characteristics, so the selection of a composite for the wings seemed like a natural choice. Composite materials also require less maintenance, meaning that in general, operating cost savings over an aircraft's lifespan often mitigate the up-front cost that is inherent to composites. The DAPCA cost model for the *Argo* was simulated taking the weight savings and cost correction factors into account. The DAPCA method estimates hours and costs based upon the design and fabrication of a purely aluminum aircraft. Therefore, a cost correction factor is necessary to account for not only the increased cost of material, but also for the increase in labor hours required for engineering, tooling, manufacturing, and quality control. The entire production cost of the aircraft is affected by the material substitution. Raymer presents a correction factor range from 1.1-1.8 for composite material substitution, so the team selected an intermediate correction factor of 1.5, as only the wings would be made of composites [5]. This correction factor resulted in an $81 million cost increase per aircraft for a 1,000 unit production run, and only $200 cost savings on an operating cost basis. Even if the *Argo* operated 4,500 flight hours per year, it would take upwards of 90 years to break even on the composite decision. Therefore, the team has decided to have an all aluminum aircraft.

D. Model Uncertainties and Inaccuracies

One cost uncertainty lies in the straight line estimation model. This model relies on cost data from OEMs such as Boeing and Airbus. These values factor in OEM profit, but it is difficult to determine what percentage of the list price is due to profit versus production.

Many of the aforementioned cost estimation models were created years ago, with cost data that is no longer relevant or timely. All of the figures for the *Argo's* cost models have been adjusted for general 2029 inflation. However, there are most likely different inflation rates for material parts, labor, or fuel, and other industries, which this cost model is unable to take into account.

Another uncertainty is in the direct operating cost breakdown. Roughly 63% of the operating cost is due to fuel costs, which is a highly conservative figure. For the 700 nmi optimized mission, a time step integration shows that

58,200 lb of fuel are required to complete the mission, which correlates to 8,635 gallons of fuel. The RFP mandates that fuel costs $3 per gallon with an additional $3 per gallon carbon tax, which makes the overall fuel cost $6 per gallon [1]. Average fuel costs for Jet-A over the past year are reported as $1.12, however, this is also a low estimate as it is impacted by uncharacteristically inexpensive jet fuel prices as a result of the COVID-19 pandemic [66]. To adjust for inflation and to mitigate the effects of the pandemic on fuel prices, a more accurate estimate for fuel cost in 2029 would be $2 per gallon. This would reduce fuel costs by two-thirds and result in operating costs of $16,000 per flight hour. This is a much more realistic estimate.

XIII. Acoustics

A. Acoustic Requirements

Acoustic requirements for the *Argo* were set in accordance with CFR Part 36 [67] and the Stage 5 Noise Standards [68] established by the FAA. For an aircraft to successfully meet these standards, the noise level at three different stages- lateral, flyover, and approach- must fall below these limits [69]. Methodologies for determining limits for each of these three stages are discussed below. For each of the stages, the limit was set by interpolating from the plot of MTOW against the Effective Perceived Noise Level (EPNL) found in Stage 5 [68].

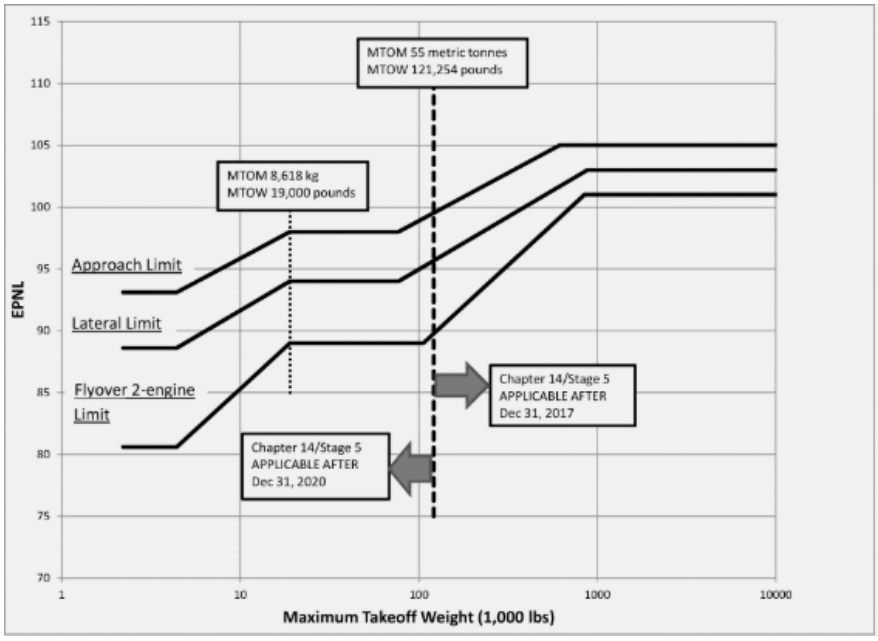

Figure 73 MTOW [lb] Plotted Against EPNL [dB] [68]

1. Lateral

The lateral noise level refers to the acoustic profile of an aircraft at full power after takeoff. This profile was constructed by measuring noise along a line parallel to and 450 m from the runway center line[69]. A time-step

integration was carried out from k_F to k_L, where k_F is defined as the first time instance of the 10 dB-down measurement from the peak noise, and k_L is defined as the last time instance of the 10 dB-down measurement from the peak noise shown in Figure 74. The lateral limit set for the Argo was 100.5 dB based on Figure 73.

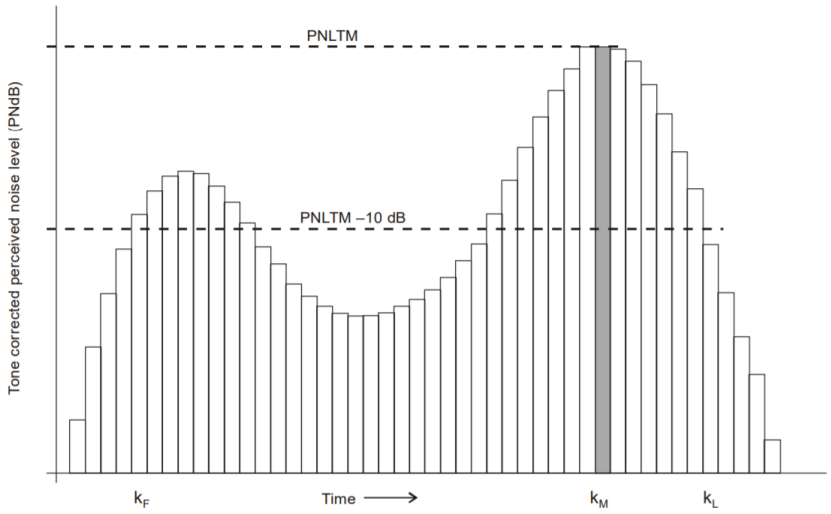

Figure 74 Time Step Integration Points for Acoustic Measurements, k_F and k_L [68]

2. Flyover

The flyover noise level was calculated by taking a time-step integration using measurements at the point on the extended centre line of the runway and at a distance of 6,500 meters from the start of roll [69]. Similar to the measuring technique for lateral noise, the time-step integration is carried out from k_F to k_L. The flyover limit set for the *Argo* was 98.8 dB based on Figure 73.

3. Approach

The approach noise measurement location is the point on the extended centre line of the runway 2,000 meters from the threshold. On level ground, it can be defined as the position 120 meters vertically below the 3° descent path. The descent path originates at a point 300 meters beyond the runway threshold [58]. Similar to the measuring technique for lateral noise, the time step integration is carried out from k_F to k_L. The limit set for the *Argo* was 104.4 dB based on Figure 73.

B. Acoustic Model

Acoustic levels were plotted using information provided by the ICAO Aircraft Engine Emissions Databank [70]. Engines with thrust levels ranging from 72,066 - 115,000 lb were selected for this analysis. Acoustic trend lines were used to make a reasonable estimation for the noise levels generated by the *Argo* based on the takeoff thrust of 97,000 lb provided by the Trent XWB-97.

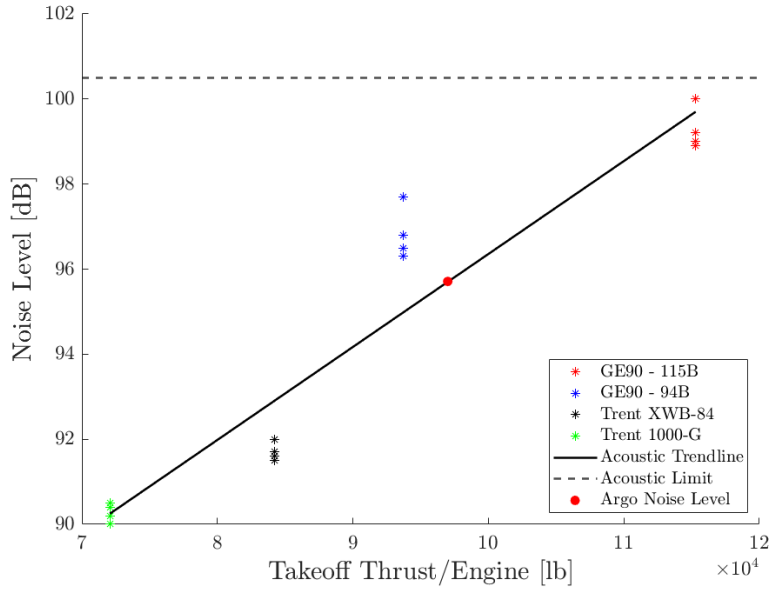

Figure 75 Thrust per Engine Plotted Against Noise Level (Lateral)

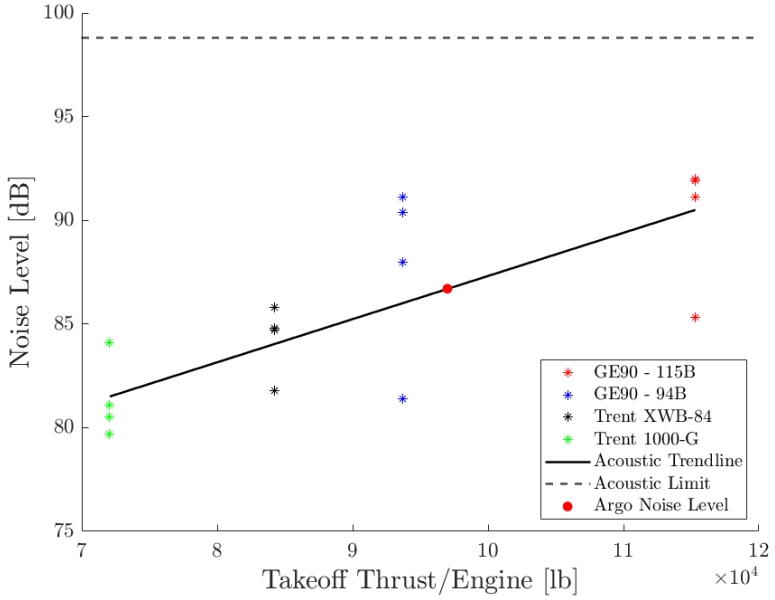

Figure 76 Thrust per Engine Plotted Against Noise Level (Flyover)

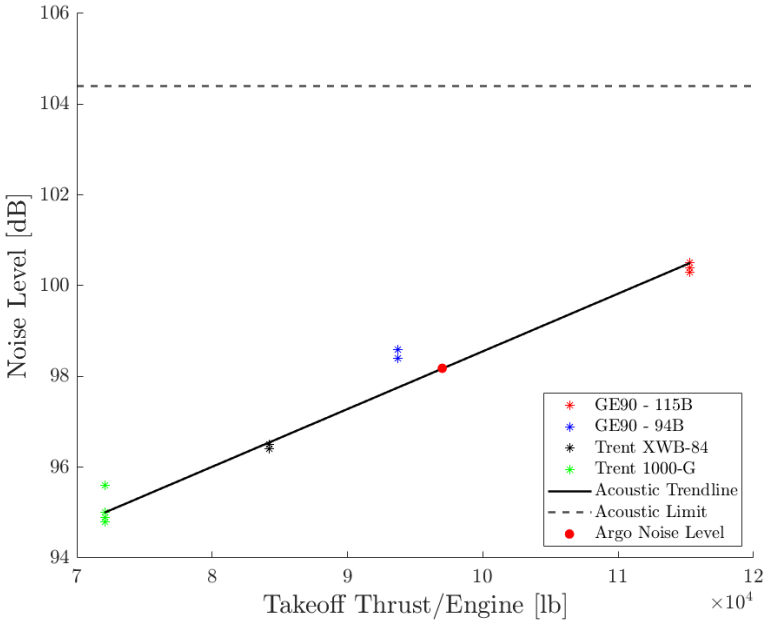

Figure 77 Thrust per Engine Plotted Against Noise Level (Approach)

Figures 75, 76 and 77 show that the maximum noise levels predicted by the model are well below the limits discussed earlier. Based on the thrust level of 97,000 lb, the lateral noise level for the *Argo* is 99.5 dB, the flyover noise level is 90 dB and the approach noise level is 100.5 dB. Table 48 compares the acoustic limits and predictions for the *Argo*.

Table 48 Acoustic Limits and Predictions for *Argo*

	Lateral [dB]	**Flyover [dB]**	**Approach [dB]**
Acoustic Limit	100.5	98.8	104.4
Acoustic Prediction	95.7	86.7	98.2

C. Model Uncertainties and Inaccuracies

While the model shows a positive correlation between thrust and noise level, there are some uncertainties. Figures 75, 76, and 77 show that engines with the same thrust ratings may have varying accompanying noise levels. This adds a level of uncertainty to the model. Furthermore, exact information on the thrust levels and de-rating of engines is not available in the ICAO Aircraft Engine Emissions Databank [70]. A reasonable estimation of engine thrust was made based on the engine model selected. Finally, CFR Part 36 mandates that acoustic testing can only be carried if a certain set of environmental conditions are met [71]. These criteria include availability of level ground, relatively low air traffic, and favorable environmental conditions. However, ambient noise will always be present regardless of the environment, which adds another degree of uncertainty.

D. Emissions

The airline industry in the United States today is responsible for approximately 12% of transport emissions and 3% of the country's greenhouse gas production, so it is important to estimate the environmental impact of the *Argo's* operations [72]. The ICAO Carbon Emissions Calculator [73] was used to estimate the CO_2 emissions for a range of hypothetical routes, as seen in Table 49. The *Argo* is designed to operate between 2,500 and 4,500 flight hours per year. For the purpose of CO_2 estimation, an intermediate case of 3,500 flight hours per year was utilized to calculate the number of flight cycles per year, which is used to determine the carbon emissions per passenger per year.

The different routes were analyzed with mission ranges between 500 nmi and 3,500 nmi, and the resulting CO_2 emissions ranged from 267,000 lb to 443,000 lb depending on the mission. If the *Argo* flies only the optimized 700 nmi range, CO_2 emissions per passenger per year are 396,000 lb. The RFP notes a mission profile from JFK to LHR [1]. This route results in 345,000 lb of emissions per passenger. It is interesting to note that there is little to no linear correlation between mission range and CO_2 emissions per passenger, as seen in Figure 78. This is because the ICAO Emissions Calculator only considers aircraft that are currently in service. Routes between 500 nmi and 2,000 nmi are normally serviced by low capacity, short range aircraft. Longer mission ranges are serviced by high-capacity, long-range aircraft. No aircraft are currently on the market that cater to short-range high-capacity routes like the *Argo*. Because the *Argo* is flying short-range missions, it will have a low emission output per cycle. This already low figure will be divided among 400 people meaning that the per-passenger emissions are quite low.

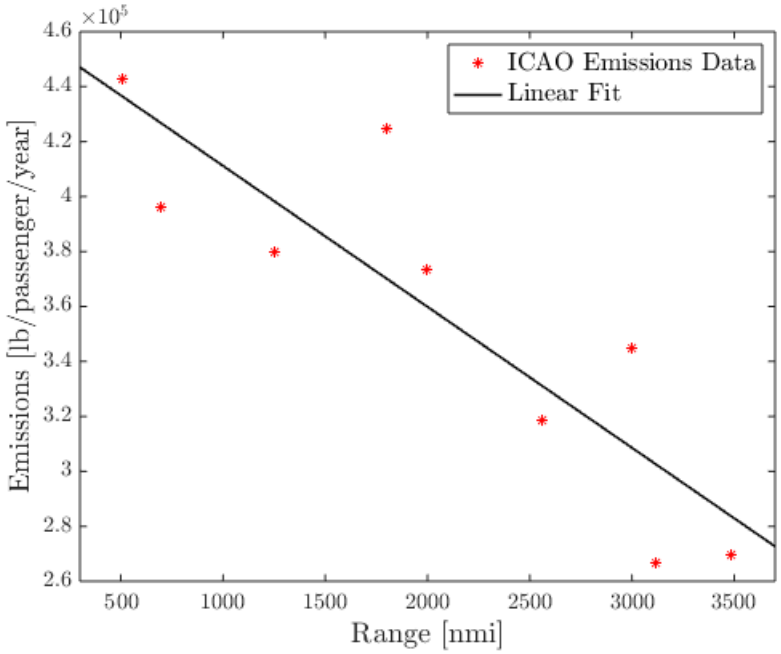

Figure 78 Emissions Data

Table 49 Estimate of CO_2 Emissions for Different Routes

Mission Range [nmi]	Origin	Destination	Flight Hours	Flights/year	CO_2 Emissions/pax/year [lb]
511	ORD	IAD	1.8	1900	443,000
696	ORD	DFW	2.5	1400	396,000
1,255	ORD	CUN	3.8	910	380,000
1,800	ORD	SJU	4.5	770	425,000
1,998	ORD	AUA	5.8	610	374,000
2,558	ORD	KEF	6.8	520	319,000
2,999	JFK	LHR	7.5	470	345,000
3,120	ORD	SNN	9.2	380	267,000
3,484	ORD	LIS	10.2	340	270,000

XIV. Conclusion

Airlines have begun to look for aircraft which can efficiently carry large numbers of passengers on short-range flights to relieve congestion at busy airports. The *Argo* is a high-capacity airliner which has been optimized for short-range flights. With a maximum range of 3,500 nmi and a capacity of 400 passengers, the *Argo* will be the first aircraft in a new market segment. At a unit cost of $186 million, the *Argo* will have a competitive pricing advantage over existing high-capacity airliners. With its high seating capacity, it will help relieve congestion at airports such as JFK or London Heathrow.

The *Argo* will have a traditional wing and empennage configuration. It utilizes an aspect ratio of 7.3 and a wing area of 4,000 ft^2 to reduce MTOW and fuel weight. Based on current estimates, the MTOW will be 500,000 lb. The design of the high-lift system and chosen engine technology enables a BFL of 9,000 ft. The unique a la carte avionics system enables VFR and IFR operations. All mandatory and tradable requirements have been satisfied by the design [1]. Additionally, variants of the *Argo* have been considered, which would reduce development costs and increase revenue. The *Argo* is well suited to the task of high-capacity, short-range operations, and the team is confident it will serve as a competitive option in an increasingly congested sky.

References

[1] AIAA, "AIAA 2020 Undergraduate Design Competition RFP," *American Institute of Aeronautics and Astronautics*, 2020. https://www.aiaa.org/docs/default-source/uploadedfiles/education-and-careers/university-students/design-competitions/undergraduate-team-aircraft-design-competition/undergraduate-aircraft-high-capacity-short-range-transport-aircraft.pdf?sfvrsn=b6081273_0.

[2] International Civil Aviation Organization, "ICAO Aerodrome Reference Code," 2017. https://www.skybrary.aero/index.php/ICAO_Aerodrome_Reference_Code, accessed on 4-29-2020.

[3] Jackson, P., *Jane's All the World's Aircraft*, 102nd ed., Sampson Low, Marson & Co., London, 2012.

[4] Cornell, "14 CFR § 25.303 - Factor of safety." 2018. https://www.law.cornell.edu/cfr/text/14/25.303, accessed on 2-12-2020.

[5] Raymer, D., *Aircraft Design: A Conceptual Approach*, 6th ed., American Institute of Aeronautics and Astronautics, Reston, VA, 2018.

[6] Roskam, J., *Airplane Design : Part V : Component Weight Estimation*, 1st ed., Roskam Aviation and Engineering Corporation, Reston, KS, 1985.

[7] Merret, J., "AE 443 Aerospace Senior Design at University of Illinois," 2020.

[8] AviationDB, "Aviation Database," 2019. http://www.aviationdb.com/Aviation/F4SDetailQuery.shtm#SUBMIT, accessed on 2-5-2020.

[9] GlobalAir, "Gulfstream G-650 Technical Specifications," 2019. https://www.globalair.com/aircraft-for-sale/Specifications?specid=1250, accessed on 2-11-2020.

[10] Alitalia, "Alitalia Cargo Standard Container Sizes," 2019. http://www.alitaliacargo.com/en/about-us/uld-standardcontainer-ake.html, accessed on 3-5-2020.

[11] Federal Aviation Administration, "FAA 14 CFR § 25.807," 2020. https://www.law.cornell.edu/cfr/text/14/25.807, accessed on 2-14-2020.

[12] ModernAirliners, "Boeing 787 Dreamliner Interior," 2019. http://www.modernairliners.com/boeing-787-dreamliner/boeing-787-dreamliner-interior/, accessed on 3-4-2020.

[13] SeatGuru, "SeatGuru Seat Map Lufthansa A340-600," 2019. https://www.seatguru.com/airlines/Lufthansa/Lufthansa_Airbus_A340-600_D.php, accessed on 2-10-2020.

[14] Rolls-Royce, "Rolls-Royce Trent XWB," 2020. https://www.rolls-royce.com/products-and-services/civil-aerospace/airlines/trent-xwb.aspx#/, accessed on 4-30-2020.

[15] European Union Aviation Safety Agency, "Type-Certificate Data Sheet for Trent XWB Series Engines," Tech. rep., EASA, 2019.

[16] Daidzic, N. E., "Estimation of Performance Airspeeds for High-Bypass Turbofans Equipped Transport-Category Airplanes," *Journal of Aviation Technology and Engineering*, 2016.

[17] Feagin, R. C., "Delta Method, An Empirical Drag Buildup Technique," 1978.

[18] Mason, W., "Transonic Aerodynamics of Airfoils and Wings," *Virginia Institute of Technology*, 2006.

[19] Selig, M., "UIUC Airfoil Coordinates Database," ???? https://m-selig.ae.illinois.edu/ads/coord_database.html, accessed on 4-21-2020.

[20] L. Jenkinson, D., P. Simpkin, "Butterworth-Heinemann - Civil Jet Aircraft Design," 2019. https://booksite.elsevier.com/9780340741528/appendices/data-a/table-4/table.html, accessed on 3-9-2020.

[21] Scholz, D., "Aircraft Design," 2015. https://www.fzt.haw-hamburg.de/pers/Scholz/HOOU/ , accessed on 3-9-2020.

[22] Sadraey, M. H., *Aircraft Design: A Systems Engineering Approach*, Wiley, 2013.

[23] McCormick, B. W., *Aerodynamics, Aeronautics, and Flight Mechanics*, John Wiley & Sons, Inc., 1979.

[24] Boeing Commercial Airplanes, "FAA Reference Code and Approach Speeds for Boeing Aircraft," Tech. rep., Boeing, 2016.

[25] Roberson, W., and Johns, J. A., "Fuel Conservation Strategies: Takeoff and Climb," 2008. https://www.boeing.com/commercial/aeromagazine/articles/qtr_4_08/pdfs/AERO_Q408.pdf, accessed on 3-13-2020.

[26] Torenbeek, E., *Synthesis of Subsonic Airplane Design*, Delft University Press, 1982.

[27] Tulapurkara, E., "Airplane Design," 2013. https://nptel.ac.in/courses/101/106/101106035/, accessed on 4-20-2020.

[28] "Electronic Code of Federal Regulations Part 25," 2020. https://www.ecfr.gov/cgi-bin/retrieveECFR?gp=&SID=b37456081ab32881662b60d7d60c2614&mc=true&n=pt14.1.25&r=PART&ty=HTML, accessed on 4-20-2020.

[29] Ulrich Glitsch, R. E. K. S., Hans Jürgen Ottersbach, "Physical workload of flight attedants when pushing and pulling trolleys aboard aircraft," *International Journal of Industrial Ergonomics*, November 2007.

[30] Nelson, R. C., *Flight Stability and Automatic Control*, McGraw-Hill Education, 1989.

[31] Leland Nicolai, G., *Fundamentals of Aircraft and Airship Design*, American Institute of Aeronautics and Astronautics, 1975.

[32] Roskam, J., *Methods for Estimating Stability and Control Derivatives of Conventional Subsonic Airplanes*, Roskam Aviation and Engineering Corporation, 1971.

[33] "Flight Test Guide for Certification of Transport Category Airplanes," 2018. https://www.faa.gov/documentLibrary/media/Advisory_Circular/25-7D.pdf, accessed on 3-6-2020.

[34] Ross, J. L., "MIL-F-8785B (ASG), Military Specification Flying Qualities of Piloted Airplanes, MSA 283, Series 3, Sub-Series 1, Sub-Group 3, File 24, Item 3." 1969. https://archives.lib.purdue.edu/repositories/2/archival_objects/19000, accessed on 4-29-2020.

[35] Cornell, "14 CFR § 25.337 - Limit maneuvering load factors." 2018. https://www.law.cornell.edu/cfr/text/14/25.337, accessed on 2-12-2020.

[36] Hale, J., "Boeing 787 from the Ground Up," *Aero*, 2006. https://www.boeing.com/commercial/aeromagazine/articles/qtr_4_06/article_04_1.html, accessed on 4-20-2020.

[37] Canaday, H., "COMPOSITES VS. METALS," *Aerospace America*, May 2015. http://www.omagdigital.com/article/COMPOSITES+VS.+METALS/1986792/254792/article.html, accessed on 2-21-2020 .

[38] MatWeb, 2019. http://www.matweb.com/index.aspx, accessed on 2-1-2020.

[39] Niu, M. C., *Airframe Stress Analysis and Sizing*, 2nd ed., Adaso/Adastra Engineering Center, 2001.

[40] Jun Liu, X. Y., Yulong Li, "Design of aircraft structures against threat of bird strikes," *Chinese Journal of Aeronautics*, July 2018.

[41] Mouritz, A., *Introduction to Aerospace Materials*, Woodhead Publishing Limited, 2012.

[42] Roskam, J., *Airplane Design Part III: Layout Design of Cockpit, Fuselage, Wing and Empennage: Cutaways and Inboard Profiles*, 3rd ed., DARcorporation, 1985.

[43] Megson, T. H. G., *Aircraft Structures for Engineering Students*, 6th ed., Butterworth-Heinemann, 2017.

[44] Gates, D., "Boeing Revs Up Robots for 777X in Everett Factory, Signals That a 797 Awaits," 2017. https://www.seattletimes.com/business/boeing-aerospace/boeing-revs-up-robots-for-777x-in-everett-factory-signals-that-a-797-awaits, accessed on 4-20-2020.

[45] Roskam, J., *Airplane Design Part IV: Layout Design of Landing Gear and Systems*, Roskam aviation and engineering Corporation, 1989.

[46] *777-9 Airplane Characteristics for Airport Planning*, Boeing, March 2018. Rev A.

[47] *787 Airplane Characteristics for Airport Planning*, Boeing, March 2018. Rev M.

[48] *777-200LR / -300ER / -Freighter Airplane Characteristics for Airport Planning*, Boeing, May 2015. Rev E.

[49] *A340-500/-600 AIRCRAFT CHARACTERISTICS AIRPORT AND MAINTENANCE PLANNING*, Airbus, Aug 2019.

[50] *A330 AIRCRAFT CHARACTERISTICS AIRPORT AND MAINTENANCE PLANNING*, Airbus, Aug 2019.

[51] *A350 AIRCRAFT CHARACTERISTICS AIRPORT AND MAINTENANCE PLANNING*, Airbus, Oct 2019.

[52] Cornell, "114 CFR § 25.733 - Tires." 2018. https://www.law.cornell.edu/cfr/text/14/25.733, accessed on 4-21-2020.

[53] "Aircraft Tire Data Book," *EASA*, 2002. https://www.aps-aviation.com/wp-content/uploads/goodyear-aircarft-tire-data.pdf, accessed on 3-22-2020.

[54] Moir, I., and Seabridge, A., *Aircraft Systems mechanical, electrical, and avionics subsystems integration*, Wiley, 2010.

[55] "Sidestick Vs Control Yoke?" ????. https://www.airliners.net/forum/viewtopic.php?t=760949, accessed on 4-9-2020.

[56] *Pilot's Handbook of Aeronautical Knowledge: FAA-H-8083-25B*, Aviation Supplies & Academics, 2016.

[57] "Passenger health FAQs: The aircraft cabin - your health and comfort," *UK Civil Aviation Authority*, ???? https://www.caa.co.uk/Passengers/Before-you-fly/Am-I-fit-to-fly/Health-information-for-passengers/Passenger-health-FAQs--The-aircraft-cabin---your-health-and-comfort/, accessed 5-13-2020.

[58] Smith, O., "The truth about oxygen masks on planes – what can the Southwest incident teach us?" *The Telegraph*, 2017. https://www.telegraph.co.uk/travel/travel-truths/truth-about-oxygen-masks-on-planes/.

[59] Cornell, "14 CFR § 91.205 - FPowered civil aircraft with standard category U.S. airworthiness certificates: Instrument and equipment requirements." 2018. https://www.law.cornell.edu/cfr/text/14/91.205, accessed on 2-12-2020.

[60] Adams, C., "Multimode Receivers: More Demand, More Capability," *Avionics Internation*, 2002. https://www.aviationtoday.com/2002/04/01/multimode-receivers-more-demand-more-capability/, accessed on 3-22-2020.

[61] "How ADS-B works," *Airservices RSS*, ????. http://www.airservicesaustralia.com/projects/ads-b/how-ads-b-works/, accessed on 2-9-2020.

[62] Norris, G., "GE90 secures exclusive position on 777X," *Flight Global*, 1999. https://www.flightglobal.com/ge90-secures-exclusive-position-on-777x/27600.article.

[63] Boeing, "Boeing Current Price," 2019. http://www.boeing.com/company/about-bca/#/prices.

[64] Airbus, "Airbus 2018 Price List Press Release," *Airbus*, 2018. https://www.airbus.com/newsroom/press-releases/en/2018/01/airbus-2018-price-list-press-release.html, accessed on 4-9-2020.

[65] Roskam, J., *Airplane Design: Part VIII Airplane Cost Estimation: Design, Development, Manufacturing, and Operating*, Roskam Aviation and Engineering Corporation, 1990.

[66] "Jet Price Fuel Monitor," 2020.

[67] Cornell, "CFR Part 36," *LII*, 1969. https://www.law.cornell.edu/cfr/text/14/part-36, accessed on 3-2-2020.

[68] FAA, "Stage 5 Airplane Noise Standards," *National Archives*, 2019. https://www.federalregister.gov/documents/2017/10/04/2017-21092/stage-5-airplane-noise-standards, accessed on 4-9-2020.

[69] EASA, "Noise Certification Workshop," *EASA*, 2006. https://www.icao.int/Meetings/EnvironmentalWorkshops/Documents/Noise-Certification-Workshop-2006/Boettcher_3.pdf, accessed on 4-9-2020.

[70] EASA, "ICAO Aircraft Engine Emissions Databank," *EASA*, 2019. https://www.easa.europa.eu/easa-and-you/environment/icao-aircraft-engine-emissions-databank, accessed on 3-10-2020.

[71] "Noise Standards: Aircraft Type and Airworthiness Certification," 2017. https://www.faa.gov/documentlibrary/media/advisory_circular/ac_36-4d.pdf.

[72] Overton, J., "The Growth in Greenhouse Gas Emissions from Commercial Aviation," 2019. https://www.eesi.org/papers/view/fact-sheet-the-growth-in-greenhouse-gas-emissions-from-commercial-aviation,, accessed on 4-30-2020.

[73] "Carbon Emissions Calculator," *ICAO Carbon Emissions Calculator*, 2016. https://www.icao.int/environmental-protection/Carbonoffset/Pages/default.aspx, accessed on 3-9-2020.